Pressure gradients in molecular dynamics simulations of nano-confined fluid flow

Zur Erlangung des akademischen Grades eines

Doktors der Ingenieurwissenschaften (Dr.-Ing.)

von der KIT-Fakultät für Maschinenbau des
Karlsruher Instituts für Technologie (KIT)

angenommene
Dissertation

von

M.Sc. Mohamed Tarek Elewa Hassan

Tag der mündlichen Prüfung: 19 Juli 2023
Erster Gutachter: Prof. Dr. Peter Gumbsch
Zweiter Gutachter: Prof. Dr. Lars Pastewka
Bearbeitungszeit: Juli 2019 bis Mai 2023

Acknowledgement

I would like to express my heartfelt gratitude and appreciation to all those who have contributed to the successful completion of this dissertation. Without their support, encouragement, and assistance, this work would not have been possible.

First and foremost, I would like to show my appreciation to my scientific advisors Prof. Dr. Peter Gumbsch and Prof. Dr. Lars Pastewka for their guidance and support during the time of my PhD. Their insightful feedback and constructive criticism have significantly shaped and improved the quality of this work.

The project was conducted at the Institute of Applied Materials at the Karlsruhe Institute of Technology in collaboration with the Department of Microsystems Engineering at the University of Freiburg. The project was part of the graduate school GRK-2450, funded by the Deutsche Forschungsgemeinschaft. I appreciate all the efforts done by Prof. Dr. Marcus Elstner to initiate the collaborations between the projects and continously develop the graduate school structure.

On the technical side, I acknowledge the support by the state of Baden-Württemberg through bwHPC (bwUniCluster 2.0 and bwForCluster NEMO) for the computing time as well as the storage facility LSDF at Karlsruhe Institute of Technology. The initialization of the nanofluidic systems in this thesis was accomplished with *Moltemplate* code [1]. The molecular simulations were performed with the MD package *LAMMPS* [2] and for visualization of the atomic trajectories, the *OVITO* package [3] was used. The research data management tool *dtool* [4] was helpful in managing and processing the scientific data.

I am deeply indebted to my colleagues at Karlsruhe and Freiburg for the fruitful and stimulating discussions. I would like to especially thank my project partner Dr. Hannes Holey and the simulations group at Karlsruhe

including Dr. Patrick Ziemke, Dr. Taymour El Achkar, Dominik Horny, Daren Liu and Balduin Katzer. From the collaborations within the GRK, I am grateful for the opportunity to work on supplementary projects with Tobias Kliesch and Dr. Ivan Kondov. Furthermore, I would like to thank Johannes Hörmann and Dr. Jan Mees for helping me with molecular dynamics simulations technicalities. The meetings with Saber Boushehri, Dr. Camilo Aponte-Santamaría and Prof. Dr. Frauke Gräter offered stimulating discussions on applying the methods in the thesis in the context of synovial joints.

I would like also to extend my appreciation to Dr. Daniel Weygand, Dr. Johannes Schneider and Dr. Andreas Greiner for their suggestions and advise on my project. Special thanks to Dr. Tarek Hatem who was continously supportive during my academic journey. For the adminstrative support, I am indebted to Ms. Andrea Doer, Ms. Sabine Holthoff, Ms. Stefanie Beysel and Ms. Anna Liolios-Zimmermann. For the IT support, I am thankful to Ms. Yiyue Li and Mr. Sascha Frank for being always reachable and helpful.

This work would not have been possible without the unwavering support and encouragement of my wife Funda, my mother Amel Saad, my father Tarek Elewa, my sister Passant Tarek and my grandparents Fatma Abdelkader and Ibrahim Saad. Last but not least, my gratitude extends to my friends.

Sincerely,
Mohamed Tarek Elewa Hassan
July 2023

Abstract

A detailed understanding of the behaviour of lubricants under high confinement is crucial for a range of medical and industrial applications. The hydrodynamic framework provides accurate solutions when the contacting bodies are sufficiently separated, however, at extreme operating conditions, the departure from the Navier-Stokes-Fourier equations is eminent. Atomistic effects can no longer be homogenized and the fluid can not be treated as a continuum-fluid decoupled from the behaviour of its discrete particles. A multiscale treatment of the problem becomes crucial as the fluid operates in the boundary lubrication regime. In this regime, the lubricant is driven by pressure gradients resulting from the gap height variation between the contacts. Atomistic models usually rely on non-equilibrium molecular dynamics (NEMD) simulations of periodic molecular representative volume elements (RVE), where the lubricant fluid is confined between slab walls. Due to periodicity, introducing pressure gradients in such models presents a hurdle. In this thesis, the "pump" method was developed to introduce pressure gradients in perodic RVEs by applying a local perturbation, based on linear momentum conservation, that induces pressure-driven flow of the lubricant. The independent variable can be the pressure gradient, by fixing the force, or the mass flux, by fixing the current. The two variants are equivalent. The method was tested on compressible and wetting fluids, and applied in conjunction with different thermostating strategies. Thermodynamic field variables of the fluid lubricant including velocity, pressure, flux, and temperature were measured and reported down to confinements of 3 molecular diameters. The pump method can be applied to a channel of arbitrary geometry. This permits the investigation of hydrodynamic cavitation, a phenomenon that is ubiquitous in nature yet not widely investigated on the molecular scale. A sensitivity analysis was conducted to optimize the channel geometry that promotes cavitation. Subsequently, the cavitation lifetime, growth and collapse were compared to the hydrodynamic theoretical predictions. Within a multiscale framework, the pump method can act as the constraint on the molecular system from the larger continuum scale.

Kurzfassung

Ein detailliertes Verständnis des Verhaltens von Schmierstoffen in engen Spalten ist für eine Reihe von medizinischen und industriellen Anwendungen entscheidend. Die hydrodynamischen Grundgleichungen bieten genaue Lösungen, sofern die kontaktierenden Körper ausreichend weit voneinander entfernt sind. Unter extremen Belastungsbedingungen werden jedoch Abweichungen von den Navier-Stokes-Fourier-Gleichungen beobachtet. Dies liegt hauptsächlich an der Bedeutung atomare Effekte, die eine homogenisierte Betrachtung im Rahmen von Kontinuumstheorien nicht mehr erlauben, sodass die Flüssigkeit als Ansammlung diskreter Partikel behandelt werden muss. Der multiskalige Charakter des Problems wird im Bereich der Grenzreibung umso deutlicher. In diesem Regime wird das Schmiermittel durch Druckgradienten angetrieben, die sich aus der Variation der Spalthöhe zwischen den kontaktierenden Körpern ergeben. In der atomistischen Modellierung werden üblicherweise Nichtgleichgewichts-Molekulardynamik (NEMD) Simulationen periodischer, repräsentativer Volumenelemente (RVE) verwendet, bei denen der Schmierfilm von flachen Wänden eingeschlossen wird. Aufgrund der Periodizität stellt das Einstellen von Druckgradienten in solchen Modellen eine Hürde dar. In dieser Arbeit wurde die "Pump"-Methode entwickelt, um Druckgradienten in periodischen Systemen einzuführen, indem eine lokale Störung aufgebracht wird, die unter Einhaltung der Impulserhaltung einen druckgetriebenen Fluss des Schmiermittels induziert. Dabei kann sowohl der Massenfluss als auch der Druckgradient, durch Festlegen atomarer Kräfte, als unabhängige Variable gewählt werden. Die Methode wurde für kompressible Fluide mit unterschiedlichen Benetzungseigenschaften und in Verbindung mit verschiedenen Thermostat-Strategien getestet. Dabei werden die thermodynamischen Feldgrößen Druck, Temperatur und Geschwindigkeit des Schmierstoffs in Spalthöhen bis zu drei Moleküldurchmessern gemessen. Die Pump-Methode kann auf Kanäle beliebiger Geometrie angewendet werden, was die Anwendung zur Untersuchung hydrodynamischer Kavitation ermöglicht – ein Phänomen, welches in der Natur allgegenwärtig ist, jedoch auf molekularer Ebene bisher kaum untersucht wurde. Dazu wurde die Kanalgeometrie anhand einer Sensitivitätsanalyse optimiert. Anschließend wurde die Lebensdauer der Kavitationsblasen, sowie deren Wachstum und Zusammenbruch mit den theoretischen, hydrodynamischen Vorhersagen verglichen. Im Rahmen eines Multiskalenansatzes für Schmierungsprobleme kann die Pump-Methode zur Einstellung der Randbedingungen eines molekularen Systems im Einklang mit Kontinuumssimulationen verwendet werden.

List of publications

Journal publications

Mohamed Tarek Elewa, Lars Pastewka, Peter Gumbsch, “Sustaining pressure gradients in molecular dynamics simulations of fluid flow through periodic geometries”, Tribology letters, In preparation

Proceeding papers

Mohamed Tarek Elewa, Tarek Hatem, “Microstructural Modeling of Intrinsic Stresses in Multi-Junction Photovoltaic”, submitted to The International Conference on Power Systems, Energy & Environment 2014 Proceedings

Tarek Hatem, **Mohamed Tarek Elewa**, Salah Bedair, “Microstructural Modeling of Intrinsic Stresses in Multi-Junction Photovoltaic”, submitted to the Material Research Society 2013 Proceedings

Contributed talks to conferences

Mehdi Roozmeh, **Mohamed Tarek Elewa**, Patrick Bügel, Karin Fink and Ivan Kondov, “Scale-bridging workflows in materials science using FireWorks”, International Conference on Computational Science 2023, Prague, Czech Republic

Mohamed Tarek Elewa, Lars Pastewka, Peter Gumbsch, “Sustaining Pressure Gradients in Molecular Dynamics Simulations”, World Tribology Congress 2022, Lyon, France

Mohamed Tarek Elewa, Lars Pastewka, Peter Gumbsch, "Sustaining Pressure Gradients in Molecular Dynamics Simulations", European Community on Computational Methods in Applied Sciences 2022, Oslo, Norway

Mohamed Tarek Elewa, Lars Pastewka, Peter Gumbsch, "Pressure-driven flow in Molecular Dynamics Simulations", Society of Tribologists and Lubrication Engineers 2021, Virtual

Matous Mrovec, **Mohamed Tarek Elewa**, Tapaswani Pradhan, Sergei Starikov, Ralf Drautz, "Atomistic studies of dislocations in iron using magnetic bond order potentials", 10 Years ICAMS - International Symposium 2018, Ruhr-Universität Bochum, Germany

Mohamed Tarek Elewa, Tarek Mostafa Hatem, Salah Bedair, "Microstructural Modeling of Intrinsic Stresses in Multi-Junction Photovoltaic", Industry Academia Collaboration 2014, Cairo, Egypt

Tarek Mostafa Hatem, **Mohamed Tarek Elewa**, "Microstructural Modeling of Intrinsic Stresses in Multi-Junction Based Photovoltaic", 12th U.S. National Congress on Computational Mechanics 2013, Raleigh, North Carolina, USA

Contents

List of Figures

List of Tables

1. Introduction

1.1. Motivation

A profound understanding of tribological contacts is crucial for the design of mechanical systems. This encompasses the study of the performance, reliability and energy dissipation mechanisms for surfaces in contact. Understanding the underlying thermodynamic conditions in conjunction with mechanical loading can improve the efficiency of contacting components and cut back on substantial energy losses due to friction and wear [5].

Reducing friction through the use of lubricants is an ancient practice that was performed to transport large structures, enhance the performance of bearings on chariots and ships, and later on to build and develop more complex machinery [5, 6]. Quantification of friction took shape in the Renaissance era by Leonardo Da Vinci, who introduced the concept of the coefficient of friction. In 1699, Amontons deducted that the friction force is directly proportional to the normal load and is independent of the contact area. In 1781, Coloumb verified Amontons' findings and established a disctinction between static and kinetic friction. The nineteenth century witnessed a growing interest in tribology mainly accompanying the industrial revolution. The scientific pursue resulted in the hydrodynamic lubrication framework, which was made possible by Beauchamp Tower's experiments and Osborne Reynolds' theoretical work.

Macroscopic tribological phenomena originate from microscopic interactions. Therefore, a deeper insight on the atomic scale can provide a guideline for engineering of lubricants and contacting surfaces. Atomic scale effects become more pronounced when only a few layers of a liquid lubricant remain between the contacts i.e. as we move from the hydrodynamic lubrication to the boundary lubrication regime on the Stribeck curve [7].

In the boundary lubrication regime, the mean lubricating film thickness h is much lower than the average height of the surface irregularities, more specifically the composite standard deviation of surface roughness σ. In this regime, the lubricant film parameter $\Lambda = h/\sigma < 1$, as shown in Fig. 1.1. At such high loads p, low interfacial velocities N or low viscosities η, friction is dominated by the interaction of few molecular layers of the fluid together with solid-solid rough surface peaks (or "asperities") contact.

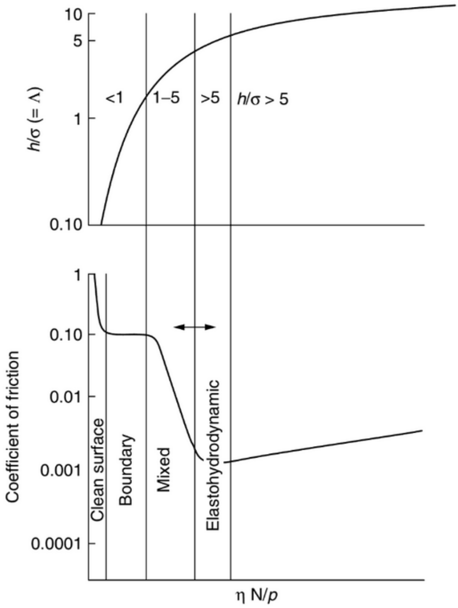

Figure 1.1.: Stribeck curve: the lubricant film parameter Λ and coefficient of friction as a function of Hersey number $\eta N/p$. The curve shows different lubrication regimes. Reprinted from Ref.[6].

The classical lubrication theory, originally developed by Reynolds [8], is usually applied in engineering lubrication problems of contacts operating in the hydrodynamic regime (sufficient contact separation and large lubricant film thickness) to predict the lubricant's pressure and load bearing capacity. The theory can be generalized to include fluid compressibility [9], slip at the walls, piezoviscosity as well as account for deviations from the Newtonian behaviour [10]. However, when the fluid properties vary significantly on a scale comparable to a few molecular diameters of the fluid lubricant, the classical equations break down [11]. In order to understand the sources of departure from the hydrodynamic framework, the implicit assumptions shall be highlighted.

Starting from the Reynolds equation, the formulation is based on the thin film approximation, which states that the lubricant flow is laminar and inertia is negligible. Another assumption is that the Navier-Stokes equations hold. Navier-Stokes linear momentum equation can be derived by inserting the constitutive relation between the applied stress tensor and the corresponding deformation into the linear momentum conservation equation. Similarly, the Navier-Stokes-Fourier energy equation is derived from inserting Fourier's heat conduction law into the energy conservation equation. Such constitutive relations may not hold for highly confined fluids [11, 12].

Additionally, the core assumption in Navier-Stokes and Reynolds equations is that the continuum description is valid, such that the ratio of the molecular mean free path to the representative length scale or the "Knudsen number" is low ($\text{Kn} < 0.1$) [5]. The break down of the hydrodynamic theory is in essence due to the strong spatial inhomogenities and the non-locality of thermodynamic, structural [13] and transport properties [14, 15] of highly confined fluids. An appropriate example would be a liquid lubricant operating in the boundary lubrication regime. In this case, the Knudsen number is large ($\text{Kn}>0.1$) and Navier-Stokes-Fourier equations lose their validity.

The flow of confined fluids is, therefore, highly non-continuum and to obtain reliable numerical solutions, microscopic details have to be coupled with the macroscopic description. The macroscopic problem can be solved with continuum numerical schemes, which can relax some of the aforementioned assumptions [9, 16, 17], while the microscopic resolution can be handled with atomistic simulations. Such simulations can be classified into stochastic Monte Carlo (MC) and deterministic molecular dynamics (MD). The earlier updates atomic positions after accepting (or rejecting) a random displacement based on the change in the system's potential energy, while the latter updates atomic positions based on solving Newton's equations of motion using a finite difference scheme. Since transport processes arise naturally in MD, it is a prime candidate for understanding tribological phenomena. A collection of historical and recent applications of molecular simulations to tribological problems is reported in Ref. [18].

Studying systems in static equilibrium, for instance under certain pressure and temperature, can be achieved with equilibrium MD. Similarly, for a system under an external perturbation, for instance a liquid lubricant between sliding contacts, non-equilibrium MD (NEMD) is the suitable tool. NEMD simulations can provide valuable insight into the underlying interactions and structural changes that occur in the boundary lubrication regime. Molecular representative volume elements (RVEs) can be crucial tools for relating the microscopic interactions to hydrodynamic properties. By reverting to the microscopic scale, fixed constitutive laws can be avoided and one can rely on the fundamental mass, momentum and energy conservation laws as well as draw direct observations from atomistic trajectories.

Therefore, the ultimate goal of simulations of fluid flow would be coupling of MD and continuum scales for capturing the atomistic effects accurately while benefiting from the reduced computational cost of macroscopic solvers [19]. Boon and Yip [20] have put this aim in other words: *".. it is one of the basic aims of research in nonequilibrium statistical mechanics to develop a unified theory of liquids which treats not only the processes in the hydrodynamic region of low (k, ω) but also molecular behavior which manifests at higher values of (k, ω)"*. The k and ω referred to here, are the wavenumber and frequency, respectively.

In this thesis, the focus would be on the atomistic scale with the greater aim in mind that the presented MD methods are to be integrated into a scale-coupling scheme. The second goal of the thesis is to investigate a phenomenon that is usually discussed from a macroscopic prespective with little insight on the microscopic behaviour, hydrodynamic cavitation.

In the last century, systematic studies on hydrodynamic cavitation started to develop. The motivation to initiate those studies sprang from cavitation relation to medical complications [21] and deleterious effects on hydraulic machinery in maritime transport [22, 23]. The damage is mainly caused by the violent collapse of bubbles on ship propellers.

Recent advances in the study of cavitation revealed how the cavitation phenomenon can play a key role in bioengineering applications, e.g. to open the blood-brain-barrier for enhanced drug delivery to the brain [24, 25] as well as biomedical applications, e.g. in lithotripsy to break down kidney stones [26] and to drive microfluidic transport in blood and cells [27]. Redesigning ship propellers [28] can be the key to avoid bubble formation and collapse and their subsequent damage.

Industrial applications of cavitations are ample. Bubbles can be used in gas-liquid reactors to increase the contact area between the phases [29]. This is useful for homogenization and breaking down of suspended particles in liquids. Cavitation can also be utilized in ultrasound cleaning devices.

Early experimental attempts to capture bubble evolution and dynamics were met with the hurdle of the immense rapidity of the formation and collapse of individual bubbles [30]. Another major dilemma was the lack of reproducibility of the exact same cavitation mechanism between different test facilities [31]. These issues could be easily circumvented with molecular dynamics simulations.

1.2. Challenge statement

A crucial part of the coupling scheme is the accurate imposition of boundary conditions on the molecular domain [32]. The molecular RVE is to represent a region where the fluid film flow is highly confined (down to few molecular diameters) between two asperities. Due to the gap height variation, the fluid experiences a pressure variation i.e. pressure gradients develop and the flow is pressure-driven.

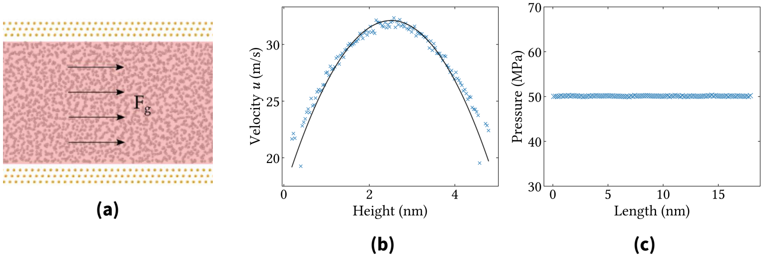

Figure 1.2.: *Gravity-fed* method **a.** schematic showing gravity force F_g applied on all fluid atoms to induce the flow. **b.** parabolic *Poiseulle-like* velocity profile along the gap height and **c.** pressure profile along the stream direction. Data from NEMD simulation of liquid argon at 100 K and external pressure of 50 MPa.

A conventional approach to induce pressure-driven flow is the “gravity-fed” method [33], where a gravity-like force is imposed uniformly on all the fluid atoms. Although, the fluid velocity profile is parabolic i.e. agrees with hydrodynamic Navier-Stokes solution for Poiseuille flow, the method fails to generate a pressure gradient, as shown in Fig.1.2.

The molecular RVEs are usually periodic in the flow direction to mimic an infinite system. Sustaining pressure gradients in periodic systems with flat walls (slab geometry) is not straightforward. Using non-flat walls could offer a solution to generating pressure gradients, however, the magnitude of the gradient can not be directly controlled.

Therefore, it is the first objective of this thesis to develop a method to sustain pressure gradients in periodic moecular domains. The second objective is to provide an atomistic insight on cavitation dynamics since the phenomenon is not widely investigated at the nanoscale in the context of hydrodynamic flow. Ultimately, the molecular simulations are to be coupled to the continuum solution. Thus, a precursory scheme to the multiscale framework is provided.

2. Non-equilibrium Molecular Dynamics of fluid flow

2.1. Molecular simulations

Non-equilibrium molecular dynamics (NEMD) originated from the need to study transport processes within and beyond the linear regime, where the flux can depend linearly or nonlinearly on the driving force. In the linear regime, transport coefficients can be obtained from equilibrium simulations, as they are related to fluctuations in the corresponding fluxes through Green-Kubo or Einstein formalisms. However, equilibrium simulations have poor signal-to-noise ratios, thus large dependence on system size and pronounced statistical errors. NEMD relies on applying an external perturbation, where the signal-to-noise ratio improves significantly with the perturbation intensity. Additionaly, NEMD simulations offer an efficient way to capture the transport processes as they occur in nature.

Three classes of NEMD simulations are the boundary-driven method, sinusoidal transverse force (STF) and homogeneous perturbations. In the boundary-driven method, a perturbation is applied physically by imposing it directly on the system, for instance moving atomic slabs or walls to mimic shearing. The pioneering work was presented in Ashurst and Hoover's paper [34] in 1975. The method offers a direct way to study non-equilibrium processes as the driving forces, occuring in nature, are mimicked in the simulation domain.

The STF method imposes a spatially periodic perturbation through an external force, represented by a sinusoidal function to comply with periodic boundary conditions. The perturbation is explicit in the equations of motion [35]. The method was proposed by Gosling et al. [36] in 1973. Using STF method, the computational expense of modelling walls is avoided, however, the heat dissipation mechanism, the thermostat, in systems under such perturbation is considered fictitious [37].

Both boundary-driven and STF methods induce significant inhomogenities in the fluid's thermodynamic properties due to the presence of walls and due to the spatially inhomogeneous perturbation, respectively. Spatial inhomogenities are intrinsic in nano-confined fluid flows and therefore need to be considered in simulations, however, if the aim is to investigate bulk properties without surface effects, these inhomogenities become undesirable. The third NEMD technique applies a spatially homogeneous perturbation by modifying the equations of motion to include external forces in a periodic system. The most prominent boundary condition used in this technique is that of sliding bricks, known as "Lees-Edwards" periodic boundary conditions [38] usually employed in conjunction with the SLLOD equations of motion [39]. The SLLOD equations of motion are derived from a Hamiltonian that includes a fictitious external field term, which drives the flow. The SLLOD algorithm is the corrected form of the DOLLS algorithm propoesed by Hoover [40].

In classical molecular dynamics, the atomic configurational energy is represented by a differentiable function of atomic coordinates. For molecular systems, this function is typically written as the dependence on a set of invariant parameters such as the bond streching, bending of valence angles and dihedral torsion [41]. These parameters constitute the bonded (intramolecular) interactions, while electrostatic, London dispersion and Pauli repulsion forces constitute the non-bonded (intermolecular) interactions. The combination of the mathematical function and the parameters set is referred to as a “force field”. Force fields parameters are usually derived from experiments and quantum mechanical calculations [42].

The set of equations to describe the force-field are

$$E_{\text{bonded}} = \sum_{\text{bonds}} K_b (b - b_0)^2 + \sum_{\text{angles}} K_\theta (\theta - \theta_0)^2 + E_{\text{dihedral}} + E_{\text{improper}} \tag{2.1}$$

$$E_{\text{non-bonded}} = \sum_i \sum_j \left[4\epsilon_i \left((\sigma/r_{ij})^{12} - (\sigma/r_{ij})^6 \right) + q_i q_j k_e / r_{ij} \right] \tag{2.2}$$

$$E_{\text{total}} = E_{\text{bonded}} + E_{\text{non-bonded}} \tag{2.3}$$

The first term in Eq. (2.1) is the sum over all bonded pairs of atoms. b, b_0 and K_b are the bond length, equilibrium bond length and stiffness, respectively. The second term is the sum over bond angles, it involves triplets of atoms. The parameters θ, θ_0 K_θ represent the angle between two bond vectors, the equilibrium angle and the angle stiffness, respectively. The dihedral term involves quadruplets of atoms and is usually represented by a cosine function. The cosine function reflects the periodicity of the dihedral rotation. Improper torsions account for rotation of atoms attached around a central atom.

The non-bonded energy term (Eq. (2.2)) sums the van der Waals (first term in large parentheses) and the electrostatic interactions between atoms in separate molecules or atoms within the same molecule separated by three or more bonds [41]. Van der Waals (pairwise) interactions consist of attractive dispersion $(1/r^6)$ term from the interaction between an instant dipole with an induced dipole, and a steep repulsion $(1/r^{12})$ term from Pauli exclusion as the atoms get progressively closer. The total pairwise energy becomes positive for a separation r_{ij} less than the van der Waals radius σ. The prefactor ϵ determines the strength of the atomic pairwise interaction i.e. the depth of the Lennard-Jones potential. Finally, the electrostatic interactions are described by Coloumb's law. q_i and q_j are the effective charges, while k_e is the Coloumb constant.

United-atom (UA) force fields treat the methine (CH), methylene (CH_2) and the methyl (CH_3) groups as pseudoatoms, while the all-atom (AA) force fields describe the carbon and hydrogen atoms explicitly. Obviously, the use of UA force fields reduces the computational expense as the number of interaction sites is reduced. However, this occurs at the expense of lack of accurate prediction of viscosity for long-chain n-alkanes [18].

Throughout this work two force fields were used, these are Groningen molecular simulation force field, GROMOS [43] and the transferable potential for phase equilibria force field, TraPPE [44]. GROMOS-54A7 was used as a benchmark in equilibrium modelling of AA and UA *n*-pentane (Ch. 3) as well to simulate model interactions within squalane (App. C), while TraPPE-UA was used more extensively throughout the rest of the thesis to model UA *n*-pentane. They mostly agree on the bonded interactions and how they are specified, for instance, both potentials include the interaction sites only at the atomic nuclei positions unlike TIP5P which considers also the lone pair positions, where there are valence electrons not shared with other atoms [41]. However, these two force fields do not agree on the dihedral term expression, where GROMOS-54A7 uses a harmonic function,

$$E_{\text{dihedral}} = \sum_{\text{dihedrals}} k_{\chi} [1 + \cos(n\chi - \sigma)] \tag{2.4}$$

where χ, K_{χ}, n and σ represent the dihedral value, energy barrier height, multiplicity and phase, respectively. In TraPPE-UA, the dihedral motion is described with the optimized potentials for liquid simulations (OPLS) [45] UA force field,

$$E_{\text{dihedral}} = \sum_{\text{dihedrals}} k_1 [1 + \cos(\chi)] + k_2 [1 - \cos(2\chi)] + k_3 [1 + \cos(3\chi)] \tag{2.5}$$

In GROMOS, the improper torsion energy is a quadratic function of the improper dihedral value. TraPPE-UA does not specify any improper rotations simply because it was designed for straight-chain alkanes. The non-bonded 1,4 (between 2 atoms in the same molecule 3 bonds away) LJ interactions are scaled differently. In TraPPE-UA, these interactions are switched off while in GROMOS-54A7, they are scaled by 0.5. Coloumb interactions are treated similarly.

2.2. Pressure-driven flow in NEMD

Various approaches have been developed to generate pressure gradients or Poiseuille flow in periodic and non-periodic RVEs. In systems with non-uniform geometries, a hydrostatic pressure difference can be generated by implementing an external field on the fluid through a channel with varying gap height, such as the nozzle model [46], a converging-diverging channel [47], or a membrane-reservoir setup [48, 49]. Instead of applying a constant force, another approach involves setting the global flow rate or center of mass velocity of the system, typically using Gaussian constraints [50]. However, in slab geometries with flat walls, applying an external field or constant flow rate would only produce uniform pressure along the flow, despite driving continuous Poiseuille flow.

The external field method, usually referred to as the “gravity-fed” method, which involves applying a constant force on all fluid atoms, has been widely used in molecular dynamics simulations [33, 51, 52] due to its simplicity and low computational cost. While this method can produce a force-driven flow in flat channels and its results align with certain hydrodynamic predictions for velocity and temperature, it does not generate a pressure gradient (see Fig. 1.2). To address the issue of generating pressure gradients in slab geometries, various approaches can be categorized into particle insertion/deletion algorithms (reservoir method) [53–55], reflecting particle method [56], and boundary-driven non-equilibrium molecular dynamics (NEMD) simulations.

Methods based on particle insertion/deletion introduce a pressure gradient by keeping fluid regions of particle insertion (the source) at a constant density, higher than regions of particle deletion (the sink). As a result, the fluid is pressure-driven from the source to the sink, and a physical pressure gradient induces the flow. The drawback of this technique is the computational burden of inserting particles, particularly when it is applied to dense fluids. An example of this computational load is visible in the particle insertion algorithm USHER [57], where a steepest descent scheme is employed to locate sites that represent minima in the potential energy landscape.

The reflecting particle method utilizes an artificial membrane to promote flow in the direction of streaming, while hindering fluid motion in the opposite direction. To achieve this, the method assigns a probability of acceptance, p, to fluid motion to the right of the membrane, while it opposes movement to the left by elastically reflecting the particles off the membrane, or accepting the move with a probability of $1-p$. This approach is successful in computing the transport coefficients of water through carbon nanotubes (CNTs), as mentioned in Ref. [58], where the results correspond to continuum predictions in regimes where the continuum theories are applicable. The main drawback is the lack of direct control over either the mass flow rates or the pressure differences, which are indirectly adjusted with the selected probabilities p.

Boundary-driven NEMD methods use perturbations that replicate the physical disturbance of the system, producing more realistic results [35]. Zhu et al. [59] applied a force to a subset of water molecules to generate flow through infinite periodic tubes of carbon nanotubes (CNTs). Despite some sampling challenges, this approach showed promising results in reproducing real permeation events. Similarly, a technique, that involves applying a force only to a part of the domain, was employed in a reservoir-membrane assembly to simulate flow through nanopores. This approach was used to measure the flow rate [60] and diffusivity [61]. For a fluid confined within slab walls, Liang et al. [62] pioneered applying local gravity not over the whole simulation domain, but only within a region of the fluid which they called the "pump". They tested the method on monoatomic compressible and incompressible Lennard-Jones fluids with different channel geometries.

Strong and Eaves [63] utilized an analogous method to regulate mass flux within nano-constricted channels. They employed an acceleration I that minimizes the cost function determined by Gauss's principle of least constraint. The constraints included in the cost function are the constant mass flux and the thermostat constraint, where the standard deviation of the thermal velocities follows the equipartition theorem. Physically, I is the acceleration field which maintains the desired mass flux by applying the force mI, while mathematically it is the constraint's Gaussian multiplier.

In this thesis, the pump method is implemented and its applicability for long-chain fluids is demonstrated. In addition to applying a perturbation using a fixed force (FF), this idea is extended to fix the particle current (FC) over a localized region of the fluid to pump the flow. This allows to control either the pressure difference (thermodynamic force) or the mass flux (thermodynamic current) directly.

2.3. Thermodynamic properties

2.3.1. Velocity

The one-dimensional steady state solution to Stokes flow for a pressure-driven fluid gives a parabolic Poiseuille velocity profile along the gap height h,

$$u(z) = \frac{1}{2\eta}\frac{\partial p}{\partial x}\left(z^2 - hz\right) + \frac{u_{\mathrm{shear}}}{h} z + u_{\mathrm{slip}} \tag{2.6}$$

where η is the dynamic viscosity, u_{shear} is the wall-shearing velocity and u_{slip} is the slip velocity defined as the velocity of the fluid at the walls relative to the wall velocity. The lower and upper walls are located at $z = 0$ and $z = h$, respectively. In the absence of shearing, u_{shear} is zero, therefore the third term vanishes and the velocity varies quadratically with the height. In the absence of pressure gradients, the first term becomes zero. Therefore, sliding the walls results in the linear Couette velocity profile.

In NEMD simulations, the streaming velocity is the center of mass (COM) velocity u_{COM} and is calculated in spatial bins along the gap height as follows

$$u_{\text{COM,bin}} = \frac{1}{N_{\text{bin}}} \sum_{i}^{N_{\text{bin}}} \dot{x}_i \tag{2.7}$$

where $\dot{x}_i$ is the x-component velocity of molecule i and N_{bin} is the number of molecules in the bin. The velocity profiles obtained from NEMD simulations together with the hydrodynamic profiles are shown in Fig. 2.1.

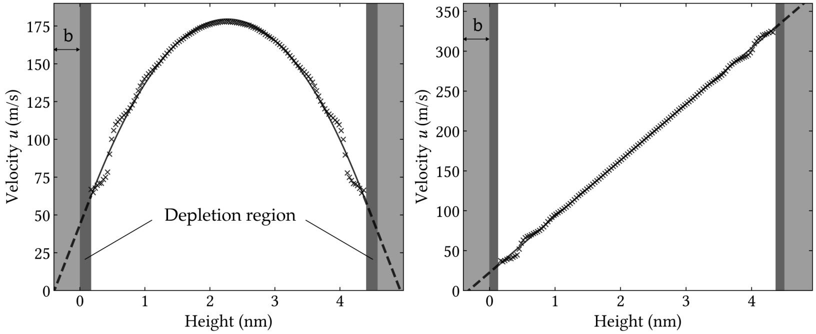

(a) **(b)**

Figure 2.1.: Velocity profiles from **a.** pressure-driven and **b.** shear-driven NEMD simulations (x markers) fit to the hydrodynamic solutions (solid lines) of Poiseuille and Couette flow profiles, respectively. The light gray and dark gray shaded regions represent the walls and the depletion regions in the fluid, respectively. These profiles show that slip (quantified through the slip length b) becomes significant for nanoconfined flows.

2.3.2. Temperature

Within the hydrodynamic framework, the classical Navier-Stokes-Fourier equation predicts can predict the fluid temperature. Starting from Newton's law of viscosity, which is expressed in tensorial form for an incompressible fluid as,

$$\underline{\sigma} = 2\eta \nabla \vec{v} \tag{2.8}$$

where $\underline{\sigma}$ is the full stress tensor (hydrostatic and viscous terms - refer to Eq. (A.5) in App. A) and $\nabla\vec{v}$ is the skew symmetric part of the velocity gradient tensor. Fourier's law of heat conduction is written as,

$$\vec{j}^e = -\lambda \nabla T \tag{2.9}$$

where $\vec{j}^e$, λ and ∇T are the heat flux vector, thermal conductivity and temperature gradient, respectively. The energy conservation equation can be expressed as,

$$\rho \frac{\mathrm{d}e}{\mathrm{d}t} = -\nabla \cdot \vec{j}^e - \underline{\sigma}^T : \nabla\vec{v} \tag{2.10}$$

By substituting Newton's law of viscosity (Eq. (2.8)) and Fourier's law of heat conduction (Eq. (2.9)) into the energy conservation equation (Eq. (2.10)), one obtains the hydrodynamic prediction for the temperature across the gap height. For Poiseuille (pressure-driven) flow in one dimension it becomes,

$$T(z) = T_0 - \frac{(\partial p/\partial x)^2}{2\eta\lambda}\left(z^4 - hz^3 + \frac{h^2}{4}z^2 - \frac{h^3}{4}z\right) \tag{2.11}$$

where T_0 is the temperature at the walls. The temperature is shown to vary quartically with the elevation in the channel z. Note that the velocity profile used here is that of Eq. (2.6) with the condition that the sliding and slip velocities are zero. The boundary conditions are that $T = T_0$ at the lower ($h = 0$) and upper ($h = z$) walls.

Additionally, the heat flow rate from the walls with an area $A_{||}$ can be expressed as a function of the temperature profile as follows

$$\dot{Q} = j^e_z A_{||} = -\lambda \frac{\partial T}{\partial z} A_{||} \tag{2.12}$$

where j^e_z is the heat flux in the z-direction. The second relation is obtained from Fourier's law of heat conduction. For Poiseuille flow, by substituting $T(z)$ from Eq. (2.11) into Eq. (2.12) at $z = h$, the heat flow rate $\dot{Q}$ becomes

$$\dot{Q} = \frac{5}{8\eta}\left(\frac{\partial p}{\partial x}\right)^2 h^3 A_{||} = \frac{5}{2}\eta\dot{\gamma}^2 h A_{||} \tag{2.13}$$

Therefore, the heat flow rate generated by the viscous shear in a fluid flow varies quadratically with the shear rate.

In NEMD simulations, the temperature of the fluid is defined from the kinetic theory as,

$$T_{\text{bin}} = \frac{1}{3\,N_{\text{bin}}\,k_{\text{B}}} \sum_i m_i (\vec{\dot{r}}_i - \vec{v}_{\text{COM}})^2 \tag{2.14}$$

where the streaming velocity $\vec{v}_{\text{COM}}$ is the vector form of the center of mass velocity (Eq. (2.7)) and k_{B} is the Boltzmann's constant. By subtracting the streaming velocity $\vec{v}_{\text{COM}}$ from the particle's lab frame velocity $\vec{\dot{r}}_i$, one obtains the peculiar (or thermal) velocity, which is thermostated. At equilibrium, the net flow is zero, thus, the center of mass velocity is zero and the temperature is computed directly from the lab frame velocities which are, in this case, equivalent to the thermal velocities.

2.3.3. Virial and mechanical stress tensors

The two expressions for measuring the stress in molecular dynamics are thermodynamic and mechanical. The thermodynamic definition of stress is based on Clausius' virial theorem [64]. The stress tensor can be written as,

$$\underline{\sigma}_{\text{virial}} = \frac{1}{V}\left[N K_B T + \frac{1}{3}\langle \underline{W} \rangle \right] \tag{2.15}$$

where V, N and T represent the volume, number and temperature of particles that consitute the domain (or subdomain). $\underline{W}$ is the internal virial tensor and the $\langle .. \rangle$ denotes an ensemble average. The internal virial can be expressed as

$$\langle \underline{W} \rangle = - \sum_{i,j<i}^{N} \vec{r}_{ij} \cdot \frac{\partial U_{ij}}{\partial \vec{r}_{ij}} \tag{2.16}$$

where $\vec{r}_{ij}$ represent the interatomic separation between atoms i and j and U_{ij} is the total energy from their pairwise, bond, angular, dihedral and improper energy contributions. The first and second terms in Eq. (2.15) represent the kinetic and intermolecular force contributions to the stress tensor, respectively. A similar expression was also derived by J. H. Irving and J. G. Kirkwood [65], where the kinetic term is computed from the atomic velocities

$$\underline{\sigma}_{\text{virial}} = \frac{1}{3V}\left[\sum_i m_i \vec{v}_i \vec{v}_i + \langle \underline{W} \rangle \right] \tag{2.17}$$

From the equipartition theorem, Eq. (2.15) and Eq. (2.17) are equivalent. Note that $\vec{v}_i$ is the thermal velocity of particle i, therefore, in a flowing fluid, the streaming velocity has to be subtracted. The virial pressure P is computed from the average of the diagonal components

$$P = \mathrm{tr}(\underline{\sigma}_{\mathrm{virial}}) \tag{2.18}$$

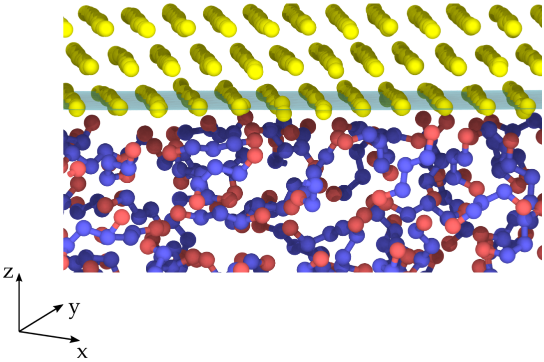

Figure 2.2.: Fluid (blue and red) and wall (yellow) atoms exerting stress on a plane.

The mechanical definition of the internal stress tensor can be derived from the sum of interatomic forces acting per unit area of the surface and the rate of change of momentum flux through the surface. Consider a plane in the wall (Fig. 2.2) with a cross-sectional area A_{xy}, atoms i and j are atomic pairs interacting across the plane and k atoms passing through. The applied mechanical stress vector on the xy-plane is,

$$\vec{\sigma}_{\mathrm{mech}} = \frac{1}{A_{xy}}\left(\sum_{ij}\vec{f}_{ij} + \sum_{k}\frac{\mathrm{d}(m_k|w_k|)}{\mathrm{d}t}\right) \tag{2.19}$$

where $\vec{\sigma}_{\mathrm{mech}} = (\sigma_{xz}, \sigma_{yz}, \sigma_{zz})$, $\vec{f}_{ij}$ is the force on solid atom j due to the pairwise interactions with a fluid atom i and w_k is the z-compnent of velocity of atom i or j. Since the wall atoms oscillate about their equilibrium positions and fluid atoms do not diffuse into the walls, there are no atoms crossing the plane i.e. the second term becomes zero. The discussion can be extended to three planes for three dimensional analysis, in this case $\vec{\sigma}_{\mathrm{mech}}$ becomes the full stress tensor $\underline{\sigma}$. However, here we consider only the applied mechanical stress on the xy-plane that separates the solid and the fluid, as shown in Fig. 2.2. Considering that the fluid is confined between two walls, $\vec{\sigma}_{\mathrm{mech}}$ becomes the average of the top (t) and bottom (b) walls,

$$\vec{\sigma}_{\mathrm{mech}} = \frac{1}{2A_{xy}} \left[\left(\sum_{ij} \vec{f}_{ij} \right)_{\mathrm{t}} - \left(\sum_{ij} \vec{f}_{ij} \right)_{\mathrm{b}} \right] \tag{2.20}$$

The thermodynamic and mechanical stress definitons are equivalent. However, there are disparities in the local stress between the two methods in regions of atomic inhomogenities e.g. free surface regions [64, 66]. The mechanical stress applies to a system with arbitrary boundary conditions while the virial expression is valid only where there are structural fluctuations (or disorder) like in a liquid. Near a free surface, the virial expression shows large oscillations which deviate from the uniform stress distribution of the mechanical expression. For that reason, in this work, the thermodynamic virial was used for computing the pressure of the confined fluid away from the surface i.e. in the fluid bulk, while the mechanical stress was used for measuring the stress on the walls.

2.3.4. Surface tension

The surface tension γ of a liquid-vapour interface is a principal parameter for the computation of the nucleation rate of a void according to the classical nucleation theory as well as the calculation of the bubble radius from the macroscopic relations. It is defined as the force per unit length that resists the expansion of the liquid. For the canonical (NVT) and Gibbs (NPT) ensembles, γ is defined as [67],

$$\gamma = \left(\frac{\partial F}{\partial A} \right)_{\mathrm{N,V,T}} = \left(\frac{\partial G}{\partial A} \right)_{\mathrm{N,P,T}} \tag{2.21}$$

where F, G and A are the Helmholtz and Gibbs energies and the surface area of the interface, respectively. For an arbitrary interatomic potential, Gloor et al. [68] developed the “test-area” method to compute γ from Eq. (2.21). By applying an infinitesimal perturbation to the surface area ΔA of a reference system, while keeping the volume fixed, the difference in Helmholtz energy between the unperturbed (0) and the perturbed (1) systems can be expressed in terms of the difference of their configuration energy ΔU as

$$\Delta F = -k_\mathrm{B} T \ln\langle \exp\bigl(-\Delta U / k_\mathrm{B} T\bigr)\rangle \tag{2.22}$$

Therefore,

$$\gamma = \lim_{\Delta A \to 0} \left(\frac{\Delta F}{\Delta A}\right) = -\frac{k_\mathrm{B} T}{\Delta A} \ln\langle \exp\bigl(-\Delta U / k_\mathrm{B} T\bigr)\rangle \tag{2.23}$$

where T is the temperature and $\Delta U = U_1 - U_0$. To perform a test-area computation of the surface tension, the energy of the uperturbed system U_0 is computed, the positions of the unperturbed system are then scaled and the perturbed system energy U_1 (and so ΔU) is obtained.

For the case of a pairwise additive potential, the surface tension can be expressed in terms of the normal and tangential components of the virial tensor. Normal and tangential are defined with respect to the interface surface. For a planar interface between the liquid and vapour phases at equilibrium, the off-diagonal components of the stress tensor are zero while the diagonal components are non-zero. Considering an interface in the xy-plane, the normal component is $p_\mathrm{N} = \sigma_{zz}$ and the tangential component p_T is the average of the other two diagonal components i.e. $p_\mathrm{T} = \frac{1}{2}(\sigma_{xx} + \sigma_{yy})$. The liquid-vapour surface tension becomes

$$\gamma = \frac{1}{2} \int_0^{L_z} \langle \sigma_{zz} - \frac{1}{2}(\sigma_{xx} + \sigma_{yy})\rangle \, \mathrm{d}z \tag{2.24}$$

where the integral is over the domain length in the z-direction L_z. A factor of 1/2 is used to account for 2 liquid-vapour interfacial surfaces. The stress tensor used here is the virial tensor computed from the Irving-Kirkwood expression, Eq.(2.17), where atoms i and j contribute to the pressure tensor in a certain region only if the line joining them intersects that region [67]. As mentioned earlier, the virial expression gives large oscillations at free surfaces, however, the contribution of theses oscillations is limited only to a small region in space, thus does not affect the time-averaged values of the stress components significantly.

2.4. Transport properties

The transport coefficients describe the relaxation of dynamical variables on the macroscopic scale [42]. Mechanical and thermal transport coefficients, which appear in the hydrodynamic equations, can be obtained using mechanical methods [69]. They could be obtained from equilibrium and non-equilibrium MD simulations.

For a system at equilibrium, transport coefficients are related to time correlation functions through linear response theory [42]. Green-Kubo and Einstein relations relate the transport coefficient γ to equilibrium fluctuations of the thermodynamic variable A. The Green-Kubo relation reads

$$\gamma = \int_0^\infty \langle \dot{A}(t)\dot{A}(0)\rangle_{t_0}\ \mathrm{d}t \tag{2.25}$$

while the Einstein relation is

$$\gamma = \lim_{t\to\infty} \frac{\mathrm{d}}{\mathrm{d}t}\frac{1}{2}\left\langle \left(A(t) - A(0)\right)^2 \right\rangle_{t_0} \tag{2.26}$$

where $< .. >_{t_0}$ indicates an average over several time origins.

In systems away from equilibrium, NEMD simulations can be employed to compute the transport coefficients by utilising the linear constituitve relations between the flux of a conserved quantity to the gradient in the density of that quantity (for instance Eq. (2.8)). Both the flux and the gradient are directly measurable from a NEMD simulation. NEMD methods can be superior to their equilibrium counterparts in calculating transport coefficients. One reason is that the transport coefficients computed from equilibrium simulations, especially from the Green-Kubo integral, are more prone to accumulation of statistical errors [70]. This is mainly rooted in accumulation of errors in the time integration of the auto correlation functions and the difficulty to verify convergence of the integral. Moreover, NEMD allows direct observations (for instance of structural changes) to be performed.

In this work, equilibrium simulations in conjunction with the Green-Kubo relations were performed to provide the zero-shear viscosity. At equilibrium, the Green-Kubo relation to obtain the shear viscosity is expressed as follows,

$$\eta = \frac{V}{k_\mathrm{B}T}\int_0^\infty \langle \sigma_{ij}(t)\sigma_{ij}(0)\rangle_{t_0}\ \mathrm{d}t \tag{2.27}$$

where σ_{ij} are the off-diagonal component of the virial stress tensor. It has been shown that averaging over all stress components and over only the three off-diagonal components, yields similar results [71].

In NEMD simulations, the interfacial shear rate $\dot{\gamma}$ was obtained from the derivative of the parabolic profile at $z = 0$, $\frac{\partial u}{\partial z}|_{z=0}$. The fluid viscosity at the interface was obtained from the constituitve relation $\sigma_{xz} = \eta\dot{\gamma}$, where σ_{xz} is the wall shear stress.

Fluid slipping against the walls is an important hydrodynamic phenomenon that reflects on the physical and chemical properties of the wall-fluid interface. In the continuum framework, the no-slip boundary condition is usually assumed i.e. the relative fluid-wall velocity is zero. However, for nanoconfined flows on smooth surfaces or hydrophobic capillaries, slip can exceed the length scale of a molecular diameter by orders of magnitude [72], thus impacting the fluid transport significantly. Slip was also observed experimentally [73]. Understanding and controlling slip in nanofluidics can increase the efficiency of energy harvesting.

Slip is quantified by the slip length b, which is the extrapolation length (Navier length) in the wall where the velocity profile vanishes. For a Newtonin fluid, the slip length is related to the slip velocity u_{slip} through Navier boundary condition and to the dynamic viscosity through a surface friction coefficient k_{F} as follows,

$$b = u_{\text{slip}}/\dot{\gamma} = \eta/k_{\text{F}} \tag{2.28}$$

In NEMD simulations, the global slip length b at a certain wall is obtained from the linear extrapolation of the velocity profile to zero, as shown in Fig. 2.1 for shear- and pressure-driven flows. This is according to the definition of b in Eq. (2.28), where $\dot{\gamma}$ is evaluated at the wall. The slip velocity can be obtianed from Eq.(2.28) if b is known or simply the relative velocity at the wall-fluid interface.

2.5. Structural properties

Near the walls, the fluid atoms possess an ordered structure induced by the walls. The static structure factor quantifies the degree of in-plane ordering in the fluid. It can be expressed as the sum of Fourier components of the density [13, 74],

$$S(\vec{k}) = 1/N_l \left| \sum_j \exp\left\{ i\vec{k} \cdot \vec{r}_j \right\} \right|^2 \tag{2.29}$$

where N_l is the number of the fluid atoms in the investigated layer, $\vec{k}$ and $\vec{r}_j$ are the two-dimensional wave vector $\vec{k} = (k_x, k_y)$ and position vector $\vec{r} = (x_j, y_j)$. The summation is over j atoms in the layer of interest.

In analogy to the transport coefficients being related to the time correlation functions of certain thermodynamic variables, the structure factor is related to the density autocorrelation function. In other words, it quantifies the density response of a system at equilibrium to a weak external perturbation of wavelength $2\pi/k$ [75].

2.6. Thermostating strategies

By default, MD trajectories sample microstates in the microcanonical ensemble [76]. However, dissipating the viscous heating of the confined flowing lubricant requires a temperature control strategy. Selecting an appropriate temperature control algorithm, a “thermostat”, for the confined fluid flow system is essential for accurate representation of the flow dynamics and consequently accurate evaluation of the transport coefficients.

Thermostat algorithms

Generally, thermostats modify the system’s Hamiltonian or equations of motion [42]. This is done through extending the system’s Lagrangian equation of motion, weak-coupling or stochastic-coupling to a thermal bath. For reference, one can write the unmodified Hamiltonian ($\mathcal{H}$) equations of motion in terms of the generalized coordinates r_i and momenta p_i as follows [77],

$$\dot{\vec{r}}_i = \frac{\partial \mathcal{H}}{\partial \vec{p}_i} = \frac{\vec{p}_i}{m_i} \quad \text{and} \quad \dot{\vec{p}}_i = -\frac{\partial \mathcal{H}}{\partial \vec{r}_i} = \vec{F}_i \tag{2.30}$$

where $\vec{F}_i$ is the force acting on particle i from interatomic interactions with the surrounding particles. Thermostating can be applied locally or globally [78, 79]. Local thermostats couple indvidual particle energies to a thermal bath, where the energy dissipation/addition from/to the particle occurs based on the particle’s velocity. Global thermostats control the temperature through uniform energy dissipation/addition according to a globally-defined temperature.

Thermostats can operate in a stochastic or deterministic manner. For stochastic thermostats, the momentum part of the equation of motion can be written in the form of the Langevin equation,

$$\dot{\vec{p}}_i = \vec{F}_i - \zeta_i \vec{p}_i + \sigma \vec{R} \tag{2.31}$$

where $\vec{R}$, σ, ζ_i are a stochastic (random) force, a parameter that determines the strength of the random force and atomic damping coefficient, respectively. The second and the third terms in Eq. (2.31) are the deterministic and the stochastic elements, respectively.

For deterministic thermostats, the stochastic force is discarded so the equation of motion becomes,

$$\dot{\vec{p}}_i = \vec{F}_i - \zeta \vec{p}_i \tag{2.32}$$

Note that the damping coefficient ζ expressed here as the same for all atoms i.e. global scaling, however, deterministic thermostats can also apply local scaling.

Throughout this work, the focus is only on three thermostats. The first is stochastic, namely the Langevin thermostat and the others are deterministic, namely the Berendsen and the Nosé-Hoover thermostats. Therefore, a brief description is provided here and their shortcomings/strengths in a non-equilibrium setting is demonstrated in Ch. 4 and a detailed discussion is provided in App. B.

First, the Langevin thermostat [80] uses Eq. (2.31) to simulate a system interacting with a thermal bath. The equation of motion is Eq.(2.31), with the random force $\vec{R}_i$ being Gaussian with zero mean. The parameter σ is related to ζ through the fluctuation-dissipation theorem,

$$\sigma = \sqrt{2\zeta k_{\mathrm{B}} T} = \sqrt{2m\gamma k_{\mathrm{B}} T} \tag{2.33}$$

where γ is the damping constant per unit mass. The generated trajectory samples the canonical ensemble at temperature T. The dynamics resulting from Eq.(2.31) are very smooth, such that the velocity trajectory is continuous, but time-irreversible [76]. The thermostat does not conserve the total momentum i.e. Langevin thermostat is not Galilean invariant. If the thermostat is applied directly on a shearing fluid or a sliding wall, one can recover the invariance by switching off the thermostat in the shearing direction.

Berendsen thermostat [81] offers a weaker formulation of the velocity scaling algorithm. The momentum equation of motion can be written as

$$\dot{\vec{p}}_i = \vec{F}_i - \zeta \vec{p}_i \quad \text{using} \quad \zeta = \frac{1}{2\tau}\left(1 - \frac{T_0}{T}\right) \tag{2.34}$$

where ζ is the damping coefficient that acts here as a Lagrangian multiplier for the Gaussian constraint of $\dot{T} = 0$. Note that $\zeta = m\gamma$ still holds as for the Langevin thermostat. The equations of motion are not time-reversible.

At each time step, the momenta are scaled by the scaling factor λ expressed as following,

$$\lambda = \frac{\vec{p}'}{\vec{p}} = \sqrt{1 + \frac{\delta t}{\tau}\left(\frac{T_0}{T} - 1\right)} \tag{2.35}$$

where δt is the time step, τ is a parameter representing the strength of coupling the system to the thermal bath and T_0 is the desired temperature. As $\tau \longrightarrow 0$, the equilibrium distribution of particle postions $\vec{r}$ and momenta $\vec{p}$ approaches the isokinetic form and as $\tau \longrightarrow \infty$, the distribution is closer to the microcanonical form. Therefore, the thermostat does not capture the correct canonical fluctuations.

Nosé [82] used an “extended system” technique to include an artificial coordinate s with mass Q and an associated momentum p_s. The additional degrees of freedom represent that of a reservoir. The equations of motion for the extended system sample the canonical ensemble of the real system [42]. Hoover [40] converted the extended system variables to the real system variables in order to avoid time scaling issues. The Nosé-Hoover equations of motion for the real and extended systems are [42],

$$\dot{\vec{p}}_i = \vec{F} - \zeta \vec{p}_i \quad \text{using} \quad \zeta = p_s/Q \tag{2.36a}$$

$$\dot{p}_s = \vec{p} \cdot \vec{p}/m - dk_\mathrm{B}T \tag{2.36b}$$

where d is the number of degrees of freedom. These equations are smooth and time-reversible, however they are non-Hamltonian (although still Lagrangian) but they preserve a Hamiltonian-like quantity. The parameter Q governs the coupling to the thermal reservoir. As $Q \longrightarrow \infty$ (weak coupling), the microcanonical distribution is recovered and as $Q \longrightarrow 0$, high-frequency temperature oscillations will occur [76]. Finally, the Nosé-Hoover thermostat suffers from lack of ergodicity in some cases where the canonical distribution might not be sampled correctly or is obtained only after long equilibration time.

Thermostating a confined fluid in non-equilibrium

For fluid systems undergoing shear flow, the dynamics of the system are not only dependent on how the equations of motion are modified (i.e. on the thermostat algorithm) but also on how and where the thermostat is applied.

The first question deals with whether the thermostat assumes a certain streaming velocity profile, a “profile-biased thermostat” (PBT) or it does not assume a certatin form “profile-unbiased thermostat” (PUT) [83]. To further explain, a typical momentum thermostated equation in a non-equilibrium setup is written as,

$$\dot{\vec{p}}_i = \vec{F}_i - \zeta m(\dot{\vec{r}}_i - \vec{v}_{\mathrm{COM}}) \tag{2.37}$$

At equilibrium, there is no flow and therefore $\vec{v}_{\mathrm{COM}}$ is zero. Away from equilibrium, it is non-zero and can be computed on the basis of an assumed profile like the linear Couette profile (PBT) or self-consistently during the simulation (PUT). The PUT can be incoporated with any of the aforementioned thermostats. Since the main motive behind a PUT is to simulate flows with high Reynolds numbers ($Re = 10^3 - 10^5$) and this is beyond the scope of this work, a PBT was sufficient.

Secondly, a thermostat can be applied on the confined fluid, on the walls or on both. These configurations yield different temperature profiles, especially thermostating-only-the-walls (here referred to as TW) and thermostating-only-the-fluid (TF) systems. It has been shown that TW systems generate the correct dynamics for a fluid undergoing high shear rates. This strategy was even superior to TF systems with a profile-unbiased and -biased Nosé-Hoover [79, 84] and to TF systems with a stochastic algorithm such as the Langevin and DPD thermostats [79]. Toton et al. [85] demonstrated that for tribological systems, a stochastic thermostat, applied in all directions to a portion of atoms in the sliding walls, is the most appropriate strategy. They compared this setup to a stochastic thermostat applied to both the fluid and the walls in the perpendicular-to-load perpendicular-to-flow direction and in all directions.

Finally for TW systems, thermostating the wall atoms can be performed on the layer(s) in contact with the fluid while the outermost atoms are rigid or on the middle layer(s) between outermost rigid atoms and innermost thermostat-free (i.e. NVE) atoms [86, 87]. The main difference between the two arrangements is in the thermal transport between the fluid and solid interfaces or more specifically the thermal (Kapitza) resistance [88, 89]. However, this does not affect the heat flow rate from the flowing fluid. This is demonstrated in App. B.

2.7. Hydrodynamic Cavitation

Liquids exhibit an elasticity in addition to their fluidity. Liquids are more akin to solids than to gases in terms of thermal motion of the molecules and their small amplitude vibrations about a quasi-equilibrium position [90]. In analogy to void formation when a solid is undergoing diffusion creep, a pocket of vapour can form in a liquid under tension for a certain period of time as soon as it yields.

The spontaneous nucleation of such pockets of vapour or “bubbles” occurs when a liquid experiences a local pressure drop below the vapour tension of the liquid. The process is known as “cavitation”, which is a nucleation process controlled by stochastic events. Cavitation is similar to boiling physically such that both infer liquid rupture but both proccesses differ thermodynamically. A clear distinction can be drawn from the fact that the respective regimes on the phase diagram are different (see Fig. 2.3).

In boiling, bubble nucleation occurs when the liquid temperature overcomes the saturation temperature at a roughly constant pressure while in cavitation it occurs when the liquid pressure drops below the saturation pressure at a roughly constant temperature. A cavitating liquid is a subcooled liquid i.e. a vapour phase exists even below the boiling point, while a boiling liquid is superheated. Latent heat flow is minor and the liquid’s inertia control the dynamics in the cavitating liquid and the opposite is true for the boiling liquid [91]. Indeed the temperature of the liquid can promote or hinder cavitation [29]. As apparent from Fig. 2.3, the pressure at which the transition from liquid to vapour takes place, the “saturation pressure”, becomes lower at lower temperature. Complex cavity geometries may arise around ship propellers or in pumps. A detailed and visual summary of different configurations is summarised in Ref. [92].

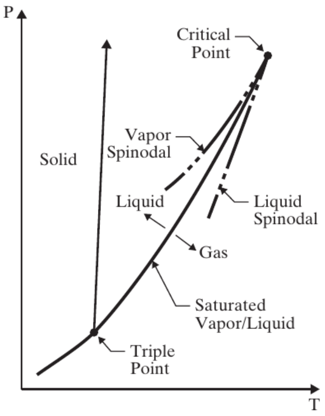

Figure 2.3.: A typical phase diagram. Reprinted from Ref.[90]

The two main classicfications for cavitation are stable and inertial cavitation. Stable cavitation can be generated from ultrasonic excitation [25] with repetitive expansion and contraction of the bubble and can be characterized by subharmonic/ultraharmonic emissions [24]. Inertial cavitation is the culprit behind cavitation damage. It is characterized by wideband emissions and results from an asymmetric contraction and expansion of a bubble followed by a violent collapse. The bubble can be driven by an ultrasonic wave like a shock wave propagating in the fluid [27] or as a product of the fluid flow through a constriction thus experiencing a drop in pressure at the expansion. The latter is usually refered to as “Hydrodynamic cavitation” and is the subject of investigation in this thesis.

2.7.1. Cavitation Inception

A drop in the local pressure of the flowing liquid below its vapour pressure ($p_l < p_v$) can cause hydrodynamic cavitation. Therefore, the usual setup to investigate cavitation involves a liquid flow through a channel of non-uniform geometry, for instance on a rough surface or through a venturi or an orifice. According to Bernoulli’s principle, as the cross section is narrower (in the constriction or in the converging region), the fluid pressure drops as it accelerates. The one-dimensional relation between the fluid's pressure and velocity ignoring dissipation losses can be expressed as follows,

$$P_1 + \frac{1}{2}\rho u_1^2 = P_2 + \frac{1}{2}\rho u_2^2 \tag{2.38}$$

where the subscripts 1 and 2 denote either a narrow or a wide region.

The degree of cavitation development is characterized by the cavitation index K [90],

$$K = \frac{p_\infty - p_\mathrm{v}(T_\infty)}{\frac{1}{2}\rho_l u_\infty^2} \tag{2.39}$$

where p_∞ and u_∞ are the pressure and velocity of the liquid away from the bubble, respectively. While ρ_l and p_v are the density and vapour pressure of the liquid at temperature T_∞. A large K means a non-cavitating single-phase liquid flow. As K becomes smaller, cavitation becomes more favorable and occurs at the incipient cavitation number K_i. Above K_i, the hydrodynamic parameters (such as lift, drag and efficienct) are independent of K [23].

The bubble growth and collapse are largely affected by the thermodynamic properties of the liquid and vapour phases as well as the geometry of the bounding surfaces. Regarding the thermodynamic aspect, the liquid-gas transition is a first order transition, characterized by a discontinuity in the derivative of the Gibbs free energy with respect to a thermodynamic variable. The energy barrier ΔG to bubble nucleation can be expressed as

$$\Delta G = 4\pi r^2 \gamma - \frac{4}{3}\pi r^3 \Delta p \tag{2.40}$$

where $\Delta p = p_\mathrm{v} - p_\mathrm{l}$, γ is the surface tension and r is the bubble radius. The first term represents the energy stored in the bubble surface and the second term is the work done on/by the bubble volume. The critical energy ΔG_c or the energy of formation is derived from substituting r with a critical radius, at which the bubble nucleation occurs. The critical energy for nucleation is expressed as

$$\Delta G_\mathrm{c} = 16\pi\gamma^3/3\Delta p^2 \tag{2.41}$$

According to the classical nucleation theory (CNT), the probability of thermal fluctuations leading to the formation of a bubble is related to the kinetic energy of the molecules k_BT through Gibbs number Gb such that $Gb = \Delta G_c/k_BT$. Finally, the nucleation rate J takes the form

$$J_{\mathrm{CNT}} = J_0 \exp\left\{ \frac{-16\pi\gamma^3}{3k_BT(p_l - p_v)^2} \right\} \tag{2.42}$$

where the prefactor $J_0 = n\sqrt{\frac{2\gamma}{\pi m}}$ as suggested by Blander and Katz [93], where n and m are the number density and the mass of the molecule, respectively.

In molecular dynamics, the nucleation rate can be extracted from the mean lifetime method suggested by Baidakov and Tipeev [94]

$$J_{\mathrm{MD}} = \lambda/V = (\tau V)^{-1} \tag{2.43}$$

where V is the total fluid volume and τ is the expectation time for the appearance of the cavity nucleus. The nucleation rates measured in MD were reported to be 8-20 orders of magnitude higher than those obtained from CNT at temperatures below the triple point temperature [95, 96].

Experimental attempts to study cavitation [97–99] could only access the lengthscale of microbubbles. Hence, molecular dynamics could provide valuable insight on cavitation in nanoconfined fluids.

2.7.2. Cavitation Dynamics

The first analysis on cavitation dynamics in a liquid was performed by Lord Rayleigh in 1917, who solved the problem of pressure in a liquid at the collapse of a spherical cavity [100]. This problem was originally presented by Besant in 1859. In 1949, Milton S. Plesset wrote down the equation of motion of such cavity [101].

Lord Rayleigh [100] derived a second-order differential equation which describes the motion of a spherical cavity in an infinite homogeneous fluid,

$$\rho[R\ddot{R} + \frac{3}{2}\dot{R}^2] = p_v - p_\infty = \text{ constant} \tag{2.44}$$

where R, $\dot{R}$ and $\ddot{R}$ are the cavity radius, interface velocity and acceleration. p_∞ is the pressure in the liquid far from the cavity. This equation entails the dynamics of nucleation and collapse of a spherical bubble.

Milton S. Plesset [101] extended Eq. (2.44) by including the bubble's surface tension. Additionally, he relaxed the assumption of a constant liquid pressure. The Rayleigh-Plesset (RP) equation describes the bubble dynamics on the hydrodynamic scale and can be written as

$$\rho[R\ddot{R} + \frac{3}{2}\dot{R}^2] = p_\mathrm{v} - p_\infty(t) - \frac{2\gamma}{R} \tag{2.45}$$

The pressure $p_\mathrm{v} - p_\infty$ is the driving term for bubble growth. It can also be thought of as the the tensile strength of the liquid.

Plesset summarized the approximations considered as follows: The bubble is acted upon by a spherically symmetric pressure field. This is not the case due to the presence of pressure gradients. He anticipated that these gradients are the source of asymmetry in the bubble shape. Secondly, The bubble is in an infinite liquid medium. The ramification of this assumption would be an exaggerated liquid ineria $\dot{R}^2$. Thirdly, The bubble's vapour pressure p_v and temperature are constant, however, there is heat transfer into the bubble during growth and from the bubble during collapse. It is also assumed that the liquid and vapour are Newtonian and incompressible. The incompressibility assumption becomes invalid especially approaching the collapse as $\dot{R}$ approaches the gas acoustic velocity. Additionaly, an inviscid fluid is assumed i.e. the effects of viscosity are ignored, although viscosity counteracts the bubble growth. Finally, the bubble is free of any dissolved gas.

In the review paper by Plesset and Prosperetti [91], they got rid of the last two assumptions. The full dynamical equation that included viscous effects and the partial pressure of the non-condensable gas p_g inside the bubble was expressed as,

$$\rho[R\ddot{R} + \frac{3}{2}\dot{R}^2] = p_\mathrm{v} - p_\infty(t) + p_\mathrm{g}(t) - \frac{2\gamma}{R} - 4\eta\frac{\dot{R}}{R} \tag{2.46}$$

p_g accounts for the pressure exerted by the dissolved gas contained in the bubble. This originates from the migration of gas through the bubble surface by diffusion [92]. It is only significant at the very early stages of formation or late stages of collapse. Gilmore [102] introduced the compressibility effects for the evolution of spherical bubbles.

The surface curvature corrections δ by Dzubiella [103] and Block et al. [104] allows the use of the liquid-vapour planar surface tension γ_∞ from Sec. 2.3.4

for spherical or cylindrical shapes. The surface tension γ in Eq. (2.45) for spherical and cylindrical bubbles can be expressed as,

$$\gamma/\gamma_\infty = 1 - 2\delta_\mathrm{T}/R \quad \text{(for spheres)} \tag{2.47a}$$

$$\gamma/\gamma_\infty = 1 - \delta_\mathrm{T}/R \quad \text{(for cylinders)} \tag{2.47b}$$

where the higher order terms were truncated. δ_T is the Tolman length which is a measure of the deviation of the curved surface γ from the planar limit [67].

At equilibrium, the RP equation, Eq. (2.45), reduces to the Young-Laplace equation by ignoring the dynamical terms and assuming a bubble that contains only the vapour of the liquid, i.e. considering only the static interface and neglecting p_g,

$$p_\mathrm{v} - p_\infty(t) = \frac{2\gamma}{R} \tag{2.48}$$

The Young-Laplace equation (Eq. (2.48)) with curvature effects for a spherical cavity can be written as,

$$p_\mathrm{v} - p_\infty = \frac{2\gamma_\infty}{R}\left(1 - \frac{2\delta_\mathrm{T}}{R}\right) \tag{2.49}$$

which describes an unstable equilibrium between the liquid and the vapour. Notice that the pressure p_∞ here is assumed constant in time. The Young-Laplace equation was found valid at the nanoscale from simulations of pressurized water pressed out of nanopore [105] and for solid-liquid interfaces [106].

2.7.3. Modelling of Cavitation

Continuum description

Reynolds equation fails to capture the hydrodynamic cavitation phenomenon. It predicts negative pressures, that if one decides to set these negative pressure to the cavitation pressure will lead to unpreserved mass [107]. Approaches that act as a remedy to this problem are discussed below.

A mass-preserving cavitation theory was developed by Jakobsson, Floberg and Olsson (JFO) [108, 109] through a set of self-consistent boundary conditions to the Reynolds equation. These boundary conditions originate from applying the mass conservation at the full-film/cavitation boundary [110]. They are known as rupture and formation boundary conditions. The JFO procedure is based on the assumption of a constant pressure in the cavitated region i.e. $\nabla P = 0$. The domain is assumed to consist of regions of either saturated liquid with pressure $p > p_c$ or cavitated regions with pressure $p = p_c$. The difficulty arises when cavitation is encountered multiple times in the lubricant film [111].

Elrod and Adams (EA) [112] avoided the complexities of locating the cavitating regions. They rather modified the Reynolds equation with a universal differential equation that employs a switch function in the pressure-density relation to remove the Poiseuille portion of the mass flux in the cavitated region. This is needed since the pressure in cavitated regions is assumed constant (i.e. $\nabla P = 0$) from the continuum prespective. Also the cavitaing flow is assumed to be due to the shear-driven contribution [107].

Elrod [110] then redefined the pressure-density relation (with the switch function encoded) in a way that describes the fluid as incompressible in the saturated zones and as a homogeneous compressible gas-liquid mixture in the cavitated zones. Obtaining a converged numerical solution can be challenging in some cases [111]. Vijayaraghavan and Keith [107] developed a continuous interpretation of the EA algorithm. They implemented a more robust finite difference scheme which also includes the effect of compressibility of the fluid.

In all the aforementioned models, the pressure-density relation is based on a constant bulk modulus assumption, which is valid in a limited pressure range [10]. Sahlin et al. [113] developed a cavitation model that accounts for a variable bulk modulus and uses a more complex equation of state namely the Dowson-Higginson equation of state [114], which relates the fluid density to pressure as follows,

$$\frac{\rho}{\rho_\mathrm{c}} = \frac{C_1 + C_2(p - p_\mathrm{c})}{C_1 + p - p_\mathrm{c}} \tag{2.50}$$

where ρ_c and p_c are the cavitation density and pressure, C_1 and C_2 are lubricant-dependent coefficients. Sahlin et al. used the EA algorithm with the switch function to suppress the Poiseuille term.

A model that treats the liquid and vapour as a homogenized mixture was presented by Bayada and Chupin [115]. The ppressure-density relation is a smooth function that can be used in the entire domain of three distinct regions: pure liquid, pure vapour and a mixture of both. Considering a void fraction $\alpha = (\rho - \rho_\mathrm{l})/(\rho_\mathrm{v} - \rho_\mathrm{l})$, the cavitation pressure can be written as

$$p_\mathrm{cav} = \rho_\mathrm{v} c_\mathrm{v}^2 - N \log\left(\frac{\rho_\mathrm{v}^2 c_\mathrm{v}^2}{\rho_\mathrm{l}^2 c_\mathrm{l}^2}\right) \quad \text{with} \quad N = \frac{\rho_\mathrm{v} c_\mathrm{v}^2 \rho_\mathrm{l} c_\mathrm{l}^2 (\rho_\mathrm{v} - \rho_\mathrm{l})}{\rho_\mathrm{v} c_\mathrm{v}^2 - \rho_\mathrm{l} c_\mathrm{l}^2} \tag{2.51}$$

where ρ and c denote the density and speed of sound in the respective liquid (l) or vapour (v). The pressure-density relation is expressed as follows

$$p(\rho) = c_\mathrm{v}^2 \rho \quad \text{if}\, \alpha > 1 \tag{2.52a}$$

$$p(\rho) = p_\mathrm{cav} + (\rho - \rho_\mathrm{l}) c_\mathrm{l}^2 \quad \text{if}\, \alpha < 0 \tag{2.52b}$$

$$p(\rho) = p_\mathrm{cav} + N \log\left(\frac{\rho_\mathrm{v} c_\mathrm{v}^2 \rho}{\rho_\mathrm{l}(\rho_\mathrm{v} c_\mathrm{v}^2 (1-\alpha) + \rho_\mathrm{l} c_\mathrm{l}^2 \alpha)}\right) \quad \text{if}\, 0 < \alpha < 1 \tag{2.52c}$$

In this work, the equations of state used in the continuum calculations were the cubic and Dowson-Higginson with a realization of the Elrod-Adams algorithm. Additionally, the Bayada and Chupin EoS was utilized as an advanced model to depict cavitation.

Atomistic models

Macroscopic models treat the lubricant cavitated and non-cavitated regions either as distinct regions or as a homogeneous compressible fluid. Consequently, the specific occurrences within the cavitation region are missing. Furthermore, the surface tension and mass transfer between vapour and liquid are not included.

This indeed can be remedied with a separate description of the dynamics using for instance the Rayliegh-Plesset equation. However, that still lacks a complete description of the bubble dynamics, especially at the final stage of collapse [29], when the bubble radius diminishes to zero and the violent collapse releases a shock wave.

Attempts to study cavitation have been focused on creating the bubble artificially within a monoatomic fluid medium. A cavity can be created by removing atoms within a certain radius from the center of a cubic box and the collapse can then be monitored as the liquid fills the void [103, 116, 117]. Hołyst et al. [116] formed a cavity in large molecular domains using this method and reported that the collapse of the cavity agrees with the RP equation. They noted that, for argon fluid interacting with a truncated Lennard-Jones potential, neither the surface tension nor the viscous term affected the dynamics significantly. An obvious shortcoming of this “void creation” method is that the bubble formed is inertial, rather than in a hydrodynamic flow scenario, in addition to that, only the collapse dynamics can be monitored.

Similarly, Lugli et al. [29] initialized a cavity within cubic boxes of water using a repulsive Lennard-Jones potential. To study the collapse, the repulsive LJ potential is switched off while applying a constant pressure. They reported a violent collapse of the bubble where the radius evolves according to the expression,

$$R(t) = R_0[(t_c - t)/t_c]^{2/5} \tag{2.53}$$

where R_0, t_c are the initial radius and the time of collapse. In the bubble’s lifetime, R_0 is the crtitical bubble radius, after which the collapse starts. Eq. (2.53) is derived from integrating $R\ddot{R} + \frac{3}{2}\dot{R}^2 = 0$, which represents the collapse of a spherical void. They also concluded that the collapse is dominated by the velocity term $3/2\rho\dot{R}$, while the surface tension and viscosity play a minor role in the collapse dynamics, a similar conclusion to Ref.[116].

The entire process of bubble nucleation and collapse can be monitored by heating the fluid in a local region [118]. Although this is considered boiling rather than cavitation, the dynamics involved are the same. Okoumra et al. [118] found that the nucleation and collapse of the heated nano bubble agree with RP equation.

Another attempt to create a cavity was achieved by representing a bubble as a particle with low mass and no charge [119], where the "bubble particle" interacts with the rest of the liquid through a time-dependent Lennard-Jones potential. The Van der Waals radius $\sigma(t)$ is replaced with the bubble radius $R(t)$ and it is represented by a sinsuoidal function that undulates between minimum and maximum radii to represent nucleation and collapse events. The low mass condition allows the bubble to translate. The viscosity was obtained as a fitting coefficient from fitting the RP to the bubble radius time-series MD data.

In this thesis, cavitation is rather a product of the presssure-driven fluid flow. This provides a more realistic approach to study cavitation as they occur in reality. The measurement of the bubble radius was possible through the “alpha-shape” algorithm [120]. The probe radius used was set to 6Å, which was adquate to capture the bubble’s surface details.

3. Equilibrium properties of the lubricant

The purpose of this chapter is to provide benchmark simulations to the NEMD simulations. Two systems reported here are a bulk fluid (with no walls) and a fluid confined between walls. Equilibrium simulations of the former are used to describe the thermodynamic and transport properties of the fluid, while the latter can tell about the structural changes induced by the walls on the fluid as well as liquid-vapour interface within the confined fluid.

The thermodynamic properties of interest from bulk fluid simulations include the isochoric $p(T)$ and isothermal $p(\rho)$ equations of state in addition to the liquid-vapour surface tension. The shear viscosity is obtained using linear response theory and provide the zero-shear (Newtonian) properties of the fluidic system.

For systems with walls, simulations of drops on a slab can show the effect of the interatomic potential on wetting. The same wall-fluid interaction parameters are used later on, in the pressure-driven flow simulations. While simulations of bubbles in a confined fluid system and simulations of liquid-vapour interfaces can provide an insight on the statics of cavitation.

3.1. Molecular model

The fluid lubricant molecules are represented by a set of randomly positioned atoms (equivalently atoms initialized with random velocity) either confined between two slabs of solid (Fig. 3.1a) or in a fully periodic system, i.e. a bulk system (Fig. 3.1b). The text below describes the constituents of the system, including the lubricant and walls, as well as the interatomic potentials used. A detailed account of a typical equilibrium simulation and post-processing procedures is also provided.

3.1.1. Materials

The lubricant used mainly in this work is the normal alkane, *n*-pentane. Alkanes are organic acyclic (aliphatic) hydrocarbons with single bonds between the carbon atoms, their general formula is C_nH_{2n+2}. For *n*-pentane, $n = 5$. In contrast to branched alkanes, normal alkanes have no side chains.

n-pentane is not a common lubricant. It is rather a component in natural gas, liquefied petroleum gas and hydrocarbon fuels that is commonly used in geothermal power plants, referigeration cycles and insulating materials [121]. Nevertheless, using *n*-pentane as the lubricating fluid in this work validates the pressure-driven flow method for molecular systems. The methods and simulations procedures followed here are ideally transferable to more complex fluidic systems.

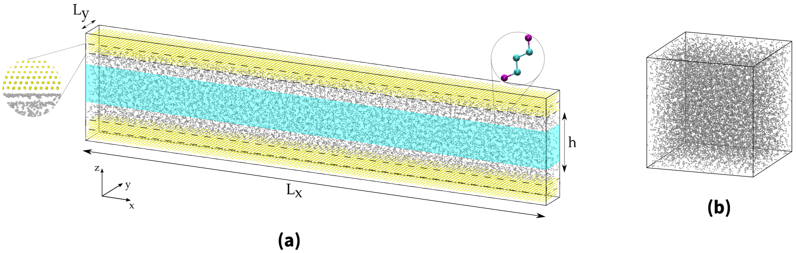

(a)

(b)

Figure 3.1.: Molecular domain of liquid lubricant molecules (in gray) **a.** confined between solid atoms (in yellow) and **b.** in a bulk system. The fluid shown here is *n*-pentane with a united-atom representation. The dashed region in the walls is the thermostated region and the cyan region defines a bulk region equidistant from the walls, where bulk fluid properites are measured.

The solid surfaces are represented by a slab geometry of two (111) surfaces of FCC gold, with a lattice constant of 4.08 Å. A primitive unit cell consists of 3 atomic layers in the *z*-direction. In the current setup, two unit cells are used in the *z*-direction to represent each wall, thus the slab thickness is the thickness of 6 atomic layers in addition to the interlayer spacings. The three outermost layers are spatially fixed mimicking rigid walls, and the three innermost layers are vibrating about their equilibrium lattice positions. To ensure that the walls were in a solid state, the temperature of the walls was kept much lower than the melting point of gold. No additional springs were used to tether the wall atoms.

	TraPPE-UA		GROMOS-54A7	
Pseudoatom	ϵ (Kcal/mol)	σ (Å)	ϵ (Kcal/mol)	σ (Å)
CH	-	-	0.0268	5.019
CH_2	0.0914	3.93	0.0981	4.070
CH_3	0.195	3.75	0.2073	3.748

Table 3.1.: The Lennard-Jones potential parameters for different pseudoatoms using TraPPE-UA and GROMOS-54A7 force fields.

3.1.2. Interatomic potentials

The short and long range interactions for the fluid were described with the TraPPE force field [44] with a united-atom (UA) representation and the GROMOS-54A7 force field [43] with UA as well as all-atom (AA) representations. For TraPPE and GROMOS potentials, geometric combining rules for both ϵ_{ij} and σ_{ij} were used such that $\epsilon_{ij} = \sqrt{\epsilon_i \epsilon_j}$ and $\sigma_{ij} = \sqrt{\sigma_i \sigma_j}$, where i and j are different atomic species.

The long range liquid-liquid, liquid-solid and solid-solid interactions are described with the Lennard-Jones (LJ) potential. The LJ potential is shifted such that the potential energy becomes zero beyond the cutoff radius. The non-bonded Lennard-Jones and bonded interatomic parameters are listed in tables 3.1 and 3.2, respectively.

The pseudoatoms in n-pentane have zero net charge. The cutoff radius r_c for the LJ potential is 14 Å, except for multiphase fluid simulations with liquid and vapour phases coexisting $r_\mathrm{c} = 24$ Å was used. Increasing r_c is required because force truncation significantly affects the interfacial properties compared to the bulk properties [67].

The LJ parameters for gold are 5.29 Å and 2.655 Kcal/mol for the Van Der Waals radius σ and the potential depth ϵ, respectively [122]. The wall-fluid interaction between the walls and each of the fluid species is evaluated according to the geometric combining rules. For cases where the fluid wettability is varied, the parameter ϵ_{ij}, where i is a solid atom and j is a fluid atom (for instance a CH_2 or CH_3 pseudoatom), is tuned with a prefactor of 0.01, 0.2 and 1 representing the non-wetting, intermediate-wetting and wetting fluids, respectively.

	TraPPE-UA			GROMOS-54A7	
Bond stretching	k_b	b_0		k_b	b_0
	1000	1.54		299.8	1.52
Angle bending	k_θ	θ_0		k_θ	θ_0
	124.2	114		55.13	109.5
	-	-		55.11	111
Dihedral torsion	k_1	k_2	k_3	k_χ	σ
	1.411	-0.271	3.145	1.415	3
Improper torsion	k_i	$\chi_{\mathrm{i}0}$		k_i	$\chi_{\mathrm{i}0}$
	-	-		40.02	35.26

Table 3.2.: Bonded interaction parameters for TraPPE-UA and GROMOS-54A7 force fields. These parameteres are used together with equations Eq. 2.1, 2.4 and 2.5 to describe the intramolecular interactions

.

3.1.3. Simulation & post-processing details

The simulation box for the bulk system (Fig. 3.1b) is periodic in all directions whereas for the confined fluid simulations, the box (Fig. 3.1a) is periodic only in the length and width. i.e. x- and y- directions.

Integration of the equations of motion was carried out with the velocity Verlet integration scheme. The time step Δt was set to 1 fs and the neighbour list was updated every time step. The choice was based on the time step that results in the minimum total energy with no drift during a microcanonical simulation of the bulk fluid. For the rigid regions in the wall, the solid-solid interactions were switched off and exlcluded from neighbour list to reduce computational cost.

The initialization of the confined fluidic system started by replicating the gold primitive unit cell to create a slab. n-pentane molecules were inserted on an equally spaced grid, between two gold slabs. The separation between the slabs determines the gap height. For bulk systems, only n-pentane molecules were inserted in the box. The number of molecules N and the fluid density ρ were specified and the box size was adjusted accordingly.

To generate a fluid configuration, the atoms were given a velocity drawn from a Gaussian distribution. In calculations that involve walls, only the innermost layers of the upper and lower walls, in contact with the fluid, were thermostated with the Langevin thermostat while the outermost layers as well as the fluid atoms were thermostat-free i.e. sampled the NVE ensemble. The damping constant for the Langevin and Berendsen thermostats is 100 fs. For simulations in the NPT ensemble, Nosé-Hoover barostat and thermostat were used. The barostat damping constant is 1000 fs.

In bulk liquid simulations (Sec. 3.2 and Sec. 3.3), the thermodynamic quantities were summed over all atoms and averaged over time. In liquid-vapour coexistence simulations (Sec. 3.4), the simulation box was decomposed into 144 spatial bins along the z-direction to compute the variation in density (see Fig. 3.4). To compute the structure factor for the confined fluid (Sec. 3.5), the reciprocal space was decomposed into 200 and 16 discrete wave vectors in the longitudinal x- and transverse y- directions, respectively. Finally, to compute the thermodynamic bulk properties of the confined fluid (Sec. 3.6), the fluid density and virial pressure were measured only in the bulk region, the cyan region in Fig. 3.1a.

3.2. Equation of state

The equation of state (EoS) describes the relationship between the macroscopic variables such as pressure, volume and temperature, and allows the prediction of the thermodynamic state of the system under certain conditions. In the context of this thesis, the ischoric EoS describes the pressure-temperature relation $p(T)$ and was obtained to compare different force fields in addition to different molecular representations. The isobaric EoS describes the pressure-density relation $p(\rho)$ and was necessary for estimating the bulk density changes under loading, which is a crucial step before conducting the NEMD simulations. Additionally, the isobaric EoS define the material pressure-density relation needed for the continuum calculations in Ch. 5.

The isochoric EoS was obtained from equilibrium simulations in the canonical (NVT) ensemble using the GROMOS-54A7-UA and TraPPE-UA force fields. Additionally, the GROMOS-54A7-AA force field is presented for comparing AA and UA representations of n-pentane. The simulation box consisted of 60 molecules i.e. 300 pseudoatoms and 1020 atoms with UA and AA representations, respectively. The fluid density was fixed at $0.673\,\mathrm{g/cm^3}$ which corresponds to a box of size $22 \times 22 \times 22\,\mathrm{\AA}^3$.

The simulation proceeded by a first equilibration for 0.01 ns using the Berendsen thermostat followed by a production equilibration with the Nosé-Hoover thermostat for 1 ns. The initial equilibration is done with the Berendsen thermostat since it is very efficient at relaxing the fluid rapidly to the target temperature. The pressure values within the first equilibration period are discarded from the time-average. The results, shown in Fig. 3.2a, indicate that a UA representation can provide accurate predictions of the thermodynamic properties. Explicit inclusion of the hydrogen atoms does not improve the results significantly at least in the range of temperatures and pressures presented here.

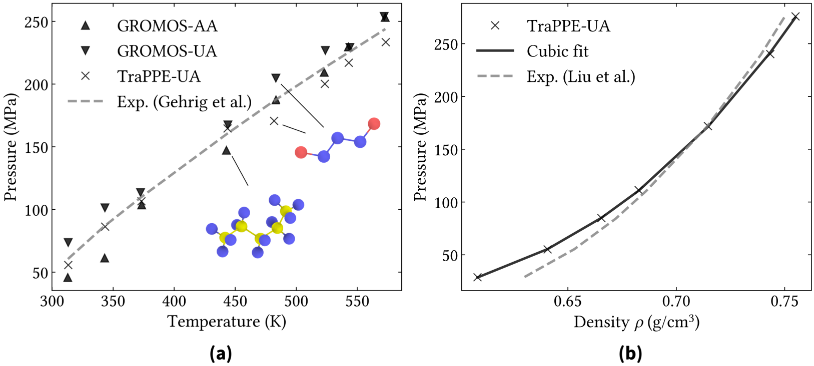

Figure 3.2.: Equations of state for *n*-pentane: **a.** Isochoric EoS using UA and AA GROMOS-54A7 [43] in addition to TraPPE-UA [44] force fields with experimental values from Ref. [123]. **b.** Isothermal EoS using TraPPE-UA force field with experimental values from Ref. [124]

The isothermal EoS was obtained from simulations in the isothermal-isobaric (NPT) ensemble using only the TraPPE-UA force field which is the main force field used throughout this thesis. 2880 *n*-pentane molecules were initialized and equilibrated at 300 K.

The initial equilibration lasted for 0.06 ns with only the Berendsen thermostat activated, followed by a production equilibration for 2 ns with the Nosé-Hoover thermostat and barostat. From Fig. 3.2b, TraPPE-UA prediction of the fluid density agrees with experimental values. The coefficients for the cubic EoS: C_1, C_2, C_3 and C_4 are 12.36 Pa/(kg/m^3)^3, -1.74 $\times$ 10^4 Pa/(kg/m^3)^3, 8.04 $\times$ 10^6 Pa/(kg/m^3) and -1.22×10^9 Pa, respectively.

3.3. Shear viscosity

Computing the shear viscosity from equilibrium simulations provides the zero-shear (Newtonian) viscosity value. The simulation setup and post-processing analysis performed here, to obtain the shear viscosity from the Green-Kubo relation, adhere to the guidelines reported by Maginn et al. [125].

Briefly, the workflow followed is a sequence of simulations in the NPT ensemble followed by switching off the barostat i.e. performing NVT equilibration and finally the thermostat is switched off, thus the production equilibration is in the NVE ensemble. The length of each equilibration step was 1.1 ns. In the final step (NVE simulation), temperature and pressure fluctuated around the mean values set from the initial NPT simulation. Measurement of the viscosity directly in the NPT ensemble was avoided since barostats and thermostats interfer with the system dynamics. In this study, the fluid box consisted of 2800 molecules.

A total of 10 replicates of the system were generated before the first NPT equilibriation step. A replicate is defined by the random number seed used for velocity initialization. The bootstrapping technique mentioned in Ref. [125] was employed, to obtain the uncertainty of the computed viscosity at a 95% confidence interval.

For each replicate, a running integral over the correlation time t was performed for the autocorrelation function to get the viscosity from Eq.(2.27). This is shown in Fig. 3.3a. To improve the precision, the auto correlation function was averaged over multiple time origins within t. The final viscosity was obtained from the time-average within the first plateau region, 0.01 to 0.04 ns in Fig. 3.3a.

To validate the Green-Kubo calculations, the viscosity was measured at different pressures at 303 K and compared with experimental values from Ref.[126], see Fig. 3.3b. The TraPPE-UA under predicts the viscosity by $10 - 30\%$ [127]. Therefore, to enable comparison, the presented results were normalized with the respective maximum shear viscosity η_0. The disparity between experimental and MD simulations presents a caveat when interpreting transport properties using the TraPPE-UA force field.

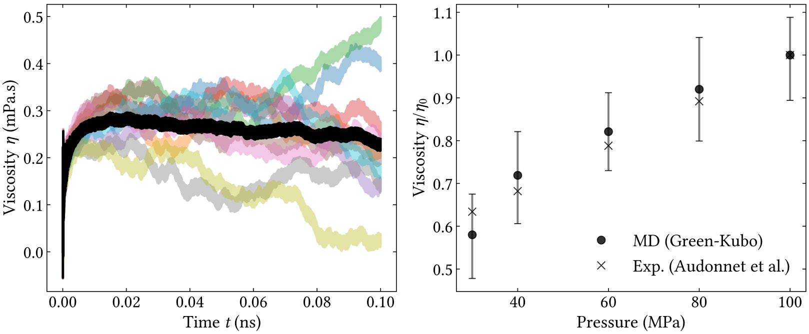

(a) **(b)**

Figure 3.3.: The shear viscosity of n-pentane from equilibrium simulations using the Green-Kubo relation (Eq. (2.27)). In **a.** the viscosity computed at (303 K, 100 MPa) for 10 replicates and their average (black) are plotted against the correlation time t. **b.** The change of viscosity with pressure at 303 K from equilibrium simulations (normalized by the η_0 measured at 100 MPa) and from experiments Ref.[126].

3.4. Surface tension

Quantifying the liquid-vapour interface properties in equilibrium provides an estimation of the surface tension γ in addition to the density and pressure of each of the coexisting phases. The values obtained here can be further used in comparing the dynamics of vapour bubbles acquired from NEMD simulations of cavitation to the hydrodynamic theory.

The approach to compute the liquid-vapour surface tension proceeds by creating a simulation box elongated in the z-direction with three regions of equal thickness, as shown in Fig. 3.4. The middle region comprises 2800 molecules in the liquid (high density) phase sandwiched between two regions of 150 randomly positioned molecules in the vapour (low density) phase.

Finite size effects, force truncation effects and long-range corrections to the potential have to be handled carefully. A guide to understanding the effect of these parameters on the measured γ can be found in Ref. [67]. In this study, the cutoff radius r_c used was 24 Å with no long-range corrections.

First equilibration, for 0.01 ns, of the enitre system was performed by running the dynamics in the canonical ensemble using the Berendsen thermostat. A second equilibration, for 3 ns, was then performed by switching to the Nosé-Hoover thermostat. The first 1 ns was discarded from the time-averged density and virial stress components calculation.

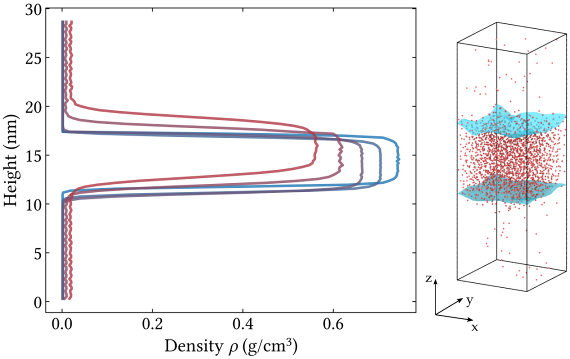

Figure 3.4.: Liquid-vapour coexistence simulations to obtain the planar surface tension. The interface (cyan surface) of liquid (slab in the box center) and vapour (scattered around the liquid) at equilibrium. The density profile was time-averaged along the simulation box z-direction. The color grading from blue to red indicate increasing temperature.

The interface surface (cyan) in Fig. 3.4, remained stable after the initial equilibration and throughout the simulation time. This indicates that both phases were stable and coexisted at the range of temperatures examined. By changing the temperature of the liquid-vapour system, the coexistence curve, Fig. 3.5a can be extracted.

The system density, Fig. 3.4, is inhomogeneous as the box segregates into a liquid slab confined between regions of gas. As the temperature increases up to the critical point (the red point on the coexistence curve in Fig. 3.5a), the density of the liquid phase drops while the vapour phase density increases. At the critical point and beyond, the multiphase system homogenizes to form a single phase.

The calculated coexistence curve, Fig. 3.5a, shows agreement with experimental data [128] and Monte Carlo simulations [44]. The critical properties can be extrapolated from weighted linear fits to the subcritical data. The critical temperature T_c is obtained from the density scaling law

$$\rho_l - \rho_v = a(T - T_c)^\beta \tag{3.1}$$

while the critical density ρ_c was obtained from the law of rectilinear diameters

$$1/2(\rho_l + \rho_v) = \rho_c + b(T - T_c) \tag{3.2}$$

where a and b are fitting coefficients. ρ_l and ρ_v are the liquid and vapour densities while $\beta = 0.32$ is the critical exponent [44], a universal quantity that describes physical behavior near phase transition. The critical point from MD simulations is at $\rho_c, T_c = (0.241\,\mathrm{g/cm^3}, 464.4\,\mathrm{K})$ and from experiments [128] at $\rho_c, T_c = (0.232\,\mathrm{g/cm^3}, 469.70\,\mathrm{K})$. In conclusion, the TraPPE-UA shows excellent performance in the liquid-vapour coexistence simulations. This is not surprising since TraPPE was originally developed for phase equilibria by fitting to saturation curves of *n*-alkanes.

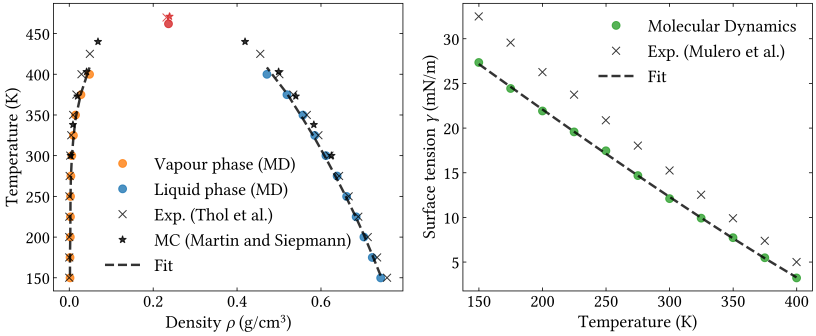

(a) **(b)**

Figure 3.5.: Liquid-vapour **a.** coexistence curve of *n*-pentane obtained from molecular dynamics calculations compared to experiments from Ref. [128] and Monte Carlo simulations from Ref. [44], and **b.** surface tension change with temperature compared to experiments from Ref. [129]. The red markers in **a.** represent the critical point.

The surface tension as a function of temperature is shown in Fig. 3.5b. There is an underestimation of the surface tension from molecular dynamics calculations as compared to experimental values. The surface tension can be described with the function form [130],

$$\gamma = \gamma_0(1 - T/T_c)^d \tag{3.3}$$

where γ_0, T_c and d are fitting coefficients. T_c was determined to be 444 K. Therefore, the two figures in Fig. 3.5 present two different ways to compute T_c. According to the results reported here, the coexistence curve provides a more precise estimate.

The surface tension computed here is the planar surface tension γ_∞. For including curvature effects of a bubble (or similarly a drop), the surface tension needs to be corrected with a prefactor. This will be discussed further in the last section of this chapter.

3.5. Surface wetting & layering

The wall-fluid interaction strength can be tuned to determine the degree of hydrophobicity of the surface (or wettability of the fluid). The confined fluid's wettability plays a major role in the total flow mass flux and velocity slip along the walls.

To demonstrate the sensitivity of wetting to the wall-fluid interaction strength, simulations of a drop of 860 n-pentane molecules on gold (111) surface, consisted of 34450 atoms, were performed. The LJ potential depth ϵ_{ij} between the fluid and the solid was changed as mentioned in Sec. 3.1.2. The effect of changing ϵ_{ij} on the potential energy and the resulting drops are shown in Fig. 3.6. The Berendsen thermostat was applied on the fluid for the first equilibration for 0.2 ns and for the remaining 6 ns, the thermostat was switched off and the fluid atoms trajectories sampled the NVE ensemble.

The contact angle can be obtained directly from a simulation of a droplet on the surface, Fig. 3.6. Although θ is a macroscopic quantity which is difficult to accurately measure at the nanoscale [105], attempts to calculate θ usually involve cylindrical binning to find the equimolar dividing surface, followed by fitting to a circle and extrapolating the fit to the surface [131, 132].

For a wetting fluid confined between solid walls, the fluid atoms in the vicinity of the walls exhibit large attraction energy to the walls and inherit structural order from the surface. Fluid ordering or epitaxial locking [13] imprint is evident in modulations in the fluid's density and velocity profiles along the gap height. This will be shown in detail in the next chapter.

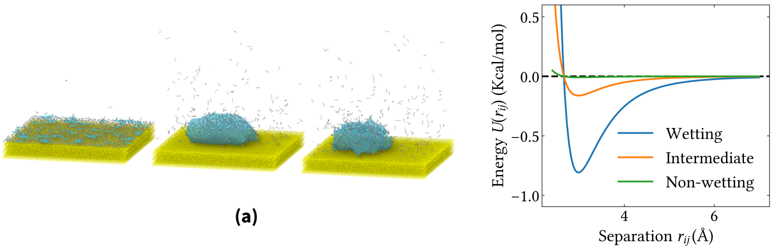

(a)

(b)

Figure 3.6.: Fluid wettability tuned through the surface-fluid interaction energy. **a.** Left to right: Wetting, intermediate-wetting and non-wetting fluid on a solid surface. **b.** The corresponding LJ interatomic potential of the fluid-wall interaction.

Fluid ordering can be quantified through the structure factor $S(\vec{k})$ (Eq. (2.29)). Equilibrium simulations of the fluid confined between two surfaces, Fig. 3.1a, were performed and $S(\vec{k})$ was computed in the fluid within the boundary layer only. As a benchmark, $S(\vec{k})$ was also measured in the solid boundary layer (Fig. 3.7b). The 2-dimensional structure factor, along the longitudinal and transverse wave vectors, for the wetting and non-wetting fluids is shown in Fig. 3.7c and Fig. 3.7d, respectively.

The degree of surface induced ordering increases as the fluid-wall interaction becomes stronger. The boundary layer of a wetting fluid is highly ordered as shown in the snapshot in Fig. 3.7a. The locked layer could be thought of as a solid phase wetting the walls [13] as the fluid atoms tend to position themselves within the hollow sites of gold atoms surface [74]. Therefore, the spacing between the ordered fluid layer molecules is dependent on the lattice constant of the solid.

The sharp Bragg peaks in Fig. 3.7b to 3.7d are similar to those observed in neutron or X-ray scattering experiments [13]. The peak in the solid structure factor, Fig.3.7b, corresponds to the first reciprocal lattice vector $k_y = 2.10\text{Å}^{-1}$. In real lattice, using $\vec{k} = 2\pi/\vec{r}$, where $\vec{r} = (x, y)$, therefore $y = 3\text{Å}$, which is close to 2.85Å, the distance to the nearest neighbour along the y direction in the (111) FCC gold surface. The amplitude of the peak gets progressively smaller for larger vectors until the peak fades out. Note that the peak at $\vec{k} = (0, 0)$ was omitted for visualization purposes.

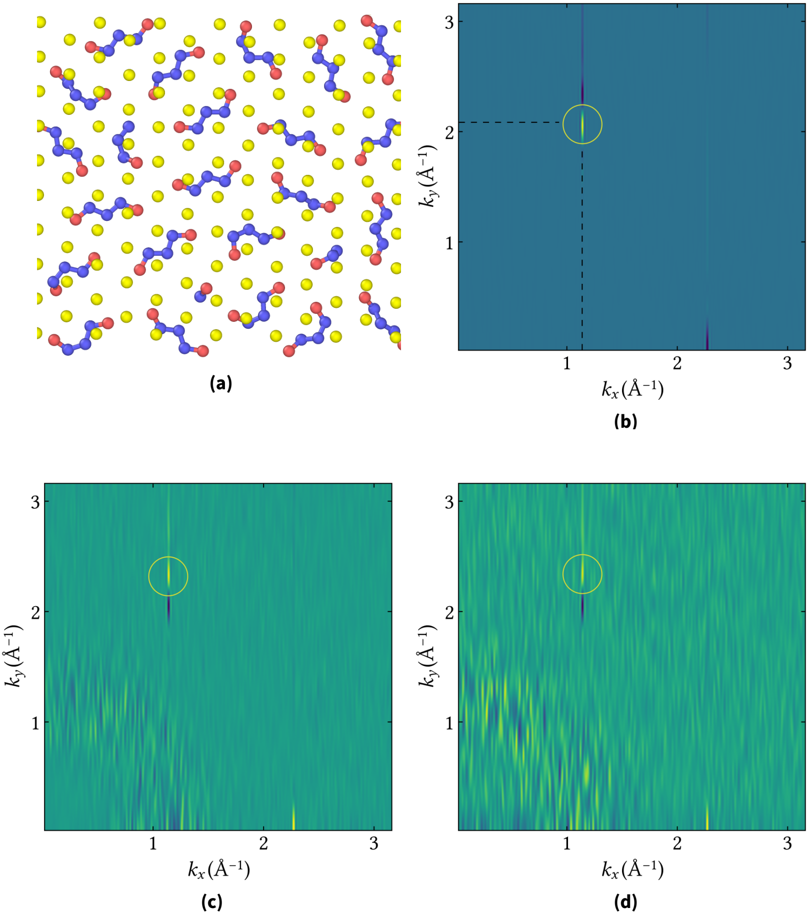

(a)

(b)

(c)

(d)

Figure 3.7.: **a.** Epitaxial locking of the fluid boundary layer atoms (in blue and red) to the solid wall (in yellow). Atomic ordering is quantified through the structure factor $S(\vec{k})$. $S(\vec{k})$ was measured at the boundary layer of the **b.** solid, **c.** wetting fluid and **d.** non-wetting fluid. Note that that $(k_x, k_y) = (0, 0)$ is not shown here. The peaks are highlighted with yellow circles for visualization.

The structure factor computed for the wetting and non-wetting fluids, Fig. 3.7c and Fig. 3.7d, show slighlty shifted peak positions from that of the solid. This confirms that the fluid atoms are sitting in the hollow sites of the solid ordered lattice and that the solid induces order on the wetting as well as the non-wetting fluids.

For the non-wetting fluid (Fig. 3.7d), there is broader distribution within $S(\vec{k})$. This suggests that there is still order in the non-wetting fluid near the walls. The circular ridge at $|\vec{k}| = 2\pi/\sigma$ persists from the short-range fluid ordering. In the bulk of the wetting and non-wetting fluids, $S(\vec{k})$ gets smeared out and shows no peak. Hence, far from the walls, the fluid retains its disorder.

3.6. Bubble radius

The aim of this section is to quantify the radius of a vapour bubble, at equilibrium with the liquid, by performing simulations of a non-planar liquid-vapour interface. Before characterizing the cavitation size and dynamics in a hydrodynamic flow (NEMD) setup, comparing static conditions of the cavity with the Young-Laplace equation can act as a reference point.

The confined fluid setup was used, Fig.3.1a. The density of the fluid was reduced to a fraction of the saturation density ($\rho_{\text{sat}} = 0.62\,\text{g/cm}^3$) at 300 K in order to ensure the coexistence of liquid and vapour phases (see Fig. 3.5a). The simulation box aspect ratio $L_y/L_x = 0.72$ was used. The initial equilibration was performed by applying a Berendsen thermostat on the fluid for 0.06 ns. For the remaining 2 ns, the fluid atoms sampled the microcanonical ensemble. The vibrating portion of the walls was thermostated with Langevin thermostat for the whole simulation time. The volume of the box was also kept constant.

Sampling of thermodynamic properties, bulk density and virial pressure, started only in the last 1 ns. For visualizing the fingerprint of the bubble, the spatial binning was performed along the length L_x and the width L_y dimensions. Averaging was performed along time (from the sampling point) and height (only the fluid bulk). The radius was measured measured every 0.01 ns from the beginning of the simulation.

A spherical cavity nucleated, expanded but remained immobile in the channel, similar to the planar liquid-vapour interface simulations. This allowed a domain decomposition into liquid and vapour regions, as shown in Fig. 3.8d. To get the radius from the Young-Laplace equation (Eq. (2.48)), p_{v}, p_{l} and γ are

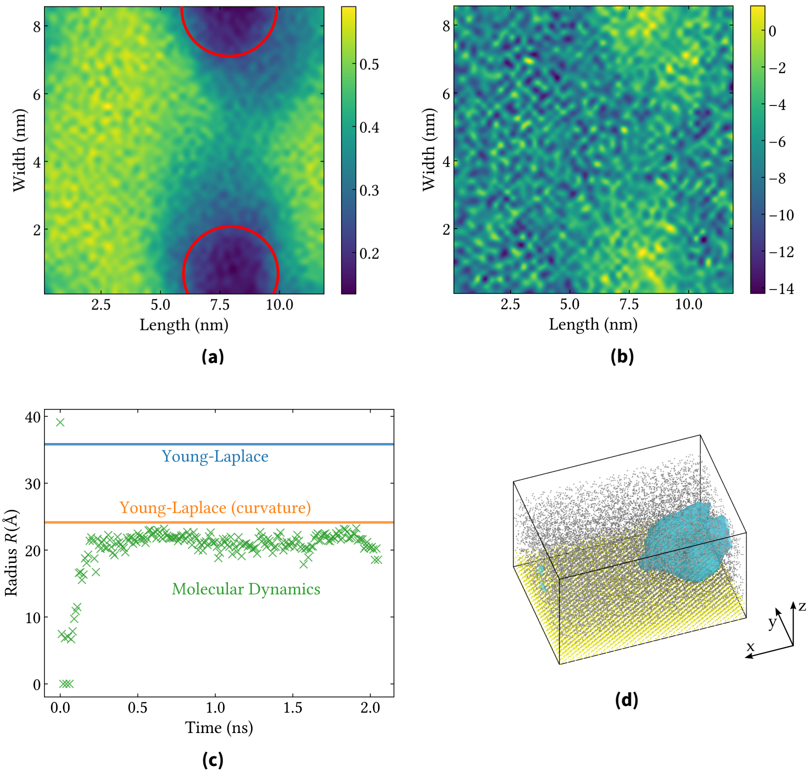

Figure 3.8.: Spherical vapour bubble **a.** density map (red lines define the bubble contour), **b.** virial pressure map, **c.** radius along time and **d.** in the simulation box (the upper wall has been discarded for visualization purposes). The Cyan surface in **d.** is the surface mesh of the cavity from the α-shape algorithm [120].

required. At 300 K, the vapour pressure p_v for n-pentane is 73 KPa [133] and the planar surface tension, obtained from Sec. 3.4, is $\gamma_\infty = 12.5$ mN/m. The liquid pressure p_∞ was measured in the liquid region away from the cavity. More specifically, it was measured within $L_x = 2.5 \longrightarrow 5$ nm and $L_y = 3 \longrightarrow 5$ nm in Fig. 3.8b. The pressure in the liquid is negative, which is reasonable because according to the Young-Laplace equation, $p_\mathrm{v} - p_\infty$ has to be positive since γ and R are always positive.

The Young-Laplace equation overestimates the bubble radius. Eq. (2.47a) was used to correct for the surface curvature. The Tolman length δ_T was assumed to be the molecular diameter (5.02Å), as reported in Ref.[103]. Whether δ_T should be negative or positive is still an unsolved issue [67]. Results from density functional theory and other MD simulatons reported negative values [134] while in other cases [135], it was reported positive. The correction computed here can be used in the context of hydrodynamic cavitation.

The bubble nucleation site depends on the surface wettability. A homogeneous nucelation took place with hydrophophillic surfaces while heterogenous nucleation occured for hydrophobic walls. For hydrophobic walls, there was no distinct bubble rather a thicker depletion gas layer between the fluid and the solid.

4. Pressure-driven flow

4.1. The Pump method

The method utilises the Reynolds tansport theorem introduced in App. A by applying a perturbation along the stream-wise direction (x-direction) only within the control volume, the “pump”. The perturbation can be in the form of either a force or a mass flux, applied at each time step.

First, the continuum formulation is translated to the molecular domain. A detailed description of the implementation of the pump method in molecular simulations, to generate pressure-driven flow, is provided. Subsequently, a compilation of results from applying the method is presented.

4.1.1. Fixed Force

The net x-component force within the pump can be derived from Eq. A.8, where the external force is the pump force,

$$F_{\text{pump}} = \int \left[\frac{\partial p}{\partial x} - \frac{\partial \tau_{xx}}{\partial x} - \frac{\partial \tau_{xy}}{\partial y} - \frac{\partial \tau_{xz}}{\partial z} \right] \mathrm{d}V + \int_{\text{out}} \rho u^2 \, \mathrm{d}y \, \mathrm{d}z - \int_{\text{in}} \rho u^2 \, \mathrm{d}y \, \mathrm{d}z \tag{4.1}$$

where the volume integral describes the balance of the x-component forces within the pump volume V and the second and third terms are the momentum flux outflow and inflow from the pump surfaces in the x-direction (see Fig. 4.1a). ρ and u are the fluid density and x-component of the velocity, respectively.

The sum of x-forces within the pump can be written as,

$$\begin{aligned} F_{\text{pump}} = &\int_{\text{out}} (p - \tau_{xx})\, \mathrm{d}y\, \mathrm{d}z - \int_{\text{in}} (p - \tau_{xx})\, \mathrm{d}y\, \mathrm{d}z - \int_{\text{front}} \tau_{xy}\, \mathrm{d}x\, \mathrm{d}z \\ &+ \int_{\text{back}} \tau_{xy}\, \mathrm{d}x\, \mathrm{d}z - \int_{\text{top}} \tau_{xz}\, \mathrm{d}x\, \mathrm{d}y + \int_{\text{bottom}} \tau_{xz}\, \mathrm{d}x\, \mathrm{d}y \\ &+ \int_{\text{out}} \rho u^2\, \mathrm{d}y\, \mathrm{d}z - \int_{\text{in}} \rho u^2\, \mathrm{d}y\, \mathrm{d}z \end{aligned} \tag{4.2}$$

The integral domains are shown in Fig. 4.1a. The walls are in the xy plane and the flow is in the yz plane. The stress components τ_{xy}, acting on the front and back faces (colored green in Fig. 4.1a) in the third orthogonal (xz) plane, are considered insignificant and thus omitted from the analysis. Additionally, only the hydrostatic part of the stress tensor is considered in the flow direction i.e. $\tau_{xx} = 0$. If we denote the cross-sectional area perpendicular to the flow and the area along the flow parallel to the walls as $A_{\perp}$ and $A_{||}$, respectively, then Eq. (4.1) can be rewritten as,

$$F_{\text{pump}} = \Delta p A_{\perp} - \Delta \tau_{xz} A_{||} + \int_{\text{out}} \rho u^2\, \mathrm{d}A_{\perp} - \int_{\text{in}} \rho u^2\, \mathrm{d}A_{\perp} \tag{4.3}$$

where Δ here refers to the difference between two opposite faces. Finally, the applied pump force is expressed as

$$F_{\text{pump}} = F_{\text{p}} + F_{\text{wall}} + \int_{\text{out}} \rho u^2\, \mathrm{d}A_{\perp} - \int_{\text{in}} \rho u^2\, \mathrm{d}A_{\perp} \tag{4.4}$$

where F_{p} and F_{wall} are the pressure-difference force and the fluid-wall friction force, respectively. The integral terms represent the net momentum flux. A schematic of the final force representation within the pump in the molecular RVE is shown in Fig. 4.1b.

The pressure-difference force results from the pump inlet-outlet pressure difference. Δp is then the independent variable to control the pressure gradient. If the pump is applied in a region with a non-uniform cross-section, i.e. inclined walls, the pressure difference force can be written as $p_{\text{out}} A_{\text{out}} - p_{\text{in}} A_{\text{in}}$.

The friction force is that imposed on the flowing fluid from the walls, it is obtained by summing over the x-component of the fluid-wall pairwise

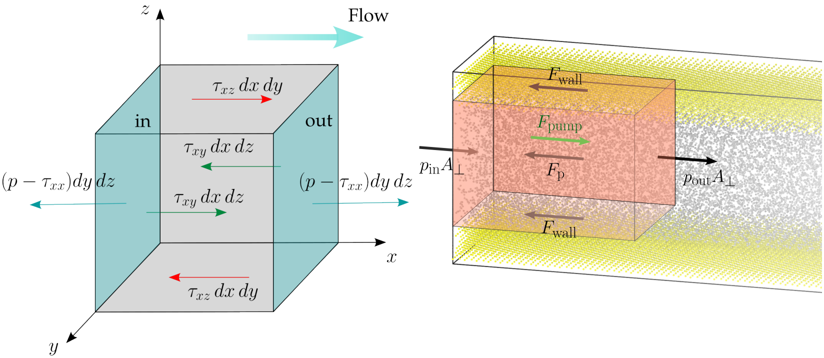

(a)

(b)

Figure 4.1.: A schematic of linear momentum balance in the pump shown on **a.** control volume element and on **b.** a molecular representative volume element. In **b.**, the prepressure-difference force F_{p} and the friction force F_{wall} act opposite to the final applied pump force F_{pump} (highlighted in green). In this schematic $p_{\text{out}} > p_{\text{in}}$.

forces in the pump region. Force decomposition is possible if the wall-fluid interaction is described with a pairwise potential

$$F_{\text{wall}} = -\tau_{xz}A_{||} = -\sum_{i}^{\text{fluid}}\sum_{k}^{\text{wall}} f_{ik,x} \tag{4.5}$$

where $f_{ik,x}$ is the x-component of the force imposed by atom k from the walls on atom i from the fluid.

The net momentum flux in the pump can be computed in upstream and downstream regions relative to the pump. Both regions are of equal length and are much smaller than the pump itself. Within both regions, the total densities ρ, velocities u and the corresponding forces are computed as a moving time-average of the last n timesteps and imposed on the $n+1$ step. The resulting net force is only added to F_{p} and F_{wall} after some stabilization time. Liang and Tsai [62] showed that for an incompressible flow, where the density (or velocity) does not change significantly along the stream-wise direction, i.e. these forces have minor contribution to the total pump force.

In a NEMD simulation, the force on an atom i in the pump, is the sum of the gradient of the interaction potential U with neighboring atoms and the external force. Without considering thermostatng, the x-compnent of the equation of motion of a fluid atom in the pump can thus be written as,

$$m_i \ddot{x}_i = -\frac{\partial U}{\partial x} + \frac{F_{\text{pump}}}{N_{\text{pump}}} \tag{4.6}$$

where F_{pump} is averaged over the number of fluid atoms in the pump region, N_{pump}. Outside the pump, in the pressure-driven region, the fluid atoms undergo free dynamics i.e. $F_{\text{pump}} = 0$.

4.1.2. Fixed Current

A similar approach of applying a perturbation to achieve a pressure gradient can be implemented through controlling the mass flux rather than the forces. The mass flux can be set as a constraint through fixing an acceleration (or current) applied to all atoms in the pump.

The x-component of the linear momentum conservation equation for a fluid under a fixed x-direction acceleration a_{pump}, can be written as

$$\rho\, a_{\text{pump}} = \frac{\partial p}{\partial x} - \frac{\partial \tau_{xx}}{\partial x} - \frac{\partial \tau_{xy}}{\partial y} - \frac{\partial \tau_{xz}}{\partial z} + \frac{1}{V}\left[\int_{\text{out}} \rho u^2 \, \mathrm{d}A_\perp - \int_{\text{in}} \rho u^2 \, \mathrm{d}A_\perp \right] \tag{4.7}$$

Therefore, the applied acceleration in the pump would result in a pressure gradient. In a simulation, the acceleration a_{pump} is applied only on atoms in the pump in the form of an x-component center of mass velocity, which is added to the atomic velocities before the second half integration of the Verlet time step.

Similar to the pressure difference Δp being the boundary condition in the FF variant, the x-direction mass flux j_x (or x-direction mass flow rate $\dot{m}_x$) is the boundary condition in the FC variant. The mass flux j_x and flow rate $\dot{m}_x$ are related to u_{COM} through

$$u_{\text{COM}} = \frac{j_x \, A_\perp \, L}{\sum_i m_i} = \frac{\dot{m}_x \, L}{\sum_i m_i} \tag{4.8}$$

where the relation $j_x = \rho u$ was used. The quantities L and $\sum_i m_i$ represent the length of the pump region and the sum of atomic masses in the pump. During the NEMD simulation, the gap height fluctuates, therefore, u_{COM} changes with the gap height, which is encoded in $A_\perp$. To fix u_{COM}, the mass flow rate, rather than the mass flux, is preferred as the boundary condition.

The pump formulation, Eq. (4.4) and Eq. (4.8), show how the macroscopic momentum balance can be used to apply atomic scale perturbation to achieve pressure gradients in nanofluidic domains. The mass flow rate $\dot{m}_x$ measured from an FF simulation and imposed as a boundary condition in an FC simulation shall result in the same pressure gradient. Similarly, for a pressure difference Δp measured in an FC simulation. This is due to the macroscopic force-flux duality which is persistent on the nanoscale.

4.2. Molecular model

The aim from the set of simulations in this chapter is to test the pump method and to understand and quantify the thermodynamic and transport changes of the nanoconfined fluid. Therefore, it is reasonable to start from a set of fluid molecules representing the liquid lubricant confined between two flat solid surfaces (slab geometry), as shown in Fig. 4.2.

As in the previous chapter, the lubricant used for testing the pump method is the straight-chain (normal) *n*-pentane confined between two FCC gold (111) surfaces. For *n*-pentane, the cutoff radius for the LJ potential was reduced from 14 to 10Å to minimize the force computation burden of large neighbour lists. The LJ potential is shifted as mentioned in Sec. 3.1.2. The intra and inter species interactions are treated as previously for fluids and walls with different wetting conditions.

4.2.1. Simulation & post-processing details

The simulation box, Fig.4.2, is periodic in the stream-wise x and span-wise y directions. The domain is partitioned into regions of applied perturbation (pump region), measurement of bulk properties away from the walls (bulk region) and measurement of properties away from the pump (sampling region). The pump region is defined a priori to the NEMD simulation and it spans the whole gap height and a portion of the box length in the stream-wise direction. The bulk and sampling regions are defined in the post-processing step.

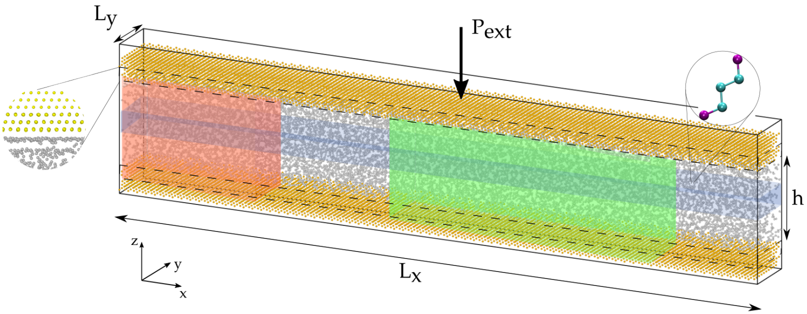

Figure 4.2.: Molecular domain of liquid lubricant molecules (in gray) confined between solid atoms (in orange). The pump, bulk and sampling regions are highlighted in red, blue and green, respectively. The fluid shown here is *n*-pentane within a united-atom representation. The dashed region in the walls is the thermostated region.

The bulk region spans the whole box length and is equidistant from the walls, i.e. centered in the gap height, while the sampling region is equidistant from the pump. The thermodynamic properties measured in the bulk region are the virial pressure and the fluid bulk density. The velocity profiles and mass flow rate are measured in the sampling region. The total fluid density and temperature are measured in the whole fluid region. For measurement of stresses in the wall, only the solid atoms in the rigid (outermost) portion of the wall were considered. Integration of the equations of motion was carried out with the velocity Verlet integration scheme.

To prepare the system for the NEMD simulation, two pre-simulations are required: a canonical (NVT) equilibration to control the fluid/wall temperature followed by equilibration in the NAP$_z$T ensemble, where A and P_z are the box (slab) surface area and external pressure in the z-direction. The second step involves loading the upper wall with a uniform force to control the hydrostatic external pressure p_{ext} on the system at a certain temperature.

In the first equilibration step, the Berendsen thermostat was applied on the fluid for the first 0.06 ns and then switched off for the remaining 2 ns to sample the microcanonical (NVE) ensmeble. For the solid, the innermost layers of the wall were thermostated with a Langevin thermostat for the whole equilibration period, 2.06 ns. The thermostating strategy was based on thermostating only the walls for reasons that will be justified in Sec. 4.3.4 and App. B. The damping constant γ (Eq. (2.31) and Eq. (2.32)) for the Langevin and Berendsen thermostats was 100 fs and the target temperature was set to 300 K.

Starting from the NVT-equilibrated configuration, an external load of magnitude $p_{\text{ext}} L_x L_y$ was imposed uniformly only on the rigid portion of the upper wall to control the pressure. The number of atoms and temperature were kept fixed hence, NAp_{ext}T statistical ensemble. The pressure coupling algorithm used here is that reported by Pastewka et al. [136]. To mimic the inertial and elastic bulk response to an external pressure, the top rigid layer movement was described by a damped harmonic oscillator with a spring constant $k = 0.01$ kcal/mol.Å^2 and a dissipation constant of value $\sqrt{2Mk}$, where M is the mass of the imaginary damper. The loading lasted for 3 ns to ensure convergence to the desired pressure (or equivalently density). The external load p_{ext} was set to 250 MPa.

The final loaded configuration served as the starting point for the NEMD simulation of lubricant flow. To induce the flow of the lubricant, the fluid atoms were driven by a pressure gradient through the activation of the pump. The pump length used here was $0.2\,L_x$. The thermodynamic quantities were sampled during the post-processing step. The initial 5 ns of the NEMD simulation were discarded from time-averaging to ensure that the system reached a steady state following the perturbation. The production simulation lasted for 35 ns.

Post-processing of the simulation data ivolved projecting the molecular trajectory onto a spatial grid of fixed size. The bin size is dependent on the simulation box dimensions and, unless otherwise stated, was set to 144 bins in the x- and z- directions. Due to large statistical errors, the first and last bins in the x-direction as well as the first and last 2 bins in the z-direction were excluded from the analysis.

4.3. Results

4.3.1. Force-Flux equivalence

The fluid is under a perturbation from the constraint applied in the pump region in the stream-wise direction, and is undergoing free-dynamics in the pressure-driven region (outside the pump). This results in an increasing (adverse pressure gradient) within the pump and a declining (favourable pressure gradient) as the fluid leaves the pump. This pressure gradient drives the fluid flow. The variation in pressure along the box length can be seen in Fig. 4.3a.

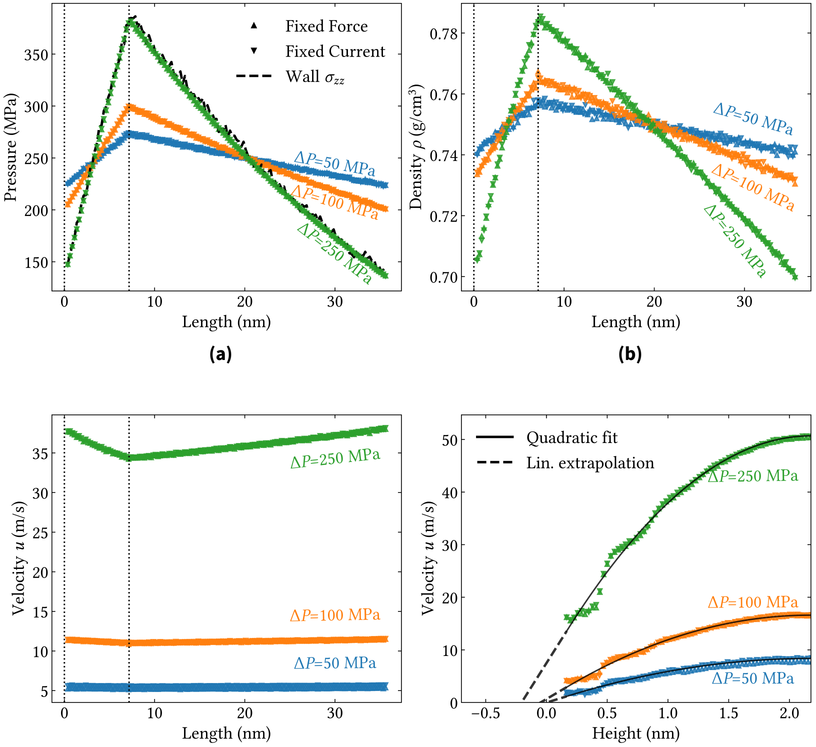

(a) **(b)**

(c) **(d)**

Figure 4.3.: Variation of **a.** pressure **b.** density and **c.** velocity x-component along the stream-wise direction and **d.** velocity x-component along the gap height (only half the gap height is shown due to symmetry around the channel centerline) using FF and FC variants of the pump method. The vertical dotted lines in **a.** to **c.** mark the pump region bounds.

Fixing the force yields the same pressure profile as fixing the current. This demonstrates the force-flux duality on the nanoscale, as well as establishes the method's flexibilty to accommodate either a pressure difference or a mass flux as the independent variable.

The fluid pressure measured in the bulk was calculated according to the virial expression Eq. (2.18) and is equivalent to the mechanical stress tensor component σ_{zz} measured at the walls from Eq. (2.19), as seen in Fig. 4.3a for the $\Delta p = 250$ MPa simulation. The viscous components of the virial stress tensor $\sigma_{\text{virial},xz}$ and the wall $\sigma_{\text{mech},xz}$ are also equal (not shown here).

The density variation along the stream (Fig. 4.3b) shows that the fluid is under compression in the pump. Nevertheless, the fluid can be considered to be incompressible as the variation in density is ≤10%. As the pressure reaches its maximum value at the pump outlet, so does the x-component of the velocity reach its lowest value (Fig. 4.3c).

The velocity profiles along the gap height, in Fig. 4.3d, agree with the hydrodynamic solution Eq. (2.6). These profiles can be fit to a quadratic function, and a linear extrapolation to the fitting curve can be used to evaluate the slip length b (and velocity u_{slip}). It is observed from the figure that at $\Delta p \leq 100$ MPa, the fluid can be considered not slipping against the walls compared to the case of Δp of 250 MPa, where slip becomes more significant. At $\Delta p = 250$ MPa, the slip velocity u_{slip} and slip length b are $\sim$ 12 m/s and $\sim$ 0.2 nm, respectively.

4.3.2. Compressible flow

As the applied perturbation gets larger, the incompressibility assumption becomes less valid. At $\Delta p = 500$ MPa, the fluid density and velocity change significantly (~ 25%) along the stream, as shown in Fig.4.4a. The flow remains laminar as Reynolds number is 1.33.

It is evident from Fig. 4.4a that $\frac{\partial u}{\partial x}$ and $\frac{\partial \rho}{\partial x}$ are $\neq 0$. From the continuity equation at steady state, the one-dimensional mass balance becomes $\rho \frac{\partial u}{\partial x} = u \frac{\partial \rho}{\partial x}$, which is also valid in MD. The velocity profiles measured in four regions outside the pump, labeled I to IV in Fig. 4.4b, show that the centerline velocity increases along the stream compared to overlapping profiles for the incompressible fluid (not shown here).

The net force from the linear momentum equation, the last two terms in Eq. (4.4), contribute slightly to the total force applied in the pump, ~ 3.5% as

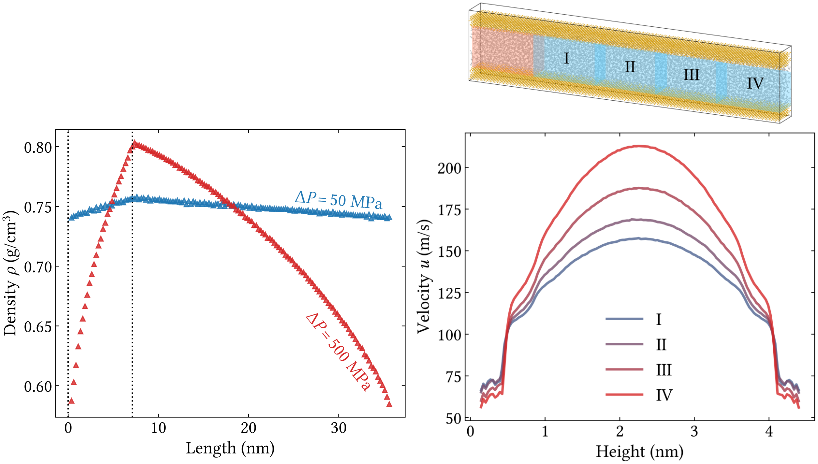

(a) **(b)**

Figure 4.4.: **a.** Density variation along the length at low $\Delta p = 50$ MPa and high $\Delta p = 500$ MPa using the FF pump. **b.** Velocity profile evolution along the stream for the $\Delta p = 500$ MPa case.

shown in Fig. 4.5. In spite of the significant variation of the fluid properties along the stream, the contribution of the momentum flux terms remains small. This agrees with the finding of Liang et al. [62], where they concluded that ignoring these terms still resulted in a pressure difference that did not deviate from the target value.

The fluctuations in the pump force are dominated by the F_{wall} fluctuations. However, the major contribution to F_{pump} is from the pressure difference F_{p} force. The fact that F_{p} does not deviate by far from the time-average indicates that the gap height does not vary significantly during the flow simulation i.e. hydrodynamic lift is small. The gap height was measured along the whole NEMD simulation time to evaluate hydrodynamic lifting. Only an increase of 4.4% was observed.

Applying larger Δp (or $\dot{m}$) is possible, however, the liquid beomes susceptible to cavitation as the tensile strength is reached once the pressure drops below the vapour pressure. Hence, the pump becomes the nucleation site for cavitation.

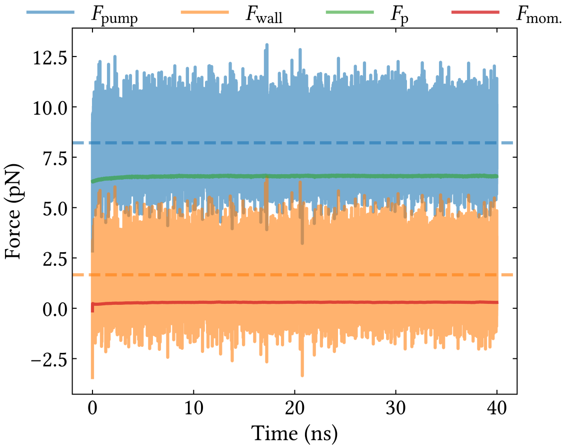

Figure 4.5.: Time series of the forces in the pump using the FF method using $\Delta p = 500$ MPa. Dashed lines are the time-averges of the respective quantities.

4.3.3. Wall-fluid interaction

The aim of this section is to validate the pump method for fluids with different wetting conditions and quantify the effect of the wall-fluid interaction on the fluid transport.

The wall-fluid interaction strength (or hydrophobicity) can be tuned with the Lennard-Jones parameter ϵ_{ij}, as described in Sec. 3.1. The lower the interaction energy, ϵ_{ij}, the more hydrophobic the surface becomes (or the more non-wetting the fluid is).

The pump was applied on three fluids with different wettabilities with a perturbation of $\Delta p = 50$ MPa in the FF pump (and its equivalent $\dot{m}$ in the FC variant). Fig. 4.6.a shows that the velocity vanishes near the walls for the wetting fluid. However, for the intermediate and non-wetting fluids, slip against the walls becomes more pronounced. The slip velocity u_{slip} is larger than the difference between the centerline velocity and the fluid velocity at the walls.

The velocity data of the three fluids can still be fit to the quadratic hydrodynamic function. Since the velocity profile is symmetric around the channel's center, the slip length is the same on upper and lower walls.

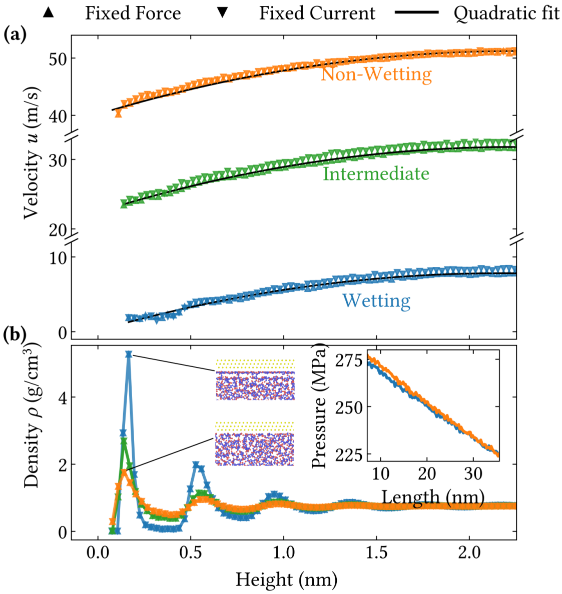

Figure 4.6.: **a.** Velocity and **b.** density profiles along the gap height h (only half h is shown) for non-wetting, intermediate-wetting and wetting fluids. Inset: the fluid pressure variation in the pressure-driven region for the wetting and non-wetting fluids. Snapshots of the box with the wetting and non-wetting fluids to show the formation of a monolayer near the walls in the former but not the latter.

For the wetting and the intermediate-wetting fluids, the density profiles (Fig. 4.6b), shows sharp peaks. Due to the high surface-fluid attraction, the fluid population near the wall is higher and more ordered, thus forming a distinct monolayer represented in the first density peak. In equilibrium, this high degree of ordering was evident from the structure factor evaluation. This ordering or layering persists even at higher pressure gradients and manifests in oscillations in pressure and temperature profiles near the walls, see Fig. 4.4b and Fig. 4.9.

The density profiles show a second peak representing a second monolayer and approaching the fluid bulk, the density smears out and the oscillations dampen. Similar profiles were reported in Refs. [13, 137, 138].

As the interction becomes weaker, the fluid and solid become decoupled and the fluid near the walls behaves similar to the bulk fluid i.e. less ordered. For the non-wetting fluid, the first peak has smaller amplitude and larger width than the other fluids. The dampening of the oscillations occurs closer to the walls and the density reaches the same bulk density as the other fluids.

The fluid pressure, measured in the bulk, is evaluated for the wetting and non-wetting fluids, shown in Fig. 4.6.b inset. The average virial pressure as well as the shear stress at the walls σ_{xz} (not shown here) are independent of the wall-fluid interaction.

Wall Slip & transport

For pressure-driven flow, the transport properties of the fluid vary along the gap height due to the parabolic nature of the velocity profile. Therefore, the transport properties (η,$\dot{\gamma}$) are only reported at the interface. Transport properties for fluids with different wettabilities are shown in table 4.1. The mass flow rate was measured in the sampling region as follows,

$$\dot{m}_x = \frac{\sum_i^N m_i u_i}{L} \tag{4.9}$$

where L and N are the sampling region length and the atom count.

ϵ_{ij}/ϵ_0	$\dot{\gamma}$ ($10^9 s^{-1}$)	η (mPa.s)	b (nm)	u_{slip} (m/s)	$\dot{m}$ (10^{-10} g/s)
0.01	9.13	0.50	4.28	34.3	4.68
0.2	8.32	0.54	2.89	23.4	2.81
1	7.13	0.60	0	1.88	0.52

Table 4.1.: Fluid transport properties, slip and mass flow rate for different wall-fluid interaction strengths. The potential depth ϵ_{ij} is normalized by ϵ_0, which is obtained from the geometric combining rules for ϵ_i fluid pseduatom and ϵ_j solid atom.

Near the walls, the non-wetting fluid experiences a higher shear rate and a lower shear viscosity relative to the wetting fluid. A strong correlation between wetting and slip is observed, this was also reported in Refs. [13, 74]. For the non-wetting fluid, the slip length exceeds the time-averaged channel height ($h \sim 4.2$ nm). The slip length b does not increase signigicantly with shear rate. Simulations of the wetting fluid at a shear rate ranging from $\mathcal{O}(10^9)$ to $\mathcal{O}(10^{11})$, showed an increase in b from 0 to 0.4 nm. This observation agrees with the deduction of Martini et al. [139], who argued that for non-rigid walls, b becomes independent of $\dot{\gamma}$ due to friction forces, which become dominant at high shear rates.

Slip enhances the fluid transport in confined channels. The mass flow rate is larger for the non-wetting fluid due to the reduced friction with the walls. This can also be deducted from the macroscopic Hagen-Poiseuille relation, which defines the mass flow rate as the integral of the velocity profile. From the NEMD simulations at different $\frac{\partial p}{\partial x}$, the mass flow rate varied linearly with the pressure gradient. The results agree with the continuum prediction when slip is accounted for, in the Hagen-Poiseuille equation.

For nanoconfined wetting fluids, the evaluation of transport properties becomes complicated due to layering, as illustrated in Fig. 4.7.

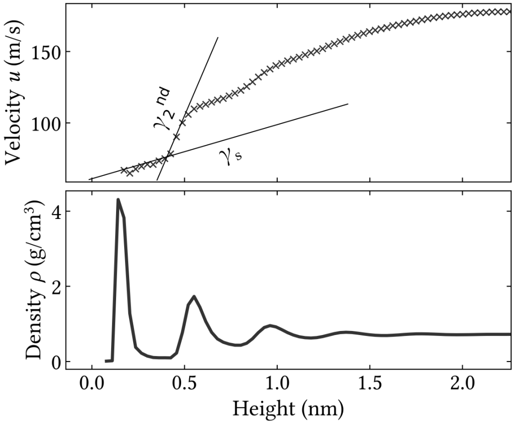

Figure 4.7.: Correlation between density and velocity for the wetting fluid. Layering affects transport coefficients along the gap heigh, where γ_s is the shear rate evaluated between the first and second monolayers and $\gamma_{2\mathrm{nd}}$ is the shear rate at the second monolayer. The fluid is under a pressure difference $\Delta p = 500$ MPa in the FF pump.

As the gap height h becomes larger, we approach the hydrodynamic assumption of no-slip boundary condition. The effects of slip and layering becomes smaller when $b << h$.

4.3.4. Thermostating the fluid-wall system

During the NEMD flow simulation, work is done continuously on the fluid and viscous heating is inevitable. In this study, the objective is to monitor the temperature of the fluid following the pump perturbation, compare the NEMD temperature profiles with the hydrodynamic predictions and determine the most appropriate thermostating strategy compatible with the pump. To achieve the last objective, four different thermostating techniques were employed in order to provide a presepctive on how different thermostating strategies can result in different temperature measurements.

In all four strategies, the pump is under FF conditions. The first three strategies were based on thermostating only the walls. The walls were stationary, therefore there is no sliding velocity bias and the thermostat was coupled to all three cartesian directions. The thermostats used were the Langevin thermostat (TW-LGV), the Nosé-Hoover thermostat (TW-NH) and the Berensen thermostat (TW-BE). The fourth strategy is to apply a Nosé-Hoover thermostat directly and only on the fluid (TF-NH) in the perpendicular-to-flow perpendicular-to-load direction i.e. the thermostat was applied only in the y-direction to avoid the fluid streaming bias. For the TF thermostat, the wall atoms were rigid.

In all of the aforementioned strategies, the initial equilibration of the fluid, 0.06 nanoseonds, was carried out with a Berendsen thermostat. In the production equilibration, 2 ns, and untill the end of the NEMD simulation, the Berendsen thermostat was switched off. In the TW systems, the fluid then sampled NVE dynamics and in the TF system, a Nosé-Hoover thermostat was imposed on the fluid.

For the solid in the TW systems, the initial and production equilibrations (as well as NEMD simulations) were conducted in the NVT ensemble with the respective thermostat. The damping constant for all thermostats was 100 fs and the target temperature was 300 K.

At low pressure gradients (at Δp = 50 MPa and Δp = 250 MPa), the fluid temperature (solid lines in Fig. 4.8) slightly increases due to the imposed force

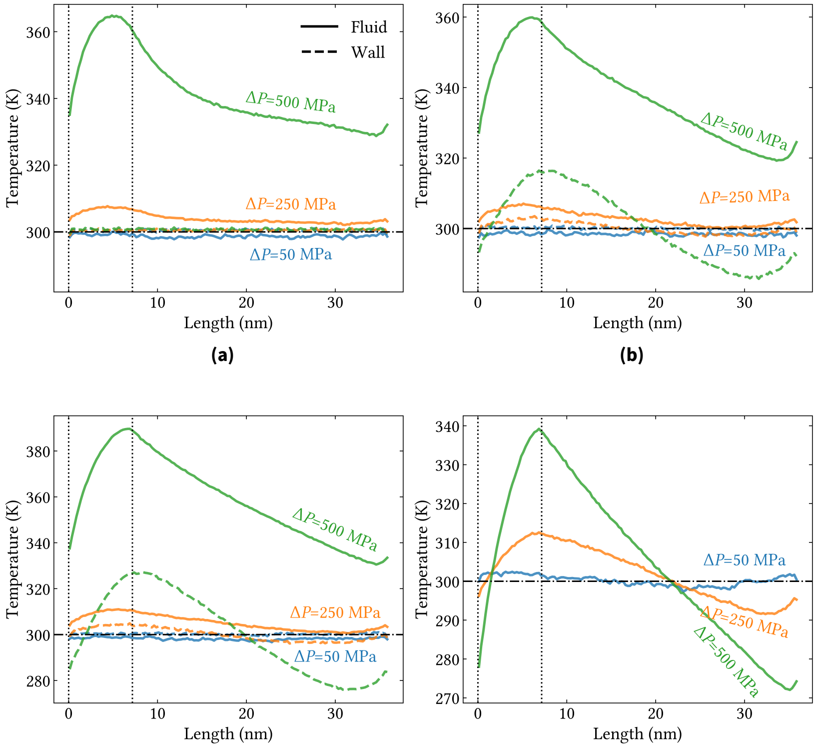

(a)

(b)

(c)

(d)

Figure 4.8.: Temperature profiles along the stream-wise direction at Δp= 50, 250 and 500 MPa using the FF pump. Thermostating strategies are: **a.** TW-LGV, **b.** TW-BE, **c.** TW-NH and **d.** TF-NH. The vertical dotted lines represent the pump bounds and the dashed-dotted horizontal line is the target temperature.

in the pump and drops in the pressure-driven region. As for the temperature measured in the walls (dashed lines in Fig. 4.8a to c), the TW-LGV (Fig. 4.8a) controls the temperature perfectly in the walls unlike the determinstic thermostats TW-BE (Fig. 4.8b) and TW-NH (Fig. 4.8c), where they both show a similar temperature profile to the fluid. This implies that the fluid temperature profile could be a result of thermal diffusivity from the walls. For the

TW-LGV system, the temperature in the walls and in the fluid is uniform and does not increase in the pump.

At high pressure gradients ($\Delta p = 500$ MPa) for all the systems, the temperature gradient in the fluid becomes more prominent. The determinstic thermostats still induce a temperature gradient within the solid wall. The TW-LGV keeps the temperature uniform in the solid while a temperature gradient develops in the fluid. A detailed discussion and analysis of this finding is given in App. B

The TF-NH (Fig. 4.8d) system shows a temperature variation in the fluid even at the intermediate pressure gradient (at $\Delta p = 250$ MPa). The temperature gradient becomes more significant at larger shear rates. The Nosé-Hoover thermostat fails to set the fluid temperature in each bin along the gap height to 300 K. However, the median of the whole fluid temperature remains at 300 K.

At the lowest pressure gradient, the temperature profiles along the gap height, in Fig. 4.9, are uniform in the fluid bulk for all systems. As Δp increases to 50 MPa, the data can be fit to the quartic function in Eq. (2.11). The bulk temperature is of the same magnitude for all thermostating strategies except the TW-NH system, which shows slightly higher fluid temperature. At $\Delta p = 500$ MPa, the quartic profile becomes more visible for the TW systems. The TW-NH system still gives a higher fluid temperature than the TW-LGV and TW-BE systems. For the TF system, at large pressure gradients, the profile becomes parabolic with a minimum in the center of the channel. This profile was reported by Bernardi et al. [84] to be unphysical.

A common feature in the temperature profiles along the gap height, in Fig. 4.9, is the oscillations near the wall. These oscillations are related to density oscillations (or the layering effect) shown in the previous subsection.

The simulations reported so far were performed on a fluid under a confinement of ~ 4.2 nm, i.e. a confinement equivalent to 7 molecular diameters. As the gap height h increases, the temperature and velocity profiles approach the hydrodynamic solution further. Conversely, a deviation becomes noticeable as h decreases i.e. as we approach the boundary lubrication regime. Simulations of the fluid under different levels of confinement were performed by halving and doubling the number of fluid atoms to reach $h \sim 2$ nm and $h \sim 8$ nm under the same external pressure $p_{\text{ext}} = 250$ MPa. The target temperature was set to $T = 300$ K for all simulations using the TW-LGV thermostat. The

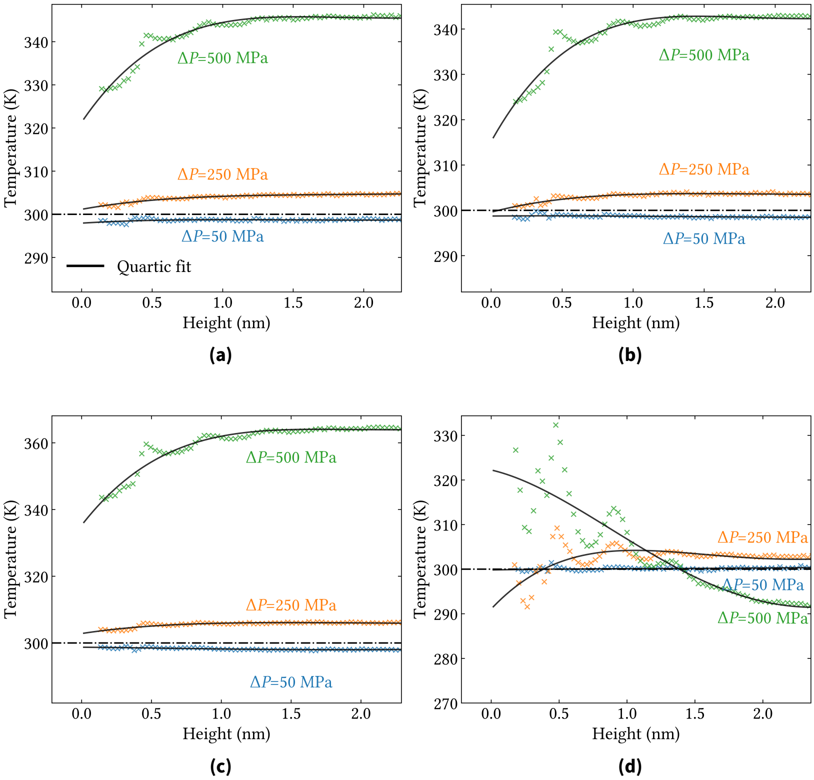

Figure 4.9.: Temperature profiles along the gap height (only half is shown) at Δp= 50, 250 and 500 MPa using the FF pump. Thermostating strategies are: **a.** TW-LGV, **b.** TW-BE, **c.** TW-NH and **d.** TF-NH.

number of spatial bins in the z-direction was proportional to the gap height, 72, 144 and 288 bins were used along the gap height for the $h = 2, 4, 8$ nm simulations, respectively.

These set of simulations were performed at similar shear rates $\dot{\gamma}$, which was tuned through Δp in the FF pump. Given the linear relation $\dot{\gamma} \propto \frac{h}{2\eta}\frac{\partial p}{\partial x}$ at $z = h$ from the Poiseuille velocity profile (Eq. (2.6)), by doubling the gap height, the pressure difference was halved. Due to slip, $\dot{\gamma}$ is not expected to be

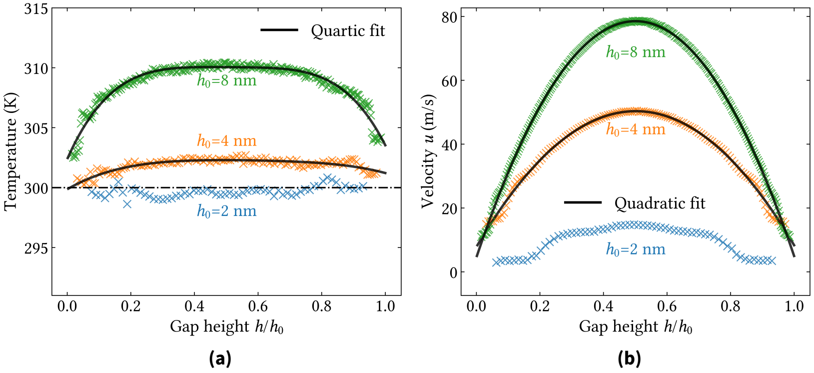

Figure 4.10.: a. Temperature and **b.** velocity profiles along the gap height for fluids under different confinements using the FF pump and the TW-LGV thermostating strategy. The distance in the z-direction is normalized by the gap height.

exactly the same in all simulations. The shear rates measured at the wall were $\dot{\gamma} = 3.4 \times 10^{10} s^{-1}, 3.9 \times 10^{10} s^{-1}, 3.2 \times 10^{10} s^{-1}$ for $h = 2, 4, 8$ nm, respectively.

From Fig. 4.10a, the temperature and velocity profiles for the intermediate and large gap heights can be fit to the quartic and quadratic functions (the hydrodynamic solutions), respectively. However, for the smallest gap height ($h = 2$ nm), a deviation from the hydrodynamic solution is prominent. At this level of confinement, the constituitve equations might not hold as transport coefficients become highly nonlocal in space.

5. Hydrodynamic cavitation

In the previous chapter, the pump introduced a pressure gradient along the flow. Due to the use of flat walls, the minimum pressure in the channel is always at the pump inlet while the maximum pressure is at the pump outlet. If the liquid pressure p_l drops below the vapor pressre p_v or more specifically $p_\mathrm{l} < p_\mathrm{v} - 2\gamma/R$, where γ and R denote the liquid-vapor surface tension and bubble radius, respectively, the liquid "breaks" [29]. This creates a void or bubble in the liquid i.e. leads to cavitation nucleation.

With the pump method implemented in a slab geometry, cavitation can only occur at the pump inlet, where the pressure is lowest. Therefore, the bubble nucleates in the pump region, where the perturbation field is applied. In order to study the bubble dynamics, the bubble nucleation site should be shifted away from the perturbation. In other words, the pressure profile should be manipulated such that the minimum pressure is not at the pump inlet rather at an arbitrary location in the pressure-driven region.

To achieve this goal, the wall geometry needs to be changed to allow for a local velocity and pressure variation such that the pressure drop occurs at an expansion following a constricted cross-sectional area e.g. venturi nozzle or an orifice. Therefore, a converging-diverging wall setup was used here. The first part of this chapter is focused on the geometrical parameterization of the channel walls in order to manipulate the bubble nucleation site.

The second part of the chapter focuses on understanding cavitation dynamics in a non-equilibrium scenario. In equilibrium, the bubble radius was compared to the static Young-Laplace equation (Sec. 3.6). The nucleation-collapse behaviour in a flowing liquid can be compared to the hydrodynamic Rayleigh-Plesset equation.

The interaction potentials as well as the NEMD simulation procedure used in the previous chapters for *n*-pentane were also used here. The focus of the study is to investigate the effect of geometry on the pumped fluid pressure, rather than computing the fluid temperature. Therefore, the following simulations involve a Nosé-Hoover thermostated fluid confined between rigid walls. This presents a caveat if one is interested in computing the fluid temperature especially for measuring the temperature of the bubble. Although, as reported in Sec. 4.3.4, the Nosé-Hoover thermostat showed unphysical temperature profiles and different thermostats can give different temperature profiles, the pressure profiles of all thermostating strategies are identical (see App. B). Therefore, the thermostat does not play a major role in how the pressure develops in the channel i.e. the pressure profile and so the bubble nucleation site should not be dependent on the thermostat used. However, care should be taken when interpreting the bubble dynamics with the thermostat applied directly on the fluid (further details in Sec. 6.2).

5.1. Nucleation site

Using Bernoulli's principle (Eq. (2.38)), a pressure drop (and an increase in velocity) in the fluid occurs as the fluid flows through a constriction. Change in pressure is possible by changing the wall geometry from slab walls to a venturi, orifice or dimple geometries. In the following simulations, the FC pump was favoured since the gap height encoded in the FF formulation (Eq. (4.4)) is changing in the channel and so the measured Δp differs from the imposed in the FF pump. On the other hand, the mass flow rate imposed in an FC pump is independent of the channel geometry.

For the first iteration of the channel geometry, a venturi of a wide-narrow-wide setup was initialized. The pump lengh is $0.1\,L_x$ and was positioned once in the narrow and once in the wide region in order to study the effect of the pump location on the fluid pressure profile. The external pressure on the upper wall was 250 MPa and the applied mass flow rate was 5×10^{-10} g/s, which resulted in an intermediate pressure difference ($\Delta p = 300$) MPa in the slab geometry of $h = 4$ nm and $L_x = 36$ nm. The pressure reported here (and for the rest of the chapter) is the bulk pressure measured in a central region of constant thickness equidistant from the converged walls. The result is shown in Fig. 5.1.

The pressure drop in the curved regions is non-linear and becomes linear in the flat portion of the channel, as shown in Fig. 5.1. The peak pressure in the

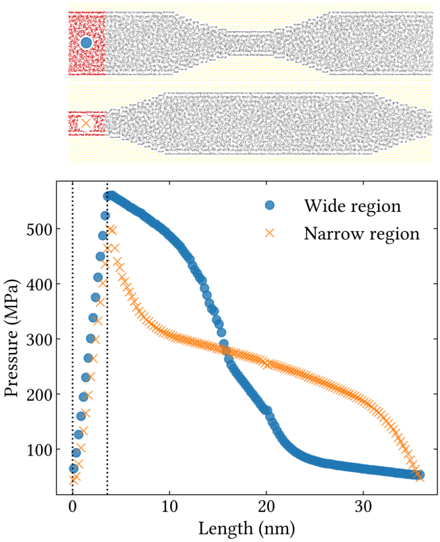

Figure 5.1.: Effect of pump location on the pressure profile in a venturi. The dotted lines highlight the bounds of the pump region.

pump is lower for the case of the pump in the converged region due to the difference in the mass flux.

By positioning the pump in the constricted region, the lowest pressure in the channel is concentrated at the pump inlet. On the other hand, pumping in the wide region creates a region of low pressure where bubble nucleation could be favourable. This can be seen in the linear drop within the second wide region, from 25 to 36 nm on the curve with blue markers. Based on this analysis, the pump shall not to be located in a highly constricted region within the converging-diverging domain.

The effect of geometrical features is evident from Fig. 5.2. Two geometries were used to analyse the pressure variation due to a gentle expansion (dimple geometry) and a sudden expansion (orifice). The upper wall is under a pressure of $p_{\text{ext}} = 50$ MPa, which is higher by three orders of magnitude than the vapor pressure ($p_{\text{v}} = 0.073$ MPa) of *n*-pentane at 300 K. Therefore, no cavitation is expected.

At the same imposed $\dot{m}$, a pressure difference Δp of 25 MPa and 60 MPa is obtained in the pump using the dimple and orifice, respectively. For the dimple geometry, Fig. 5.2a, the pressure drop is steep in the flat regions and very smooth and constant ($\Delta p = 0$) in the dimple region. Using the orifice, the pressure drop exhibits a gradual decrease in the flat regions and a sharp drop occurs within and beyond the orifice (in between the dashed lines in Fig. 5.2b) owing to the abrupt change in geomtry.

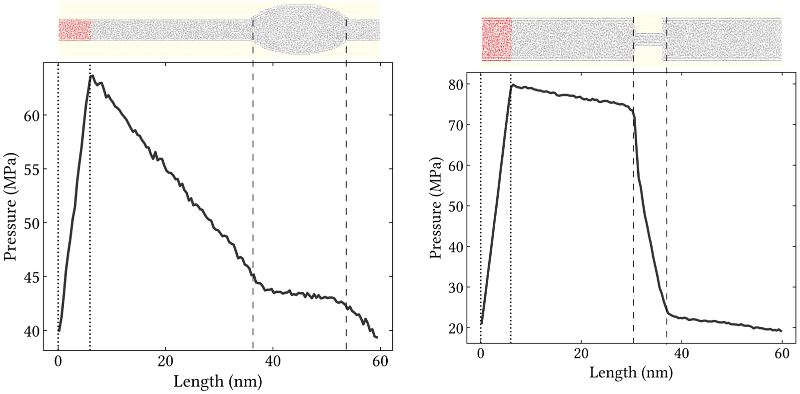

(a) **(b)**

Figure 5.2.: Converging-Diverging geometry implementation and the corresponding virial pressure in molecular domains with **a.** surface dimple and **b.** orifice. The dottend and dashed lines indicate the pump and the geometrical discontinuity bounds, respectively.

To avoid the computational expense and tedium of iterating through numerous geometry permutations to find a configuration where cavitation nucleates outside the pump, a solver based on continuum fluid mechanics can be employed for optimizing the wall geometry.

5.1.1. Continuum solution

The calclations were carried out with the continuum solver by Holey et al. [17]. The algorithm is based on a height-averaged two-dimensional solution to the flux function to obtain the densities of the conserved variables e.g. density and momentum. The continuum solver uses a finite volume discretization of the domain and an explicit time integration scheme (MacCormack's scheme

[140]) to solve for the densities of the conserved variables. To directly relate to molecular simulations, the timestep and the domain dimensions are in the order of fs and nm. The timestep is adaptive based on the choice of the Courant-Friedrichs-Lewy (CFL) number, here CFL=0.02. A low value was chosen to ensure the stability of the solver and that the numerical solution captures the dynamics of the system accurately at this length scale. The domain was discretized into 100 grid points in the flow direction.

The boundary conditions are specified in terms of pressure (or equivalently density) at the inlet and the outlet boundaries of the channel in the stream-wise x-direction i.e. Dirichlet boundary conditions were used. The channel is periodic in the span-wise y-direction. The lower wall in the continuum solver is assumed to be flat. This is to simplify the source term computation [17]. To compare directly with atomistic simulations, MD domains were also initialized with a lower flat wall, as shown in Fig. 5.3.

The compressibility of the fluid is accounted for through the equation of state, where the pressure-density relation is encoded. To represent n-pentane in the continuum solver, the cubic equation of state (see Fig. 3.2b) with a realization of the Elrod-Adams approach was used. The Bayada and Chupin EoS (Eq.(2.52)) was also used for comparison. The speed of sound in the liquid c_l and vapor c_v are 1386 m/s [121] and 189 m/s [141], respectively. The liquid and vapor densities at 300 K obtained from Fig. 3.5 were $625\,\mathrm{kg/m^3}$ and $2.19\,\mathrm{kg/m^3}$, respectively.

5.1.2. Molecular & Continuum profiles

The molecular geometries were implemented into the continuum solver in order to compare the continuum solution with the pressure-driven molecular simulations. The molecular domain geometry was replicated only in the pressure-driven region, i.e. the pump was omitted in the continuum calculations. The pump p_{out} and p_{in} are replaced here with the pressure values p_1 and p_2 at the boundaries of the continuum domain. This is shown in Fig. 5.3 for the pocket, dimple and orifice geometries.

Cavitation was controlled through the external pressure p_{ext}. For the non-cavitating flows, p_{ext} was set to 50 MPa while for cavitating flows, p_{ext}

was 5 MPa. In all the pressure-driven MD simulations (cavitating and non-cavitating), the applied $\dot{m}$ was set to 3.8×10^{-11} g/s, which is a low $\dot{m}$ value according to the slab geometry setup.

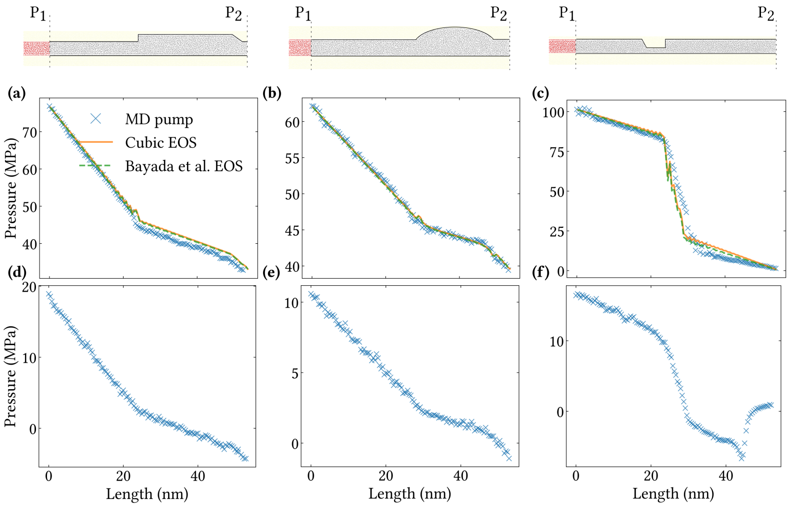

Figure 5.3.: Molecular dynamics and continuum pressure profiles of non-cavitating flow for the **a.** pocket, **b.** dimple and **c.** orifice channels. **d.** to **f** MD pressure profiles of the cavitating flow for the same geometries. The MD pressure profiles are shown for the FC pump in molecular dynamics simulations and pressure boundary conditions (p_1 and p_2) in the continuum solver. Note that the red highlighted region is the pump which is omitted in the continuum calculations. The black solid lines on the geometries represent the corresponding 2-dimensional geometries implemented in the continuum solver.

The continuum solution for pressure is almost identical to the virial pressure computed from the pressure-driven flow molecular simulations, Fig.5.3. Conforming with Fig. 5.2, the largest pressure difference is obtained when the orifice is employed (Fig. 5.3c). With the orifice geometry, the MD pressure profile undergoes the lowest pressure excursion within and beyond the constriction.

Roughly, cavitation occurs when the liquid pressure drops below $p_v - 2\gamma/R$. One common feature in the plots in Fig. 5.3d and e, is the monotonous drop in pressure. The pressure drops to negative values and recovers in the pump (omitted). For the pocket and dimple geometries, there was no distinct bubble rather an ensemble of bubbles with small radii and a short lifetimes. This is similar to “bubbly flows” [92]. For the orifice geometry, a large bubble nucleated at a distance of $\sim$ 14 nm beyond the constriction (at the dip in pressure in Fig. 5.3f). The bubble extended to the pump region and did not collapse or migrate in the channel. The results indicate that these geometries were not successful in shifting the cavitation nucleation site away from the pump.

The continuum calculations for cavitating flows are not shown here as the exact pressure p_2 is unknown. One can use the negative pressures obtained from MD, however, that can result in ambiguous densities according to the EoS. Since MD and continuum agreee to a great extent in non-cavitating flows, we can rely solely on the continuum solver for tuning the geomtry to aid cavitation outside the pump in the molecular domain.

5.1.3. Sensitivity analysis

Channel geometry optimization was achieved with the continuum solver. In this study, a mineral oil represented by the Dowson-Higginson EoS was used instead of n-pentane due to improved numerical stability especially near the abrupt geometrical changes. The EoS coefficients for Eq.(2.50) used were $p_\mathrm{c} = 61$ KPa, $C_1 = 2.22 \times 10^{10}$ and $C_2 = 1.66$. The coefficients were chosen according to the values used by Sahlin et al. [113] to fit to the compressibility data of a mineral oil except for C_1 which was chosen to be 1 order of magnitude larger to model an incompressible fluid. This was to ensure convergence and avoid reduce pressure oscillations near the geometrical discontinuities.

For a systematic study of the effect of geometrical features on the pressure profile, a senstivity analysis can be performed by changing four main parameters of the channel geometry. These are:

- Diverging-converging gap height ratio D/d
- Narrow region inlet angle α
- Narrow region outlet angle β
- Narrow region length (or throat length) l_t

Since the aim of the study is to investigate the influence of the geometrical parameters on the fluid pressure, the inlet and outlet pressure where chosen to be 80 and 25 MPa, repectively, which are much higher than that of p_{v}. In other words, the liquid did not cavitate in any of these calculations.

The results shown in Fig. 5.4 demonstrate how the liquid pressure develops as it exits the pump and flows in a wide-narrow-wide channel. Therefore, the venturi geometries shown in the figure would be entirely in the pressure-driven region in the molecular domain. The range of D/d investigated was from 2 to 6, while l_{t} ranged from 6 to 30 nm. The inlet α and outlet angles β were varied from 7° to 90°. The sharp change in the geometry results in numerical instabilities. As a consequence, large pressure oscillations occured at $\beta = 90°$ and was replaced with $\beta = 60°$.

The pressure profiles in Fig. 5.4 show a change of the pressure gradient slope from a slight drop in the wide regions to the steeper drop in the narrow region. It can be deducted that a pressure drop in the wide region can be maximized by increasing the D/d ratio (Fig. 5.4a), increasing β (Fig. 5.4b) and decreasing α (Fig. 5.4c). The last two parameters have a slight influence on the pressure profile compared to the D/d parameter.

The throat length has a minimal impact on the pressure drop, but it does influence the slope of the pressure gradient. Li et al. [142] obtained similar findings using computational fluid dynamics calculations concluding that D/d and β have the greatest influence on the fluid pressure variation in a venturi.

The results from the continuum calculations act as design guidelines for the molecular RVEs to aid in a larger pressure drop at the wide region and consequently lead to cavitation nucleation.

5.1.4. Geometry for cavitation in MD

From the continuum analysis, the MD channel was modified to implement a large D/d for the fluid when exiting the restriction. The MD geometry combined an orifice followed by a region of expansion, which is susceptible to cavitation. The corresponding profiles are shown in Fig. 5.5.

The applied p_{ext} was 5 MPa and a constant current was applied in the whole region before the constriction i.e. the FC pump length was $0.49L_x$. In Fig. 5.5, the pressure drop in the wide region from the sudden expansion is similar in shape to the profile obtained from the continuum calculations, Fig.5.4a.

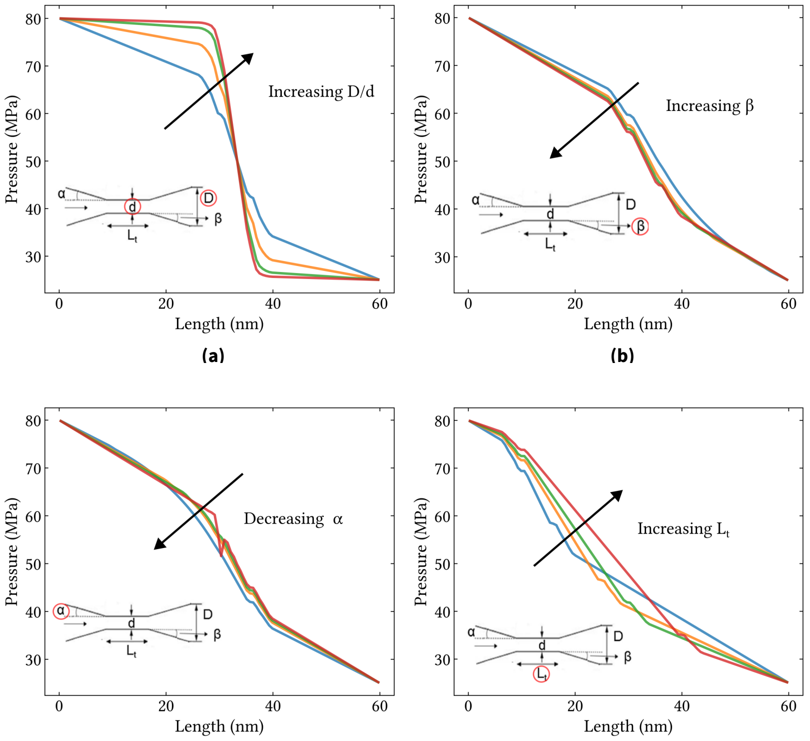

(a) (b)

(c) (d)

Figure 5.4.: Sensitivity analysis with the continuum solver by changing **a.** the diverging/converging gap height ratio, **b.** the outlet angle, **c.** the inlet angle and **d.** the throat length of the narrow region. The arrows point to the desired design guideline to achieve a larger pressure drop, therefore facilitating cavitation nucleation.

The flow remained laminar in the whole channel, Reynolds number < 1. The cavitation index K reached its lowest value after the flow constriction, where the x-component of velocity drops at the expansion. All of these simulations resulted in cavitation nucleation taking place outside the pump, beyond the constriction, but in varying ways.

For the nozzle and dimple geometries, the bubbles had small radii and a short lifetimes. This is again similar to Fig. 5.3d and Fig. 5.3e i.e. bubbly flows.

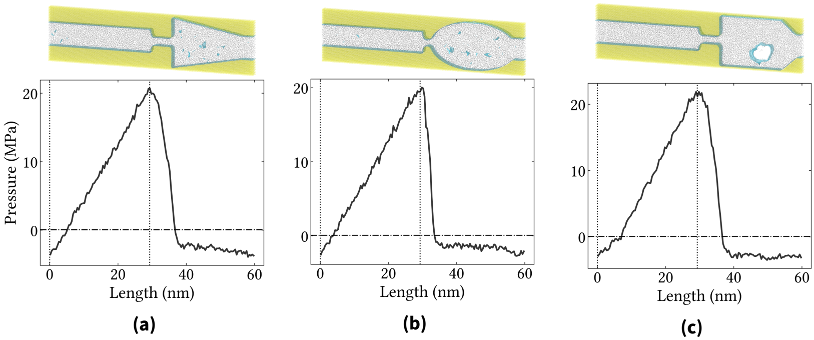

Figure 5.5.: MD configurations with cavitation outside the pump. Cyan surfaces represent the resulting surface mesh for the fluid highlighting the cavities. Vertical dotted lines highlight the pump boundaries and horizontal dashed-dotted lines are at $p = p_\mathrm{v}$

However, for the nozzle with the extended wide region, Fig. 5.5c, the bubble nucleation is reminiscent of a “traveling bubble cavitation”. In Ref. [92], this is defined as an isolated cavitation that grows from cavity nuclei and moves along the free stream.

The bubble in Fig. 5.5c travels from its nucleation location, as it is pushed by the upstream jet from the constriction, to the pump inlet where the pressure recovers (higher pressure zone) and collapses there.

5.2. Cavitation Dynamics

The nucleation and collapse of the bubble in Fig. 5.5c can be monitored and compared to the hydrodynamic Rayligh-Plesset (RP) equation. Eq. (2.45) rather than the full form Eq. (2.46) was used since there is no dissolved air or contaminant gas in the bubble i.e. only $p_\mathrm{v} - p_\mathrm{l}$ pushes the bubble boundary to grow. Additionally, the viscosity effects are discarded in this analysis.

The nucleation-collapse occurs multiple times during the course of the simulation. Each nucleation event is accompanied with a hydrodynamic lift as the bubble pushes the walls counteracting the applied p_ext. This is shown in Fig. 5.6 where a bubble growth (inset) results in hydrodynamic lifting.

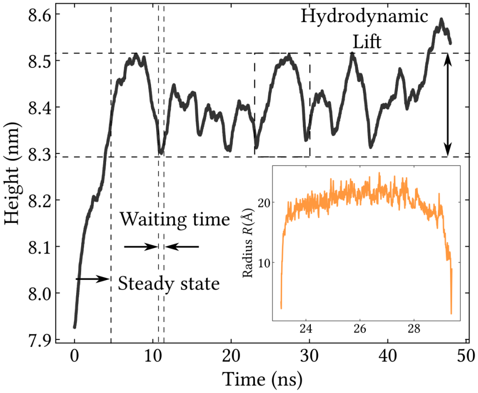

Figure 5.6.: Channel average (narrow and wide) gap height. Inset: bubble radius monitored in the timeframe highlighted on the gap height profile.

To understand the dynamics of a single nucleation-collapse event, the RP equation can be solved with the initial bubble radius and interface velocity $(R_0, \dot{R}_0)$ as the boundary conditions. The pressure p_∞ is not known a priori. Assuming that pressure in the liquid away is the same as the applied hydrostatic pressure $p_\infty = p_{\mathrm{ext}}$, results in a strong deviation of the MD data from the hydrodynamic RP prediction.

To clarify, consider a small bubble initial nucleus radius $R_0 = 0.1$ Å with an initial velocity of $\dot{R}_0 = 0.05$ Å/fs within *n*-pentane (liquid-vapour surface tension $\gamma = 12.5$mN/m at 300 K). The choice of $\dot{R}_0$ is simply to match the MD data slope dR/dt during nucleation. Using $p_\infty = p_{\mathrm{ext}} = 5$ MPa, the RP equation predicts that the bubble does not grow i.e. the vapour phase is not stable.

Reducing p_∞ by 2 orders of magnitude (from 5 MPa to 0.0736 MPa) such that $p_\infty - p_{\mathrm{v}} = 560$ Pa, the lifetime of the bubble matches the MD data, as shown in Fig. 5.7. The RP overestimates the critical radius, the radius after which the bubble starts collapsing. Moreover, the RP estimates that the bubble will start collapsing once the critical radius is reached. On the other hand in molecular simulations, the bubble radius remains constant the majority of its lifetime.

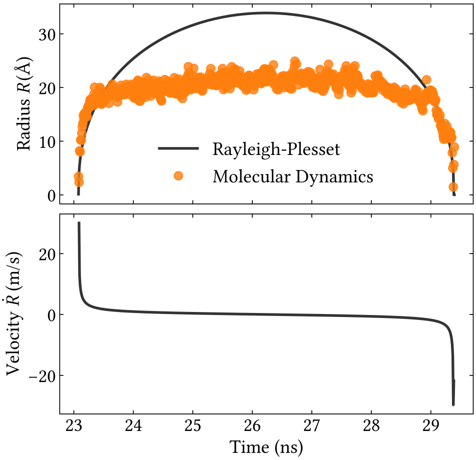

Figure 5.7.: Bubble radius from MD in comparison with the ODE solution to the Rayleigh-Plesset with the boundary conditions (R_0,$\dot{R}_0$).

The cavity accelerates near collapse. In Fig. 5.7, the initial and final velocities were omitted in order to visually inspect the change in velocity without these extremes. The nucleation and collapse slopes are identical, thus $\dot{R}_0 = \dot{R}_{\text{collapse}} = 5000$ m/s. Experimental measurements of $\dot{R}$ for micrometer-sized bubbles in water at room temperature ranged from 1200 to 1600 m/s [143].

Ignoring the liquid-vapour surface tension does not affect the RP model significantly. This finding agrees with Refs [29, 116]. Including $2\gamma/R$, elongates the bubble lifetime slightly. This is expected since the surface tension term accelerates the motion of the bubble.

The larger the applied $\dot{m}$, the larger the pressure drop at the expansion and the more frequent cavitation occurs. Fig. 5.8a shows that increasing $\dot{m}$ by a factor of 2 increases the maximum bubble radius from ~ 20 Å to ~ 30 Å and decreases the bubble lifetime. The RP solutions were obtained as previously, by assuming $R_0 = 0.1$ Å, fitting R_0 to the collapse slope and adjusting p_l to fit the cavity lifetime from MD data. The nanobubble nucleation and collapse is still comparable to the hydrodynamic description although the bubble is cylindrical. The RP always predicts a larger cavity radius.

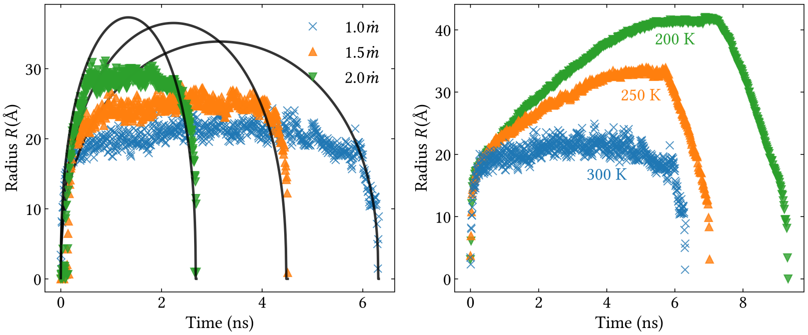

(a) **(b)**

Figure 5.8.: Bubble radius change with **a.** mass flow rate at 300 K and **b.** temperature at $1.0\dot{m}$. The solid black lines in **a.** are obtained from the Rayleigh-Plesset solution by choosing $R_0 = 0.1$Å, fitting $\dot{R}_0$ to the nucleation slope and choosing p_l that matches the bubble lifetime.

A decrease in the liquid temperature from 300 to 200 K prolongs the lifetime of the cavity by $\sim$ 2.9 ns, as seen in Fig. 5.8b. A similar observation was also reported by Lugli et al. [117] for water systems. Although, they started from a spherical cavity collapse in equilibrium. By reducing temperature, the bubble takes longer time to grow and its nucleation and collapse become highly asymmetric. Beyond the critical temperature ($T >\sim 470$ K), no cavity nucleation takes place rather single phase supercritical fluid flow.

6. Discussion

The aim of this chapter is to present a discussion on the results obtained from the pump method, how the method can be adapted to other flow scenarios and other fluids. Additionally, the possible limitations are highlighted. The hydrodynamic cavitation results are revisited and further explained in the context of the juxtaposition of the microscopic and macroscopic descriptions of cavitation in addition to the evolution of bubbles from atomistic simulations and hydrodynamic formulation. Finally, a brief overview of how the molecular simulations can be integrated within an MD-continuum coupling scheme is provided.

6.1. Evaluation of the pump method

The main motivation for using the pump method is to induce a pressure-driven fluid flow in periodic molecular domains with slab geometries, as well as any arbitrary geometry. The interest in slab geometry stems from the fact that a single molecular RVE is to model a macroscopic asperity without the need for an explicit specification of the geometrical features rather the pressure variation about it.

In the pump region, a perturbation is applied, the fluid gets perturbed and in the pressure-driven region, it undergoes constraint-free dynamics. Fluid compression-expansion can be seen in Fig. 4.3a to c, where an increase in the hydrostatic pressure (and bulk density) at the pump outlet leads to a drop in the stream velocity. This is equivalent to a fluid flow through a channel with varying gap height.

Molecular models do not need an explicit imposition of mass and momentum balance in the domain. At steady state, the mass flux along the flow direction j_x converges to a constant value. Mass conservation is realised such that the increase in density in the pump (Fig. 4.3b) is balanced by the drop in velocity (Fig. 4.3c).

As the imposed pressure gradient (or mass flux) is ramped up, $\dot{\gamma}$ increases and the fluid becomes more compressible. This results in a non-isothermal flow even when an appropriate thermostating strategy is used (see Fig.4.8a). The stability of the method is demonstrated in Fig. 4.5, where the applied force converges rapidly even at high Δp. The large fluctuations in the friction term F_{wall} originate from the thermal fluctuations in the pairwise forces between the solid and the fluid in the pump. These fluctuations dominate the fluctuations in the total pump force, however they do not affect the average imposed force.

The pump method is superior to the conventional methods of imposing a constant force on all atoms for a crucial reason. Although the gravity-fed method induces fluid flow in confined channels, the fluid is not driven by a pressure gradient rather a constant force. Therefore, the fluid is constantly under a perturbation that biases the dynamics and limits the study of transport properties and physical phenomena. The pump method is robust, computationally-inexpensive and converges faster than particle insertion-deletion methods.

The pump supports a large range of shear rates. For *n*-pentane, this was from 10^8 to 10^{11} s^{-1}. Beyond the upper limit, the fluid reaches its tensile strength and cavitates. Below the lower limit, the pump field becomes indistiguishable from the thermal motion. Lower shear rates are accessible by increasing the system size or longer sampling time. Although the shear rates used in simulations are considered high relative to experiments, they are comparable to the actual shear rates encountered in high performance lubrication applications [144].

6.1.1. Force or Current field

A pivotal advantage of the method is the interoperability, where the non-equilibrium ensemble the thermodynamic flux (N,V,T,J) or the thermodynamic force (N,V,T,F) are the state variables. The latter approach has been employed extensively in literature [59–62]. If the target is to perform a simulation at a certain $\frac{\partial p}{\partial x}$, the FF provides a straightforward implementation where only the pressure difference Δp is the required input for the specific domain length. However, there are three main scenarios where a pump based on imposing a force falls short.

First, when the separation of forces in cartesian coordinates is not possible, for non pairwise-potentials e.g. many body potentials [145]. Consider solid walls described with an embedded atom model (EAM) potential [146], the evaluation of the friction term ($f_{ik,x}$ in Eq. (4.4)) becomes complicated. The current implementation of the FF pump allows only pairwise interaction between the fluid and wall atoms. However, the FC pump does not suffer from such limitation thus allows a more accurate representation of the walls and hence the wall-fluid interaction.

Second, when the pressure gradient is not known a priori. This is the case for modelling systems in nature where the particle current through a nanotube or a membrane [50] is known rather than the pressure gradient. Using the current as the constraint is also useful in a multiscale modelling scheme, where the mass flux is thought of as the thermodynamic constraint imposed from the continuum model in a recursive continuum-atomistic scheme. This will be further explained in the multiscale coupling algorithm, Sec. 6.3.

The FF pump formulation includes the gap height in the F_p term, which limits its application to flat channels. In converging-diverging geometries, the measured Δp differs substantially from the imposed values. The FC pump is independent of geometry and can be applied in an irregular portion (rough surface) in the domain. The steady state mass flow rate will converge to the imposed value.

Moreover, the FC method reaches steady state faster than FF. The time it takes to reach a converged mass flux is much shorter than the time needed to reach a converged pump force at the same pressure gradient in the channel (see Fig. 6.1). However, for long enough simulation time, this does not present a hurdle.

6.1.2. Surface wetting

Tuning the wall-fluid interaction strength can model the surface hydrophobicity (or fluid wettability). This can be useful to mimic lubrication on coated surfaces e.g. hydrophobic diamond-like carbon [147] or liquids confined in nanoporous medium [148]. As the surface becomes more hydrophobic, the fluid dynamics become more diffusive near the walls thus increasing the slip

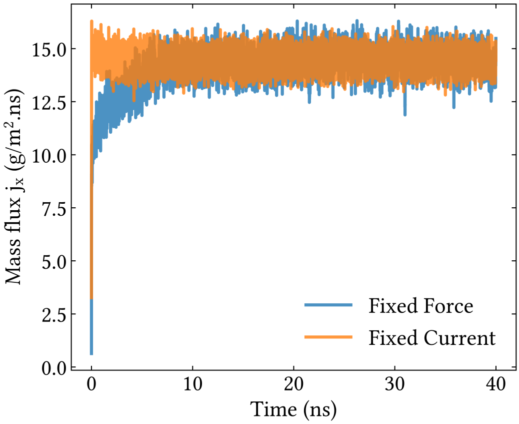

Figure 6.1.: Mass flux time series for the fixed force and fixed current variants of the pump.

length. Slip could be due to the formation of a gaseous layer from shearing against the walls [72].

For hydrophilic surfaces, wall-induced ordering is remarkable and manifests in the formation of fluid monolayers, Fig. 4.6. Layering is prominent in temperature and pressure profiles along the gap height, Fig. 4.9. For gap heights larger than 5 molecular diameters, the transport properties are weakly dependent on the wall-fluid interaction strength because transport is dominated by the bulk behavior.

Ordering is expected to diminish with increasing temperature and can be enhanced with commensurable fluid and wall densities [13] since more fluid atoms can fit themselves between the solid. Mismatch between the wall lattice constant and the nearest neighbor in the adjacent fluid layer can also facilitate ordering [74].

At a certain distance from the walls, the wall-fluid interaction plays a minor role in the properties of the fluid. If the thermodynamics quantities are averaged on scales larger than the mean free path (van der Waals radius σ of the fluid), the oscillations' effect diminish and we recover the macroscopic picture of a constant viscosity and shear stress as well as a perfectly parabolic Poiseuille velocity profile.

6.1.3. The lubricant molecule

The atomic force (or acceleration) in the pump is independent of the size and the charge of the lubricant molecule. The applied perturbation is derived from mass and momentum conservation equations which hold at any length scale.

For charged molecules, the electrostatic long range forces are handled with the Ewald sum or particle-particle particle-mesh (PPPM) method [149]. These interactions are added to the force field potential of all fluid atoms in the domain. Therefore, the relative force, F_{pump}, between the pumped and free atoms is not affected. App. C demonstrates the functionality and equivalence of the FF and FC pump variants on the lubricant molecule, squalane.

Modelling of fluid mixtures can give an insight on the chemical activity of lubricants. The lubricant's physical and chemical properties can be controlled by tuning the chemical composition of the base oil [150]. This approach allows for a more comprehensive investigation of the properties of lubricants and their performance in various applications. modelling mixtures allows, for instance, determining the effect of additives on the viscosity index of a lubricant or on the load bearing capacity of the lubricant film. The pump field can be applied not only on a pure fluid but also on a fluid mixture, see App. C.

6.2. Cavitation

The small length and time scales involved in the bubble collapse render molecular dynamics well-suited for investigating cavitation. Advanced continuum models which use homogenized equations of state are yet simplifications of the complex phase transition and thermodynamic changes in the fluid. Moreover, the macroscopic hydrodynamic theory incorporate approximations that could be valid for a macroscopic flow but fall short to cover the highly fluctuating nature of vapour bubbles.

The mechanical and thermodynamical drive for cavitation growth is the pressure difference $p_{\text{v}} - p_{\text{l}}$. Hence, a low p_{ext} shifts the pressure profile below the vapour pressure (Fig. 5.3), allowing the liquid to reach its tensile strength and cavitate. This leaves us still with the nucleation site problem, where the shifted pressure profile minimum is yet at the pump inlet.

Counterintuitively, using the pump in a converging-diverging channel does not necessarily imply cavitation will occur outside the perturbed region. With the configurations in Fig. 5.3, the pressure either drops monotonously or do not drop below p_v at the expansion rather close to the pump inlet. This could be remedied by adjusting the geometry as evident from the channels with the large D/d ratios. However, as interpreted from Fig. 5.5, this provides a partial solution. Although, the cavitation nucleation was successfully shifted, the bubble still migrates to the pump, therefore, tainting the collapse dynamics. This could manifest in artificial collapse profiles. The steep collapses at lower temperatures (Fig. 5.8b) could be an example of the cavity dynamics being affected by the pump perturbation field. For evaluating the cavity dynamics correctly through its entire lifetime, the collapse should also take place outside the pump. Moreover, the dynamics studied so far in Sec. 5.2 involved only a single cavity among many that nucleated and collapsed in a simualtion run. For improved statistical representation, multiple nucleation/collapse curves should be averaged for several cavities.

For nucleation and collapse to occur outside the pump, the fluid pressure has to recover before entering the pump. This can be possible by attaching a wide region before the pump inlet in Fig. 5.5c. The quasi-constant pressure in Fig. 5.5 at the abrupt expansion (outlet angle $\beta = 90°$) can be attributed to backflow effects due to losses from the sudden expansion.

Two main improvements to the current MD model are applying the thermostat on the walls while the fluid undergoes constraint-free dynamics and using a larger cutoff radius or adding long range corrections for the LJ interactions. Applying the thermostat on the fluid could dampen the bubble dynamics and reduce its velocity as it migrates in the channel. Therefore, to capture the bubble dynamics without thermostated equation of motion, the thermostat is to be applied on the walls. Thermostating only the walls has been demonstrated, for flows for slab channels, to be the correct strategy.

The LJ cutoff radius plays a significant role in the liquid-vapour interface simulations at equilibrium, Sec. 3.4. In the liquid-vapour equilibrium simulations r_c was 24 Å while in NEMD simulations, $r_c = 10\,\text{Å}$. A small cutoff radius underestimates the surface tension at the bubble as force truncation effects adversly affect the interfacial properties. Hydrodynamic bubbles would show a similar behaviour. A larger LJ cutoff radius would increase the bubble surface tension and promote bubble growth.

Relation to the hydrodynamic formulation

The Rayleigh-Plesset equation in its simplified form used here, assumes certain idealized conditions, such as spherical symmetry, uniform pressure and temperature. In contrast, MD simulations take into account the complex interactions between individual atoms, which lead to deviations from the idealized behaviour. These deviations can lead to differences in the predicted bubble radius compared to the results obtained from MD simulations.

A fundamental difference between the molecular simulations presented here and the hydrodynamic equations is the shape of the cavity. Macroscopically, the void is perfectly spherical. As shown in liquid-vapour equilibrium simulations (Fig. 3.8) and nonequilibrium simulations (Fig. 5.5c) the bubble shape can differ based on the simulation domain dimensions and boundary conditions. For periodic systems in the stream-wise and span-wise directions, a cylindrical void is more likely to form in domains of high aspect ratio while a spherical void is expected to nucleate in domains of low apsect ratio. This can be related to which state has the lowest free energy [151]. To relate the Rayleigh-Plesset or Young-Laplace equations to MD, a simulation box of low apect ratio is favourable. Nonetheless, due to the thermal atomic fluctuations, the bubbles are never perfect spheres or cylinders. The bubble growth in Fig. 5.7 from MD shows a constant bubble size between the nucleation and collapse events. This could also be a consequence of the gemoetrical boundary conditions as well as the finite size of the domain.

One difficulty in evaluating the bubble radius, is that the cavity surface is highly irregular. The bubble does not remain as a sphere or a cylinder due to thermal atomic fluctuations. Therefore, the MD data provide only an estimate of the bubble radius. More sophisticated tools [152] can be used for a more precise characterization of the bubble.

The RP solution was obtained without accounting for the fluid viscosity, which inhibits the bubble dynamics. The RP predicted radius deviation from MD can be also attributed to the fact the RP exaggerates the inertia $\dot{R}^2$ term. This is rooted in the assumption of bubble growth in an infinite symmetric liquid field. The assumption of a constant temperature and vapour pressure of the bubble surface might not be valid on the molecular scale.

6.3. Multiscale framework

For a large range of pressure gradients and for a confinement down to 6 molecular diameters, the hydrodynamic equations are still valid. This is particularly evident from the parabolic fits to the MD velocity profiles, Fig. 4.3d. This implies the Navier-Stokes solution validity in nano-confined flows. For extremely confined fluids ($2-3$ atomic layers), the velocity and temperature profiles deviate from the hydrodynamic predictions, see Fig. 4.10a. The main reason for such deviation is the density oscillations owing to layering. At this level of confinement, there is a rapid variation in the strain rate, Fig. 4.7, that induces a high nonlocality in the transport properties. At high confinement, the Navier-Stokes equations are no longer applicable.

The ultimate goal of the current work is to solve lubrication problems by relying on the mass and momentum conservation equations rather than constitutive relations which may not hold for highly confined fluids. The algorithm should exploit the low computational cost of the continuum numerical algorithm in conjunction with the molecular precision. The continuum flow model is well-suited for regions of low confinement while in highly confined regions, we revert to the molecular resolution.

Therefore, the pump method presented here is in fact an approach to impose thermodynamic boundary conditions (e.g. $\dot{m}_x$ or j_x) passed on from the macro scale. The continuum-fluid solver provided by Holey et al. [17] is a suitable candidate as the macroscopic solution is agnostic of the constitutive lubricant bahaviour and is rather formulated in terms of the densities of conseved variables.

The solver computes the densities of conserved variables from the divergence of the flux functions as follows [17],

$$\frac{\partial}{\partial t}\begin{pmatrix}\rho \\ \vec{j}\end{pmatrix} = -\nabla \cdot \begin{pmatrix}\vec{j} \\ \frac{1}{\rho}(\vec{j}\otimes\vec{j}) + \underline{\sigma}\end{pmatrix} \tag{6.1}$$

where $\vec{j}$ is the mass flux vector and $\underline{\sigma}$ is the stress tensor (Eq. (A.5)). The first row denotes mass conservation while the second row denote the linear momentum conservation. The algorithm is described briefly in Algorithm 1.

Algorithm 1 Multiscale recursive scheme

```
Initial training data for the GPR model
while $r \leq \mathcal{N}$ do
    Get the macroscopic solution for $\underline{\sigma}$ at a selected $\vec{j}$
    while var($\underline{\sigma}$) $> \epsilon$ do
        Perform NEMD simulation at $j_x$ and acquire the corresponding $\underline{\sigma}$
        Use the NEMD $\underline{\sigma}$ to correct for $\vec{j}$ in the continuum scale
        Perform GPR analysis on the new $\underline{\sigma}$
    end while
    Advance the macroscopic solver $t + \Delta t$ and $r + \Delta r$
end while
```

with GPR: Gaussian process regression, $\mathcal{N}$: domain size, ϵ: uncertainty threshold, t: time, r: position.

For the initial GPR training data, NEMD simulations are performed in arbitrary locations in the domain and the corresponding $\underline{\sigma}$ is computed. At the macroscale, we obtain the solution for the stresses from Eq. (6.1) at a certain mass flux. The interpolation could be performed by Gaussian process regression (GPR) similar to Ref. [19]. The NEMD simulations are performed using the pump by setting j_x as the boundary condition.

A crucial aspect of this scheme is that modelling of atomistic effects such as slip, layering, cavitation, nonlocal viscosities and stresses is not be required in the macroscopic description. Only the coupling parameters, the mass flux and the stress tensor, need to be specified.

7. Conclusions and Outlook

7.1. Conclusions

In this study, non-equilibrium molecular dynamics simulations were employed to capture the details of a fluid lubricant flow in nanoconfined channels. The procedures followed and methods developed are transferable to various flow conditions and a wide range of materials. The presented method of introducing pressure gradients in periodic molecular domains, the “pump” method, could be a crucial tool to impose thermodynamic constraints passed on from the continuum scale. Thus, facilitating scale coupling and development of multiscale solutions to lubrication problems.

The method applies the fundamental conservation of linear momentum to generate pressure gradients in molecular representative volume elements. It is less computationally demanding relative to particle insertion-deletion algorithms and since the applied perturbation field is confined to a local region, the method allows investigating the fluid transport, physical and chemical changes purely from Newtonian dynamics.

To achieve a pressure-driven flow, the pump allows imposing either a constant force (the pressure gradient is the independent variable) or current (the mass flux is the independent variable). The former was dicussed in literature while the latter was not previously introduced in their context. The fixed current variant is agnostic of the interatomic potential and the channel geometry. Fast convergence as well as relevance to natural phenomena where the particle flux is measurable, grant the fixed current approach an advantage over the fixed force approach. With the pump, a range of 3 orders of magnitude of shear rate, from 10^8 to 10^{11} s^{-1} was possible. Fluid compressibility, wetting and layering near the boundaries do not affect the method’s functionality.

Atomistic simulations agree with the Navier-Stokes solutions down to a few molecular diameters. As the flow gets more confined, deviations from the hydrodynamic solution occur as molecular effects of layering dominate. Fluid layering leads to a disparity in the transport properties along the gap height. Thermostating the wall/fluid system should be imposed only on the walls with a stochastic algorithm to allow evaluating the correct fluid temperature and capture the unbiased fluid dynamics.

Applying the pump in converging-diverging channels permits the study of hydrodynamic cavitation. The voids or bubbles and their migration paths could be directly visualized from the atomic trajectories. A systematic investigation on the optimal channel geometry to control the cavitation nucleation site was conducted with the continuum-fluid solution. The gap height ratio D/d was found to be the most crucial parameter to aid the pressure drop at the diverging portion of the channel. The cavity's lifetime was monitored and evaluated through measuring the radius and interfacial velocity. The hydrodynamic Rayleigh-Plesset equation overestimates the radius compared to the atomistic calculations. Reducing the mass flux and increasing the temperature have adverse effects on the radius and the lifetime of the cavity.

7.2. Outlook

This work has focused on the physical properties of the fluid lubricant, without attention to the chemical properties including oxidation, solvency and other chemical changes to the lubricant. Deformation of the solid walls including corrosion and wear were also not considered. These factors are crucial to a complete modeling of the boundary lubrication regime.

The bubble dynamics in the collapse phase should be inspected in the free dynamics region. This will allow a more precise characterization of the bubbles for instance by measuring the energy released during collapse, a quantity that is not considered in the Rayleigh-Plesset equation. Many industrial processes rely on mixtures, such as emulsions, suspensions, and slurries, which are often subject to cavitation. Understanding the behavior of cavitation in these mixtures can help optimize industrial processes and prevent damage to equipment. Finally, realizing the MD-continuum recursive scheme could open prespectives for on-the-fly modelling of complex systems, such as natural (synovial fluid) and industrial lubricants (lubricant oils), from a continuum prespective while preserving their atomistic nature.

A. Reynolds transport theorem

By formulating a control volume analysis for any arbitrary region in the fluid flow, the flow conditions away from such volume becomes irrelevant. Reynolds transport theorem converts from system to control volume analysis [153, 154].

Consider a quantity B with its intensive value $\beta = dB/dm$, where m is mass. Reynolds transport theorem states that the rate of change of B within the system is equal to the rate of change of β within the control volume volume V in addition to the net flow of β from/to the control volume surfaces with area A. This can be written as

$$\frac{\mathrm{d}B}{\mathrm{d}t} = \frac{\mathrm{d}}{\mathrm{d}t}\left(\int_V \beta\rho\,\mathrm{d}V\right) + \int_{\text{out}} \beta\rho\vec{v}\,\mathrm{d}A - \int_{\text{in}} \beta\rho\vec{v}\,\mathrm{d}A \tag{A.1}$$

where in and out refer to the inlet and outlet of the control volume opposite surfaces. $\vec{v}$ is the velocity vector relative to an inertial coordinate system and ρ is the fluid density. The first term can be neglected for a fixed control volume, $\frac{\mathrm{d}V}{\mathrm{d}t}$ is zero. It can also be neglected when the flow is steady, i.e. neither β nor ρ change with time. If we consider the quantity in question to be the mass, i.e. $\beta = 1$, we get,

$$\frac{\mathrm{d}\,m}{\mathrm{d}t} = \int_{\text{out}} \rho\vec{v}\,\mathrm{d}A - \int_{\text{in}} \rho\vec{v}\,\mathrm{d}A \tag{A.2}$$

which is the mass conservation or continuity equation. For linear momentum balance, the quantities B and β become $m\vec{v}$ and $\vec{v}$, respectively. At steady state, Reynolds transport theorem reads,

$$\frac{\mathrm{d}(m\vec{v})}{\mathrm{d}t} = \sum \vec{F} = \int_{\text{out}} \rho\vec{v}^2\,\mathrm{d}A - \int_{\text{in}} \rho\vec{v}^2\,\mathrm{d}A \tag{A.3}$$

Reducing to one-dimensional analysis in the stream-wise x-direction,

$$\sum F_x = \int_{\text{out}} \rho u^2\,\mathrm{d}y\,\mathrm{d}z - \int_{\text{in}} \rho u^2\,\mathrm{d}y\,\mathrm{d}z \tag{A.4}$$

where u is the velocity component in the x-direction. This relation summarizes that the net force on any arbitrary region along the stream is equal to the net momentum flow.

Now, we focus on the left hand side of Eq. (A.4). The force F_x is the sum of body and surface forces. A body force acts in the form of a field such as gravity, electric or magnetic fields. In the current context, they are ignored. The surface forces arise from stresses on the sides of the control surface namely the hydrostatic pressure p and viscous stresses τ,

$$\underline{\sigma} = \begin{bmatrix} -p + \tau_{xx} & \tau_{xy} & \tau_{xz} \\ \tau_{yx} & -p + \tau_{yy} & \tau_{yz} \\ \tau_{zx} & \tau_{zy} & -p + \tau_{zz} \end{bmatrix} \tag{A.5}$$

The x-component of the total force, ignoring the body forces, acting on an arbitrary element is written as

$$\begin{aligned} \sum F_x &= \int \left[\frac{\partial \sigma_{xx}}{\partial x} + \frac{\partial \sigma_{xy}}{\partial y} + \frac{\partial \sigma_{xz}}{\partial z} \right] \mathrm{d}V \\ &= \int \left[-\frac{\partial p}{\partial x} + \frac{\partial \tau_{xx}}{\partial x} + \frac{\partial \tau_{xy}}{\partial y} + \frac{\partial \tau_{xz}}{\partial z} \right] \mathrm{d}V \end{aligned} \tag{A.6}$$

By equating Eq. (A.6) and Eq. (A.4), we get,

$$\int \left[-\frac{\partial p}{\partial x} + \frac{\partial \tau_{xx}}{\partial x} + \frac{\partial \tau_{xy}}{\partial y} + \frac{\partial \tau_{xz}}{\partial z} \right] \mathrm{d}V = \int_{\mathrm{out}} \rho u^2 \,\mathrm{d}y\,\mathrm{d}z - \int_{\mathrm{in}} \rho u^2 \,\mathrm{d}y\,\mathrm{d}z \tag{A.7}$$

If an external force F_{ext} is applied along the x-direction,

$$F_{\mathrm{ext}} = m a_{\mathrm{ext}} = \int \left[\frac{\partial p}{\partial x} - \frac{\partial \tau_{xx}}{\partial x} - \frac{\partial \tau_{xy}}{\partial y} - \frac{\partial \tau_{xz}}{\partial z} \right] \mathrm{d}V + \int_{\mathrm{out}} \rho u^2 \,\mathrm{d}y\,\mathrm{d}z - \int_{\mathrm{in}} \rho u^2 \,\mathrm{d}y\,\mathrm{d}z \tag{A.8}$$

where a_{ext} is the acceleration inside the control volume.

Eq. (A.8) describes the force balance in the control volume, refered to here as the “pump”. Hence, serving as the starting point for the pump method variants, where the external perturbation is in the form of a fixed force or a fixed current.

B. Discussion on thermostats

In this section, the aim is to answer three main questions: why is there a temperature gradient along the stream?, what is the optimal thermostating strategy for nanoconfined flows? and how does thermostating affect the dynamical processes and transport?

To proceed with the first question, the temperature gradient along the length in Fig. 4.8 suggests that the fluid flow deviates from an isothermal flow. Although the pressure profile is independent of the thermostat, (even for a highly compresible fluid as shown in Fig. B.1), the justification of the temperature gradient depends on the thermostat in consideration.

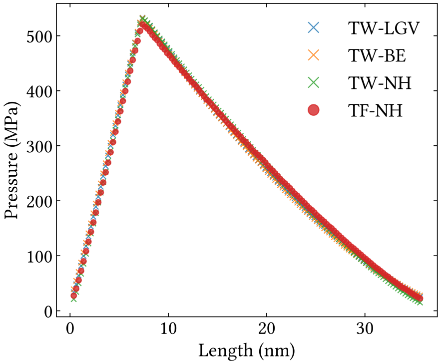

Figure B.1.: Virial pressure profile using different thermostats for the compressible fluid (Δp = 500 MPa) with the FF pump.

First, for the TF system (Fig. 4.8d), the gradient is due to the Nosé-Hoover thermostat's global control of the temperature. As ΔT in the pump is +60 K, the thermostat compensates by dropping the temperature in the pressure-driven region by −60 K. The thermostat does this to achieve an average temperature of 300 K, which is the time-averaged temperature of the whole fluid and is independent of the shear rate. Therefore, in this case the gradient is an artifact of the thermostat.

For the deterministic TW systems (Fig. 4.8b and Fig. 4.9c), the temperature gradient in the fluid is induced by the temperature gradient in the wall. Although the thermostats are applied only on the walls, they still act based on the global feedback of all atoms in the wall. The temperature in the solid rises in the pump region by 15 K and 25 K using the Berendsen and the Nosé-Hoover thermostats, respectively. It then drops by the same amount in the pressure-driven region. Similar to the TF system, the time-averaged temperature of the whole solid wall is kept at the desired temperature and is independent of the shear rate. Consequently, the gradient in the solid temperature is again due to the thermostat acting globally, however, the gradient in the fluid could be a result of the gradient in the solid.

For the TW-LGV system (Fig. 4.8a), the Langevin thermostat controls the temperature perfectly in the solid due to the stochastic forces acting locally. The temperature gradient in the fluid persists even with the absence of a gradient in the walls. This suggests that the temperature gradient is not an artifact of the thermostat and is rather a physical phenomenon.

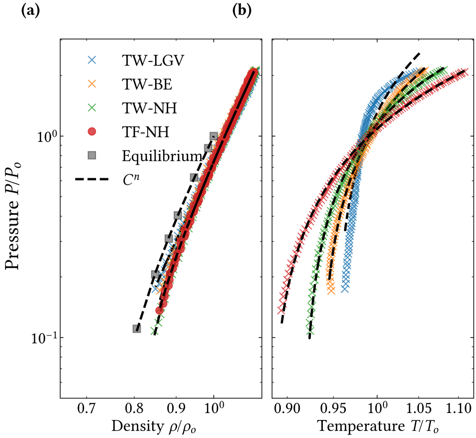

Figure B.2.: Variation of density and temperature in the pressure-driven region (outside the pump) for the compressible fluid $\Delta p = 500$ MPa with the FF pump.

To show how the flow develops into non-isothermal at high shear rate, the temperature and density are monitored in the pressure-driven region. As seen in Fig. B.2a, the density values from the NEMD simulations collapse into the same curve with the isothermal equation of state equilibrium simulations (at T=300 K) and can be fit to the polytropic equations of the form [155]

$$P\rho^{-k} = \text{constant} \quad \text{and} \quad PT^{(k/1-k)} = \text{constant} \tag{B.1}$$

where k is the polytropic index. For an isothermal flow, $k = 1$ and for an adiabatic reversible (isentropic) flow, k becomes the adiabatic exponent γ, which is the ratio of specific heats (c_p/c_v).

Although the polytropic equations assume that the fluid is an ideal gas, fitting the polytropic function to the $P - \rho$ and $P - T$ data is still reasonable. Since all thermostats give identical $P - \rho$ data (Fig. B.2a), the exponent k was computed as the fitting coefficient to be $\sim$ -8. Therefore, the isothermal and isentropic assumptions are not valid. The former is observed visually from the change of pressure with temperature while the latter is explained through heat removed/added by the thermostat from/to the fluid thus refuting the adiabatic assumption and the presence of friction which is an irreversible thermodynamic process.

To explain why the fluid flow becomes non-isothermal, the internal energy of the system increases as the fluid gets compressed, which in turn means a larger kinetic energy and temperature. This is similar to the throttling (or the Joule-Thomson) effect [156] but in a non-adiabatic condition, where the fluid cools during expansion and warms up during compression as long as the temperature is below the inversion temperature, the temperature above which an expanding fluid at constant enthalpy warms up.

To answer the second and third questions, the discussion focuses first on the TF system. Frozen or rigid walls pose a hurdle to study thermal transport since simply there is no heat dissipation from the fluid to the walls i.e. the fluid has infinite thermal conductivity. In an experimental setup, viscous heating of the fluid is transferred to the walls, which are in contact with the external environment. Another issue is that the rate of heat removal by the thermostat is larger than the rate of heat conduction across the fluid [144]. Moreover, the fact that the time-averged fluid temperature is independent of the shear rate is unrealistic [85]. In general, thermostating only the fluid does not generate the correct dynamics and consquently shows wrong temperature profiles [79, 84].

For the TF-NH thermostat, only the y-component of the equation of motion was coupled to the heat bath. Switching off the thermostat in the direction in which non-conservative forces are applied is usually done to recover the Galilean invariance [157]. However, such technique is not perfect since it assumes certain symmetry in the thermostating directions [158]. For the remaining part of the discussion, only the TW systems are considered.

From Fig. 4.8, it is evident that the Langevin thermostat is the most appropriate thermostat since it keeps the solid temperature uniform and constant at the desired temperature. However, the aim at this stage is to quantify how thermostats affect the dynamics of the fluid in the confined channel.

All the TW thermostats satisfy the local thermodynamic equilibrium (LTE) postulate. This is important since the kinetic temperature is equivalent to the thermodynamic temperature only if LTE is satisfied [79]. The probability distribution function of the fluid peculiar velocity components was measured in a 5Å × 5Å × 5Å central region in the confined fluid within slab walls box, Fig. 4.2. The distribution follows the normal Boltzmann distribution with close-to-zero skewness and kurtosis, see Fig. B.3. There is a slight deviation between the distribution functions of each velocity component, however, the statistics can be improved by sampling more regions in the fluid.

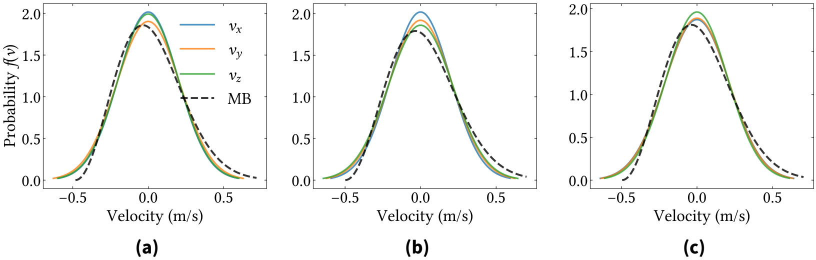

(a) **(b)** **(c)**

Figure B.3.: Thermal velocity distribution for the **a.** TW-LGV, **b.** TW-BE, **c.** TW-NH thermostats at Δp =500 MPa. The dashed lines represent the Maxwell-Boltzmann (MB) distribution fit to the data.

Finally, for a complete analysis, if the discussion is to be limited to the TW-LGV system, where shall the thermostat be applied in the walls? The configuration used so far is by applying it to the innermost wall atomic layers, however, another setup used frequently [87, 159] is to separate the thermostated wall region from the fluid with a few unthermostated solid layers sampling the microcanonical ensemble. This is usually done to minimize the thermostat effects at the solid/liquid interface. To test this notion, the simulation box in Fig. 4.2 was used. The outermost atoms are rigid, the middle are thermostated and the innermost are vibrating freely within the microcanoncial ensemble. A schematic of the direct-thermostating and buffered-thermostating setups are shown in Fig. B.4.

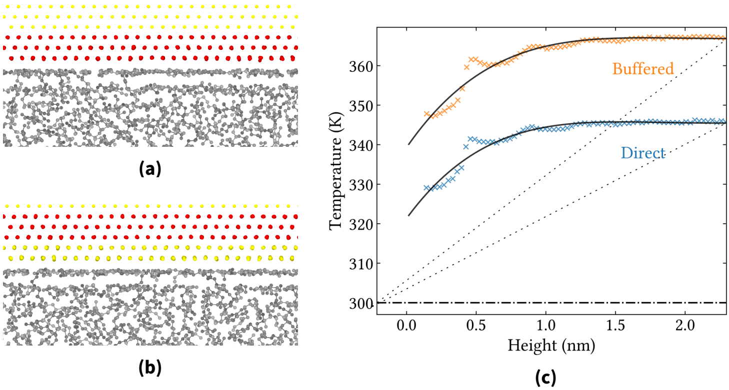

(a)

(b)

(c)

Figure B.4.: Langevin thermostat applied on wall atoms (TW-LGV) **a.** in contact with the fluid and **b.** at a buffer distance from the fluid. In the first case, the rest of the solid atoms are spatially fixed and in the second case, the innermost atoms between the thermostated region and the fluid is undergoing NVE dynamaics while the outermost atoms are spatially fixed. The pressure difference was set to $\Delta p = 500$ MPa in the FF pump. The temperature profiles are plotted in **c.** with the dotted lines showing the temperature jump ΔT_i from the walls to the fluid bulk and dash-dot line representing the target temperature at the walls.

Since the wall temperature is kept at 300 K, there is a temperature jump from the fluid to the wall, observed in Fig. B.4c. This is due to the thermal transport across the interface between different materials [89]. The temperature jump is related to the temperature gradient in the fluid through the Kapitza length L_K [88],

$$\Delta T_i = T_\mathrm{fluid} - T_\mathrm{wall} = L_\mathrm{K} \left. \frac{\partial T}{\partial n} \right|_\mathrm{fluid} \tag{B.2}$$

where $\frac{\partial T}{\partial n}$ is the temperature gradient in the fluid with n as the normal to the wall. The Kapitza length is similar in concept to the velocity slip length, it is the extrapolated length in the wall at which the fluid temperature matches that of the wall. To compute the Kapitza length, a temperature gradient has to be induced along the gap height. Simulations where a temperature gradient along the height (similar to Ref. [89, 160, 161]) have to be performed to measure the exact thermal resistance. However, the main concern here is whether the heat flow rate from the fluid to the walls is affected by the thermostat position.

The heat flow rate in the NEMD simulations was measured from the slope of the energy dissipated by the thermostat with time ($\dot{Q} = \Delta E/\Delta t$) [87, 162], while the continuum $\dot{Q}$ was evaluated from Eq. (2.13). From Fig. B.5, it is evident that thermostating the innermost or the middle solid layers does not change the thermal conduction significantly.

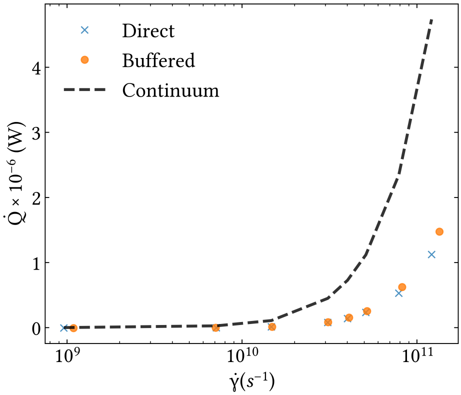

Figure B.5.: The heat flow rate $\dot{Q}$ for the direct and buffered thermostats compared to the continuum prediction.

The heat flow rate (and therefore heat flux) is slightly larger when the thermostat is applied at a distance from the fluid. Barisik and Beskok [89] argued that the temperature jump between the solid and fluid is a superposition of the interfacial and an artificial thermal resistance. The effect of this artificial thermal resistance can be minimized by positioning the thermostat on the solid layers away from the liquid. Additionally, they found that the heat flux from arrangements a. and b. in Fig. B.4 are very similar. This agrees with the finidings here.

In conclusion, as long as a stochastic thermostat with a proper damping parameter is applied only on the walls, its position does not affect the fluid transport significantly and would ideally control the wall temperature and capture the true fluid dynamics.

C. Application to lubricants & mixtures

To illustrate the transferability of the method to various chain lengths as well as lubricant-size molecules, a long branched (iso) alkane is considered here. Normal alkanes have no side chains while branched alkanes are derived from the corresponding straight-chain by removing one of the H atoms from the methylene bridge unit (CH_2) and replacing it with alkyl group. The branched alkane subject of this investigation is a higher alkane with $n = 30$, with the name 2,6,10,15,19,23-hexamethyltetracosane according to the IUPAC [1] naming convention, also known as squalane.

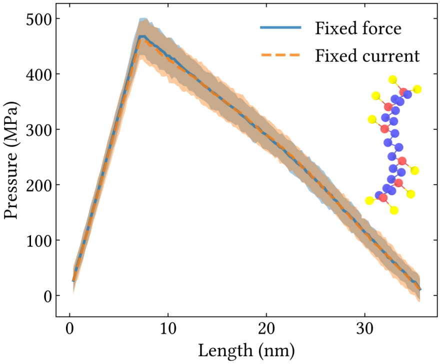

Figure C.1.: The pump method applied on squalane. The applied $\Delta p = 500$ MPa and $\dot{m} = 4.07 \times 10^{-19}$g/ns with the FF and FC variants, repectively. The applied $p_{\mathrm{ext}} = 250$ MPa. The shaded regions show the uncertainty in pressure.

---

[1] International Union of Pure and Applied Chemistry

The force field for squalane is described with GROMOS-54A7 with a united-atom representation. The long-range solver for computing the Coulombic interactions is the particle-particle particle-mesh (PPPM) method [149] with a relative error of 0.0001 in force evaluation. This value was shown to be sufficient for force evaluation in squalane and other long chain molecules [127]. To use PPPM in systems with slab geometry, the method proposed by Yeh et al. [163] was employed. The non-bonded Lennard-Jones and bonded interatomic parameters are listed in tables 3.1 and 3.2, respectively. Unlike interactions were evaluated using the geometric mean mixing rules. The LJ potential cutoff radius was 14 Å and the potential was shifted to zero at the cutoff.

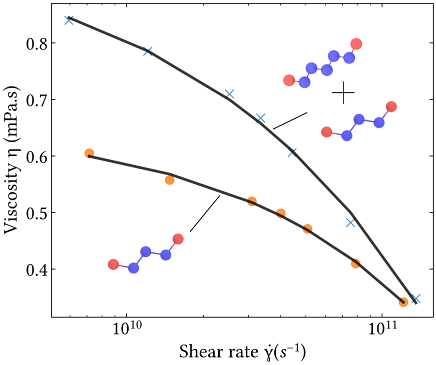

Figure C.2.: Flow curve of pure *n*-pentane and a mixture of *n*-pentane and *n*-heptane. The solid lines are power law fits $C\dot{\gamma}^{n-1}$.

The pump was also applied on a mixture of *n*-pentane and *n*-heptane. The composition of the mixture was 80% n-heptane and 20% n-pentane by volume. The shear rate $\dot{\gamma}$ reported here was obtained from the derivative of the parabolic profiles at $z = 0$, $\frac{\partial u}{\partial z}|_{z=0}$. The fluid viscosity at the interface was obtained from the constituitve relation $\sigma_{xz} = \eta\dot{\gamma}$. The flow curve shows that adding *n*-heptane acts as a viscosity modifier to the pure *n*-pentane fluid. Both fluids show shear thinning according to the power law Carreau model.

Bibliography

[1] A. I. Jewett, D. Stelter, J. Lambert, S. M. Saladi, O. M. Roscioni, M. Ricci, L. Autin, M. Maritan, S. M. Bashusqeh, T. Keyes, R. T. Dame, J.-E. Shea, G. J. Jensen, and D. S. Goodsell, "Moltemplate: A Tool for Coarse-Grained Modeling of Complex Biological Matter and Soft Condensed Matter Physics", Journal of Molecular Biology **433**, 166841 (2021).

[2] A. P. Thompson, H. M. Aktulga, R. Berger, D. S. Bolintineanu, W. M. Brown, P. S. Crozier, P. J. in 't Veld, A. Kohlmeyer, S. G. Moore, T. D. Nguyen, R. Shan, M. J. Stevens, J. Tranchida, C. Trott, and S. J. Plimpton, "LAMMPS - a flexible simulation tool for particle-based materials modeling at the atomic, meso, and continuum scales", Computer Physics Communications **271**, 108171 (2022).

[3] A. Stukowski, "Visualization and analysis of atomistic simulation data with OVITO-the Open Visualization Tool", Modelling and Simulation in Materials Science and Engineering **18**, 015012 (2010).

[4] T. S. Olsson and M. Hartley, "Lightweight data management with dtool", PeerJ **7**, e6562 (2019).

[5] A. Z. Szeri, *Fluid film lubrication*, 2nd ed. (Cambridge University Press, Cambridge, England, 2010).

[6] R. Dorf, *The engineering handbook*, 2nd ed. (CRC Press, Boca Raton, Florida, United States, 2005).

[7] R. Stribeck, "Die wesentlichen Eigenschaften der Gleit- und Rollenlager", Zeitschrift des Vereines Deutscher Ingenieure **46**, 1341–1348 (1902).

[8] O. Reynolds, "IV. On the theory of lubrication and its application to Mr. Beauchamp tower's experiments, including an experimental determination of the viscosity of olive oil", Philosophical Transactions of the Royal Society of London **177**, 157–234 (1886).

[9] A. Almqvist, E. Burtseva, F. Pérez-Ráfols, and P. Wall, “New insights on lubrication theory for compressible fluids”, International Journal of Engineering Science **145**, 103170 (2019).

[10] L. Bertocchi, D. Dini, M. Giacopini, M. T. Fowell, and A. Baldini, “Fluid film lubrication in the presence of cavitation: a mass-conserving two-dimensional formulation for compressible, piezoviscous and non-Newtonian fluids”, Tribology International **67**, 61–71 (2013).

[11] K. P. Travis, B. D. Todd, and D. J. Evans, “Departure from Navier-Stokes hydrodynamics in confined liquids”, Physical Review E **55**, 4288–4295 (1997).

[12] K. P. Travis and K. E. Gubbins, “Poiseuille flow of Lennard-Jones fluids in narrow slit pores”, The Journal of Chemical Physics **112**, 1984–1994 (2000).

[13] P. A. Thompson and M. O. Robbins, “Shear flow near solids: Epitaxial order and flow boundary conditions”, Physical Review A **41**, 6830–6837 (1990).

[14] W. E. Alley and B. J. Alder, “Generalized transport coefficients for hard spheres”, Physical Review A **27**, 3158–3173 (1983).

[15] B. D. Todd, J. S. Hansen, and P. J. Daivis, “Nonlocal Shear Stress for Homogeneous Fluids”, Physical Review Letters **100**, 195901 (2008).

[16] A. Codrignani, D. Savio, F. Magagnato, and B. Frohnapfel, “A scaling parameter for pressure losses and thermal effects in lubricant flows with viscous dissipation”, Tribology International, 43rd Leeds - Lyon Symposium on Tribology 2016 **113**, 238–244 (2017).

[17] H. Holey, A. Codrignani, P. Gumbsch, and L. Pastewka, “Height-Averaged Navier–Stokes Solver for Hydrodynamic Lubrication”, Tribology Letters **70**, 36 (2022).

[18] J. P. Ewen, D. M. Heyes, and D. Dini, “Advances in nonequilibrium molecular dynamics simulations of lubricants and additives”, Friction **6**, 349–386 (2018).

[19] D. Stephenson, J. R. Kermode, and D. A. Lockerby, “Accelerating multiscale modelling of fluids with on-the-fly Gaussian process regression”, Microfluid. Nanofluidics **22**, 139 (2018).

[20] J. Boon and S. Yip, *Molecular Hydrodynamics* (Dover Publications, 1991).

[21] E. N. Harvey, W. D. McElroy, and A. H. Whiteley, “On Cavity Formation in Water”, Journal of Applied Physics **18**, 162–172 (1947).

[22] J. K. Vennard, “Cavitation in hydraulic structures: a symposium”, Transactions of the American Society of Civil Engineers **112**, 1–15 (1947).

[23] R. E. A. Arndt, “Cavitation in Fluid Machinery and Hydraulic Structures”, Annual Review of Fluid Mechanics **13**, 273–326 (1981).

[24] P.-C. Chu, W.-Y. Chai, C.-H. Tsai, S.-T. Kang, C.-K. Yeh, and H.-L. Liu, “Focused Ultrasound-Induced Blood-Brain Barrier Opening: Association with Mechanical Index and Cavitation Index Analyzed by Dynamic Contrast-Enhanced Magnetic-Resonance Imaging”, Scientific Reports **6**, 33264 (2016).

[25] H.-L. Liu, C.-H. Fan, C.-Y. Ting, and C.-K. Yeh, “Combining Microbubbles and Ultrasound for Drug Delivery to Brain Tumors: Current Progress and Overview”, Theranostics **4**, 432–444 (2014).

[26] Y. A. Pishchalnikov, O. A. Sapozhnikov, M. R. Bailey, J. C. Williams, R. O. Cleveland, T. Colonius, L. A. Crum, A. P. Evan, and J. A. McAteer, “Cavitation Bubble Cluster Activity in the Breakage of Kidney Stones by Lithotripter Shockwaves”, Journal of Endourology **17**, 435–446 (2003).

[27] P. Marmottant and S. Hilgenfeldt, “A bubble-driven microfluidic transport element for bioengineering”, Proceedings of the National Academy of Sciences **101**, 9523–9527 (2004).

[28] T. Sebastian and C. Strem, *Toroidal propeller*, U.S. Patent 10 836 466, Nov. 2020.

[29] F. Lugli and F. Zerbetto, “An introduction to bubble dynamics”, Physical Chemistry Chemical Physics **9**, 2447 (2007).

[30] R. T. Knapp and A. Hollander, “Laboratory Investigations of the Mechanism of Cavitation”, Transactions of the American Society of Mechanical Engineers **70**, 419–431 (1948).

[31] A. J. Acosta and B. R. Parkin, “Cavitation Inception—A Selective Review”, Journal of Ship Research **19**, 193–205 (1975).

[32] N. G. Hadjiconstantinou, “Discussion of recent developments in hybrid atomistic-continuum methods for multiscale hydrodynamics”, Bulletin of the Polish Academy of Sciences Technical Sciences **53**, 335–342 (2005).

[33] J. Koplik, J. Banavar, and J. Willemsen, “Molecular dynamics of Poiseuille flow and moving contact lines”, Physical Review Letters **60**, 1282 (1988).

[34] W. T. Ashurst and W. G. Hoover, “Dense-fluid shear viscosity via nonequilibrium molecular dynamics”, Physical Review A **11**, 658–678 (1975).

[35] B. D. Todd and P. J. Daivis, *Nonequilibrium molecular dynamics: theory, algorithms and applications* (Cambridge University Press, Cambridge, England, 2017).

[36] E. M. Gosling, I. McDonald, and K. Singer, “On the calculation by molecular dynamics of the shear viscosity of a simple fluid”, Molecular Physics **26**, 1475–1484 (1973).

[37] B. D. Todd and D. J. Evans, “Temperature profile for Poiseuille flow”, Physical Review E **55**, 2800–2807 (1997).

[38] A. W. Lees and S. F. Edwards, “The computer study of transport processes under extreme conditions”, Journal of Physics C: Solid State Physics **5**, 1921–1928 (1972).

[39] D. J. Evans and G. P. Morriss, “Nonlinear-response theory for steady planar Couette flow”, Physical Review A **30**, 1528–1530 (1984).

[40] W. G. Hoover, “Canonical dynamics: Equilibrium phase-space distributions”, Physical Review A **31**, 1695–1697 (1985).

[41] O. Guvench and A. D. MacKerell, “Comparison of Protein Force Fields for Molecular Dynamics Simulations”, in *Molecular Modeling of Proteins*, edited by A. Kukol, Methods Molecular Biology™ (Humana Press, Totowa, NJ, 2008), pp. 63–88.

[42] M. P. Allen and D. J. Tildesley, *Computer simulation of liquids* (Press, Oxford Clarendon, 2017).

[43] N. Schmid, A. P. Eichenberger, A. Choutko, S. Riniker, M. Winger, A. E. Mark, and W. F. van Gunsteren, “Definition and testing of the GROMOS force-field versions 54A7 and 54B7”, European Biophysics Journal **40**, 843–856 (2011).

[44] M. G. Martin and J. I. Siepmann, “Transferable Potentials for Phase Equilibria. 1. United-Atom Description of n-Alkanes”, The Journal of Physical Chemistry B **102**, 2569–2577 (1998).

[45] W. L. Jorgensen, J. D. Madura, and C. J. Swenson, “Optimized intermolecular potential functions for liquid hydrocarbons”, Journal of the American Chemical Society **106**, 6638–6646 (1984).

[46] M. Moseler and U. Landman, “Formation, Stability, and Breakup of Nanojets”, Science **289**, 1165–1169 (2000).

[47] D. M. Holland, D. A. Lockerby, M. K. Borg, W. D. Nicholls, and J. M. Reese, “Molecular dynamics pre-simulations for nanoscale computational fluid dynamics”, Microfluidics and Nanofluidics **18**, 461–474 (2015).

[48] C. Huang, K. Nandakumar, P. Y. K. Choi, and L. W. Kostiuk, “Molecular dynamics simulation of a pressure-driven liquid transport process in a cylindrical nanopore using two self-adjusting plates”, The Journal of Chemical Physics **124**, 234701 (2006).

[49] S. Y. Docherty, W. D. Nicholls, M. K. Borg, D. A. Lockerby, and J. M. Reese, “Boundary conditions for molecular dynamics simulations of water transport through nanotubes”, Proceedings of the Institution of Mechanical Engineers, Part C: Journal of Mechanical Engineering Science **228**, 186–195 (2014).

[50] S. E. Strong and J. D. Eaves, “The Dynamics of Water in Porous Two-Dimensional Crystals”, The Journal of Physical Chemistry B **121**, 189–207 (2017).

[51] L. Hannon, G. C. Lie, and E. Clementi, “Molecular dynamics simulation simulation of channel flow”, Physics Letters A **119**, 174–177 (1986).

[52] D. K. Bhattacharya and G. C. Lie, “Molecular-Dynamics Simulations of Nonequilibrium Heat and Momentum Transport in Very Dilute Gases”, Physical Review Letters **62**, 897–900 (1989).

[53] I. Hanasaki and A. Nakatani, “Fluidized piston model for molecular dynamics simulations of hydrodynamic flow”, Modelling and Simulation in Materials Science and Engineering **14**, S9–S20 (2006).

[54] M. Sun and C. Ebner, “Molecular-dynamics simulation of compressible fluid flow in two-dimensional channels”, Physical Review A **46**, 4813–4818 (1992).

[55] G. S. Heffelfinger and F. van Swol, “Diffusion in Lennard-Jones fluids using dual control volume grand canonical molecular dynamics simulation (DCV-GCMD)”, The Journal of Chemical Physics **100**, 7548–7552 (1994).

[56] J. Li, D. Liao, and S. Yip, “Coupling continuum to molecular-dynamics simulation: Reflecting particle method and the field estimator”, Physical Review E **57**, 7259–7267 (1998).

[57] R. Delgado-Buscalioni and P. V. Coveney, “USHER : An algorithm for particle insertion in dense fluids”, The Journal of Chemical Physics **119**, 978–987 (2003).

[58] J. A. Thomas and A. J. H. McGaughey, “Reassessing Fast Water Transport Through Carbon Nanotubes”, Nano Letters **8**, 2788–2793 (2008).

[59] F. Zhu, E. Tajkhorshid, and K. Schulten, “Pressure-Induced Water Transport in Membrane Channels Studied by Molecular Dynamics”, Biophysical Journal **83**, 154–160 (2002).

[60] J. Goldsmith and C. C. Martens, “Pressure-induced water flow through model nanopores”, Physical Chemistry Chemical Physics **11**, 528–533 (2009).

[61] H. Frentrup, C. Avendaño, M. Horsch, A. Salih, and E. A. Müller, “Transport diffusivities of fluids in nanopores by non-equilibrium molecular dynamics simulation”, Molecular Simulation **38**, 540–553 (2012).

[62] Z. Liang and H.-L. Tsai, “A method to generate pressure gradients for molecular simulation of pressure-driven flows in nanochannels”, Microfluidics and Nanofluidics **13**, 289–298 (2012).

[63] S. E. Strong and J. D. Eaves, “The Dynamics of Water in Porous Two-Dimensional Crystals”, The Journal of Physical Chemistry B **121**, 189–207 (2017).

[64] D. H. Tsai, “The virial theorem and stress calculation in molecular dynamics”, The Journal of Chemical Physics **70**, 1375–1382 (1979).

[65] J. H. Irving and J. G. Kirkwood, “The Statistical Mechanical Theory of Transport Processes. IV. The Equations of Hydrodynamics”, The Journal of Chemical Physics **18**, 817–829 (1950).

[66] K. S. Cheung and S. Yip, “Atomic-level stress in an inhomogeneous system”, Journal of Applied Physics **70**, 5688–5690 (1991).

[67] A. Ghoufi, P. Malfreyt, and D. J. Tildesley, “Computer modelling of the surface tension of the gas–liquid and liquid–liquid interface”, Chemical Society Reviews **45**, 1387–1409 (2016).

[68] G. J. Gloor, G. Jackson, F. J. Blas, and E. de Miguel, “Test-area simulation method for the direct determination of the interfacial tension of systems with continuous or discontinuous potentials”, The Journal of Chemical Physics **123**, 134703 (2005).

[69] D. J. Evans and G. Morriss, *Statistical mechanics of nonequilibrium liquids*, 2nd ed. (Cambridge University Press, Cambridge, England, 2008).

[70] K.-S. Kim, M. H. Han, C. Kim, Z. Li, G. E. Karniadakis, and E. K. Lee, “Nature of intrinsic uncertainties in equilibrium molecular dynamics estimation of shear viscosity for simple and complex fluids”, The Journal of Chemical Physics **149**, 044510 (2018).

[71] T. Chen, B. Smit, and A. T. Bell, “Are pressure fluctuation-based equilibrium methods really worse than nonequilibrium methods for calculating viscosities?”, The Journal of Chemical Physics **131**, 246101 (2009).

[72] P. G. de Gennes, “On fluid/wall slippage”, Langmuir **18**, 3413–3414 (2002).

[73] R. Pit, H. Hervet, and L. Léger, “Direct Experimental Evidence of Slip in Hexadecane: Solid Interfaces”, Physical Review Letters **85**, 980–983 (2000).

[74] N. V. Priezjev, “Rate-dependent slip boundary conditions for simple fluids”, Physical Review E **75**, 051605 (2007).

[75] J.-P. Hansen and I. R. McDonald, *Theory of simple liquids*, 4th ed. (Academic Press, 2013).

[76] P. H. Hünenberger, “Thermostat Algorithms for Molecular Dynamics Simulations”, in *Advanced Computer Simulation*, Vol. 173, edited by A. Abe, J.-F. Joanny, A.-C. Albertsson, R. Duncan, H.-H. Kausch, S. Kobayashi, K. Dušek, K.-S. Lee, W. de Jeu, L. Leibler, O. Nuyken, T. E. Long, E. Terentjev, B. Voit, I. Manners, G. Wegner, M. Möller, C. Dr. Holm, and K. Prof. Dr. Kremer (Springer Berlin Heidelberg, Berlin, Heidelberg, Jan. 2005), pp. 105–149.

[77] H. Goldstein, C. P. Poole Jr, and J. L. Safko, *Classical mechanics*, 3rd ed. (Addison Wesley, 2001).

[78] J. E. Basconi and M. R. Shirts, “Effects of Temperature Control Algorithms on Transport Properties and Kinetics in Molecular Dynamics Simulations”, Journal of Chemical Theory and Computation **9**, 2887–2899 (2013).

[79] X. Yong and L. T. Zhang, “Thermostats and thermostat strategies for molecular dynamics simulations of nanofluidics”, The Journal of Chemical Physics **138**, 084503 (2013).

[80] T. Schneider and E. Stoll, “Molecular-dynamics study of a three-dimensional one-component model for distortive phase transitions”, Physical Review B **17**, 1302–1322 (1978).

[81] H. J. C. Berendsen, J. P. M. Postma, W. F. van Gunsteren, A. DiNola, and J. R. Haak, “Molecular dynamics with coupling to an external bath”, The Journal of Chemical Physics **81**, 3684–3690 (1984).

[82] S. Nosé, “A unified formulation of the constant temperature molecular dynamics methods”, The Journal of Chemical Physics **81**, 511–519 (1984).

[83] D. J. Evans and G. P. Morriss, “Shear Thickening and Turbulence in Simple Fluids”, Physical Review Letters **56**, 2172–2175 (1986).

[84] S. Bernardi, B. D. Todd, and D. J. Searles, “Thermostating highly confined fluids”, The Journal of Chemical Physics **132**, 244706 (2010).

[85] D. Toton, C. D. Lorenz, N. Rompotis, N. Martsinovich, and L. Kantorovich, “Temperature control in molecular dynamic simulations of non-equilibrium processes”, Journal of Physics: Condensed Matter **22**, 074205 (2010).

[86] J. P. Ewen, C. Gattinoni, N. Morgan, H. A. Spikes, and D. Dini, “Nonequilibrium Molecular Dynamics Simulations of Organic Friction Modifiers Adsorbed on Iron Oxide Surfaces”, Langmuir **32**, 4450–4463 (2016).

[87] J. Ghorbanian and A. Beskok, “Temperature profiles and heat fluxes observed in molecular dynamics simulations of force-driven liquid flows”, Physical Chemistry Chemical Physics **19**, 10317–10325 (2017).

[88] B. H. Kim, A. Beskok, and T. Cagin, “Molecular dynamics simulations of thermal resistance at the liquid-solid interface”, The Journal of Chemical Physics **129**, 174701 (2008).

[89] M. Barisik and A. Beskok, “Boundary treatment effects on molecular dynamics simulations of interface thermal resistance”, Journal of Computational Physics **231**, 7881–7892 (2012).

[90] C. E. Brennen, *Cavitation and bubble dynamics* (Cambridge University Press, Cambridge, England, 2013).

[91] M. S. Plesset and A. Prosperetti, “Bubble Dynamics and Cavitation”, Annual Review of Fluid Mechanics **9**, 145–185 (1977).

[92] J.-P. Franc, “The Rayleigh-Plesset equation: a simple and powerful tool to understand various aspects of cavitation”, in *Fluid Dynamics of Cavitation and Cavitating Turbopumps*, edited by L. d’Agostino and M. V. Salvetti, CISM International Centre for Mechanical Sciences (Springer, Vienna, 2007), pp. 1–41.

[93] M. Blander and J. L. Katz, “Bubble nucleation in liquids”, AIChE Journal **21**, 833–848 (1975).

[94] V. G. Baidakov, A. O. Tipeev, K. S. Bobrov, and G. V. Ionov, “Crystal nucleation rate isotherms in Lennard-Jones liquids”, The Journal of Chemical Physics **132**, 234505 (2010).

[95] V. G. Baidakov and K. S. Bobrov, “Spontaneous cavitation in a Lennard-Jones liquid at negative pressures”, The Journal of Chemical Physics **140**, 184506 (2014).

[96] T. Kinjo and M. Matsumoto, “Cavitation processes and negative pressure”, Fluid Phase Equilibria **144**, 343–350 (1998).

[97] M. Ghorbani, A. K. Sadaghiani, L. G. Villanueva, and A. Koşar, “Hydrodynamic cavitation in microfluidic devices with roughened surfaces”, Journal of Micromechanics and Microengineering **28**, 075016 (2018).

[98] C. Mishra and Y. Peles, “An experimental investigation of hydrodynamic cavitation in micro-Venturis”, Physics of Fluids **18**, 103603 (2006).

[99] M. Medrano, P. J. Zermatten, C. Pellone, J. P. Franc, and F. Ayela, “Hydrodynamic cavitation in microsystems. I. Experiments with deionized water and nanofluids”, Physics of Fluids **23**, 127103 (2011).

[100] L. Rayleigh, “VIII. *On the pressure developed in a liquid during the collapse of a spherical cavity*”, The London, Edinburgh, and Dublin Philosophical Magazine and Journal of Science **34**, 94–98 (1917).

[101] M. S. Plesset, “The Dynamics of Cavitation Bubbles”, Journal of Applied Mechanics **16**, 277–282 (1949).

[102] F. R. Gilmore, *The growth or collapse of a spherical bubble in a viscous compressible liquid*, Report 26-4, California Institute of Technology, Pasadena, CA, Apr. 1952.

[103] J. Dzubiella, “Interface dynamics of microscopic cavities in water”, The Journal of Chemical Physics **126**, 194504 (2007).

[104] B. J. Block, S. K. Das, M. Oettel, P. Virnau, and K. Binder, “Curvature dependence of surface free energy of liquid drops and bubbles: A simulation study”, The Journal of Chemical Physics **133**, 154702 (2010).

[105] H. Liu and G. Cao, “Effectiveness of the Young-Laplace equation at nanoscale”, Scientific Reports **6**, 23936 (2016).

[106] P. Montero de Hijes, K. Shi, E. G. Noya, E. E. Santiso, K. E. Gubbins, E. Sanz, and C. Vega, “The Young–Laplace equation for a solid–liquid interface”, The Journal of Chemical Physics **153**, 191102 (2020).

[107] D. Vijayaraghavan and T. G. Keith, “Development and Evaluation of a Cavitation Algorithm”, Tribology Transactions **32**, 225–233 (1989).

[108] B. Jakobsson and L. Floberg, “The finite journal bearing, considering vaporization: (das Gleitlager von endlicher Breite mit Verdampfung).”, Transactions of Chalmers University of Technology (1957).

[109] K. Olsson, *Cavitation in dynamically loaded bearings* (Scandinavian University Books, 1965).

[110] H. G. Elrod, “A Cavitation Algorithm”, Journal of Lubrication Technology **103**, 350–354 (1981).

[111] M. Paggi and D. Hills, *Modeling and simulation of tribological problems in technology* (Springer, 2020).

[112] H. Elrod, “A computer program for cavitation and starvation problems”, Proceedings of the 1st Leeds-Lyon Symposium on Tribology **37** (1974).

[113] F. Sahlin, A. Almqvist, R. Larsson, and S. Glavatskih, “A cavitation algorithm for arbitrary lubricant compressibility”, Tribology International **40**, 1294–1300 (2007).

[114] D. Dowson and G. R. Higginson, *Elasto-hydrodynamic lubrication: international series on materials science and technology* (Elsevier, 2014).

[115] G. Bayada and L. Chupin, “Compressible Fluid Model for Hydrodynamic Lubrication Cavitation”, Journal of Tribology **135**, 041702 (2013).

[116] R. Hołyst, M. Litniewski, and P. Garstecki, “Large-scale molecular dynamics verification of the Rayleigh-Plesset approximation for collapse of nanobubbles”, Physical Review E **82**, 066309 (2010).

[117] F. Lugli, S. Höfinger, and F. Zerbetto, “The Collapse of Nanobubbles in Water”, Journal of the American Chemical Society **127**, 8020–8021 (2005).

[118] H. Okumura and N. Ito, “Nonequilibrium molecular dynamics simulations of a bubble”, Physical Review E, 4 (2003).

[119] V. H. Man, M. S. Li, P. Derreumaux, and P. H. Nguyen, “Rayleigh-Plesset equation of the bubble stable cavitation in water: A nonequilibrium all-atom molecular dynamics simulation study”, The Journal of Chemical Physics **148**, 094505 (2018).

[120] A. Stukowski, “Computational Analysis Methods in Atomistic Modeling of Crystals”, JOM **66**, 399–407 (2014).

[121] C. W. Scholz, Y. Sanchez-Vicente, T. Tananilgul, M. Thol, J. P. M. Trusler, and M. Richter, “Speeds of Sound in n-Pentane at Temperatures from 233.50 to 473.15 K at Pressures up to 390 MPa”, Journal of Chemical & Engineering Data, 11 (2020).

[122] H. Heinz, R. A. Vaia, B. L. Farmer, and R. R. Naik, “Accurate Simulation of Surfaces and Interfaces of Face-Centered Cubic Metals Using 12-6 and 9-6 Lennard-Jones Potentials”, The Journal of Physical Chemistry C **112**, 17281–17290 (2008).

[123] M. Gehrig and H. Lentz, “Values of p(V,T) for n-pentane in the range 5 to 250 MPa and 313 to 643 K”, The Journal of Chemical Thermodynamics **11**, 291–300 (1979).

[124] K. Liu, Y. Wu, M. A. McHugh, H. Baled, R. M. Enick, and B. D. Morreale, “Equation of state modeling of high-pressure, high-temperature hydrocarbon density data”, The Journal of Supercritical Fluids, 100th Year Anniversary of van Der Waals’ Nobel Lecture **55**, 701–711 (2010).

[125] E. J. Maginn, R. A. Messerly, D. J. Carlson, D. R. Roe, and J. R. Elliot, “Best Practices for Computing Transport Properties 1. Self-Diffusivity and Viscosity from Equilibrium Molecular Dynamics”, Living Journal of Computational Molecular Science **2** (2020).

[126] F. Audonnet and A. A. H. Pádua, “Simultaneous measurement of density and viscosity of n-pentane from 298 to 383 K and up to 100 MPa using a vibrating-wire instrument”, Fluid Phase Equilibria **181**, 147–161 (2001).

[127] J. Ewen, C. Gattinoni, F. Thakkar, N. Morgan, H. Spikes, and D. Dini, “A Comparison of Classical Force-Fields for Molecular Dynamics Simulations of Lubricants”, Materials **9**, 651 (2016).

[128] M. Thol, T. Uhde, E. Lemmon, and R. Span, “Fundamental equations of state for hydrocarbons”, Part I. n-Pentane, Unpublished (2018).

[129] A. Mulero, I. Cachadiña, and M. I. Parra, “Recommended Correlations for the Surface Tension of Common Fluids”, Journal of Physical and Chemical Reference Data **41**, 043105 (2012).

[130] V. G. Baidakov, S. P. Protsenko, Z. R. Kozlova, and G. G. Chernykh, “Metastable extension of the liquid-vapor phase equilibrium curve and surface tension”, The Journal of Chemical Physics **126**, 214505 (2007).

[131] T. Werder, J. H. Walther, R. L. Jaffe, T. Halicioglu, and P. Koumoutsakos, “On the Water-Carbon Interaction for Use in Molecular Dynamics Simulations of Graphite and Carbon Nanotubes”, The Journal of Physical Chemistry B **107**, 1345–1352 (2003).

[132] J. T. Hirvi and T. A. Pakkanen, “Molecular dynamics simulations of water droplets on polymer surfaces”, The Journal of Chemical Physics **125**, 144712 (2006).

[133] J. A. Beattie, S. W. Levine, and D. R. Douslin, “The Vapor Pressure and Critical Constants of Normal Pentane”, Journal of the American Chemical Society, 4431–4432 (1951).

[134] A. E. van Giessen and E. M. Blokhuis, “Direct determination of the Tolman length from the bulk pressures of liquid drops via molecular dynamics simulations”, The Journal of Chemical Physics **131**, 164705 (2009).

[135] M. J. Haye and C. Bruin, “Molecular dynamics study of the curvature correction to the surface tension”, The Journal of Chemical Physics **100**, 556–559 (1994).

[136] L. Pastewka, S. Moser, and M. Moseler, “Atomistic insights into the running-in, lubrication, and failure of hydrogenated diamond-like carbon coatings”, Tribology Letters **39**, 49–61 (2010).

[137] C. Sendner, D. Horinek, L. Bocquet, and R. R. Netz, “Interfacial Water at Hydrophobic and Hydrophilic Surfaces: Slip, Viscosity, and Diffusion”, Langmuir **25**, 10768–10781 (2009).

[138] N. V. Priezjev, “Effect of surface roughness on rate-dependent slip in simple fluids”, The Journal of Chemical Physics **127**, 144708 (2007).

[139] A. Martini, H.-Y. Hsu, N. A. Patankar, and S. Lichter, “Slip at High Shear Rates”, Physical Review Letters **100**, 206001 (2008).

[140] R. W. MacCormack, “The Effect of Viscosity in Hypervelocity Impact Cratering”, Journal of Spacecraft and Rockets **40**, 757–763 (2003).

[141] M. B. Ewing, A. R. H. Goodwin, and J. P. M. Trusler, “Thermophysical properties of alkanes from speeds of sound determined using a spherical resonator 3. n-Pentane”, The Journal of Chemical Thermodynamics **21**, 867–877 (1989).

[142] M. Li, A. Bussonnière, M. Bronson, Z. Xu, and Q. Liu, “Study of Venturi tube geometry on the hydrodynamic cavitation for the generation of microbubbles”, Minerals Engineering **132**, 268–274 (2019).

[143] K. R. Weninger, B. P. Barber, and S. J. Putterman, “Pulsed Mie Scattering Measurements of the Collapse of a Sonoluminescing Bubble”, Physical Review Letters **78**, 1799–1802 (1997).

[144] R. Khare, J. de Pablo, and A. Yethiraj, “Molecular simulation and continuum mechanics study of simple fluids in non-isothermal planar couette flows”, The Journal of Chemical Physics **107**, 2589–2596 (1997).

[145] M. H. Müser, S. V. Sukhomlinov, and L. Pastewka, “Interatomic potentials: achievements and challenges”, Advances in Physics: X **8**, 2093129 (2023).

[146] M. S. Daw and M. I. Baskes, “Embedded-atom method: derivation and application to impurities, surfaces, and other defects in metals”, Physical Review B **29**, 6443–6453 (1984).

[147] M. I. D. B. Bouchet, C. Matta, T. Le-Mogne, J. M. Martin, T. Sagawa, S. Okuda, and M. Kano, “Improved mixed and boundary lubrication with glycerol-diamond technology”, Tribology - Materials, Surfaces & Interfaces **1**, 28–32 (2007).

[148] J.-L. Barrat and L. Bocquet, “Large Slip Effect at a Nonwetting Fluid-Solid Interface”, Physical Review Letters **82**, 4671–4674 (1999).

[149] R. W. Hockney and J. W. Eastwood, *Computer simulation using particles* (CRC Press, Florida, United States, 2021).

[150] S. M. Hsu, “Molecular basis of lubrication”, Tribology International, The New Trends and Frontiers in Tribology **37**, 553–559 (2004).

[151] L. G. MacDowell, V. K. Shen, and J. R. Errington, “Nucleation and cavitation of spherical, cylindrical, and slablike droplets and bubbles in small systems”, The Journal of Chemical Physics **125**, 034705 (2006).

[152] P. Schmidtke, A. Bidon-Chanal, F. J. Luque, and X. Barril, “MDpocket: open-source cavity detection and characterization on molecular dynamics trajectories”, Bioinformatics **27**, 3276–3285 (2011).

[153] O. Reynolds, *The sub-mechanics of the universe* (Cambridge University Press, Cambridge, 1903).

[154] F. M. White, *Fluid mechanics*, 8th ed. (McGraw Hill Education, 2016).

[155] F. Holland and R. Bragg, *Fluid flow for chemical and process engineers*, 2nd ed. (Butterworth-Heinemann, 1995).

[156] F. Reif, *Fundamentals of statistical and thermal physics* (McGraw-Hill, New York, 1965).

[157] C. Pastorino, T. Kreer, M. Müller, and K. Binder, “Comparison of dissipative particle dynamics and Langevin thermostats for out-of-equilibrium simulations of polymeric systems”, Physical Review E **76**, 026706 (2007).

[158] T. Soddemann, B. Dünweg, and K. Kremer, “Dissipative particle dynamics: A useful thermostat for equilibrium and nonequilibrium molecular dynamics simulations”, Physical Review E **68**, 046702 (2003).

[159] J. P. Ewen, H. Gao, M. H. Müser, and D. Dini, “Shear heating, flow, and friction of confined molecular fluids at high pressure”, Physical Chemistry Chemical Physics **21**, 5813–5823 (2019).

[160] P. Wirnsberger, D. Frenkel, and C. Dellago, “An enhanced version of the heat exchange algorithm with excellent energy conservation properties”, The Journal of Chemical Physics **143**, 124104 (2015).

[161] F. Müller-Plathe, “A simple nonequilibrium molecular dynamics method for calculating the thermal conductivity”, The Journal of Chemical Physics **106**, 6082–6085 (1997).

[162] T. Ikeshoji and B. Hafskjold, “Non-equilibrium molecular dynamics calculation of heat conduction in liquid and through liquid-gas interface”, Molecular Physics **81**, 251–261 (1994).

[163] I.-C. Yeh and M. L. Berkowitz, “Ewald summation for systems with slab geometry”, The Journal of Chemical Physics **111**, 3155–3162 (1999).